The Thesis Committee for Yu Liang
Certifies that this is the approved version of the following thesis:

Experimental Study of Convective Dissolution of Carbon Dioxide in Porous Media

APPROVED BY
SUPERVISING COMMITTEE:

Supervisor:

David A. DiCarlo

Marc A. Hesse

Experimental Study of Convective Dissolution of Carbon Dioxide in Porous Media

by

Yu Liang, B.E.; B.S.

Thesis

Presented to the Faculty of the Graduate School of

The University of Texas at Austin

in Partial Fulfillment

of the Requirements

for the Degree of

Master of Science in Engineering

The University of Texas at Austin

December 2014

Dedication

To my parents, Yanji Liang and Xiaolin Li, and my mother country, China.

致我的父母，梁延基和李晓琳。致我的祖国，中国。

“一万年来谁著史，三千里外欲封侯。”

Acknowledgements

I would like to thank my advisors David DiCarlo and Marc Hesse who have provided the best guidance and mentorship for me. Their wisdom and willingness to explore unknowns have influenced me deeply. They have set an example that I am willing to follow in the future. I am also grateful that they have created opportunities to encourage me to cooperate with other scholars.

I want to thank my undergraduate assistant Mustafa Shambulov, who has worked on this project with me for one year. I also want to thank my office mates Amir Kianinejad and Rafael Longoria. Our office has been a fantastic place for me to study knowledge, discuss topics and seek cooperation, and I will never forget their friendship.

I want to thank everyone in Dr. DiCarlo's group and Dr. Hesse's group. I have learnt a lot from the cooperation with them. Also, I would like to thank Glen Baum, Gary Miscoe, Mark Smith, Barbara Messmoreand, and Daryl Nygaard for their technical support. Especially, I want to thank Frankie Hart, who always patiently helps me with graduation issues.

Finally, I want to thank my parents for their unconditional support and endless love.

Abstract

Experimental Study of Convective Dissolution of Carbon Dioxide in Porous Media

Yu Liang, M.S.E.

The University of Texas at Austin, 2014

Supervisor: David A. DiCarlo

Geological carbon dioxide (CO2) capture and storage in geological formations has the potential to reduce anthropogenic emissions. The viability of technology depends on the long-term security of the geological CO2 storage. Dissolution of CO2 into the brine, resulting in stable stratification, has been identified as the key to long-term storage security.

The dissolution rate determined by convection in the brine is driven by the increase of brine density with CO2 saturation. Here we present a new analog laboratory experiment system to characterize convective dissolution in homogeneous porous medium. By understanding the relationship between dissolution and the Rayleigh number in homogeneous porous media, we can evaluate if convective dissolution occurs in the field and, in turn, to estimate the security of geological CO2 storage fields.

The large experimental assembly will allow us to quantify the relationship between convective dynamics and the Rayleigh number of the system, which could be essential to trapping process at Bravo Dome. A series of pictures with high resolution are taken to show the existence and movement of fingers of analog fluid. Also, these pictures are processed, clearly showed the concentration of analog fluid, which is essential to analyze the convective dissolution in detail. We measured the reduction in the convective flux due to hydraulic dispersion effect compared to that in homogeneous media, to determine if convective dissolution is an important trapping process at Bravo Dome.

TABLE OF CONTENTS

LIST OF FIGURES

LIST OF TABLES

CHAPTER 1: INTRODUCTION

1.1 OVERVIEW

Atmospheric CO_2 is one important component of the greenhouse gases which greatly affects the temperature of the Earth. Since 1750, a 40% increase in the atmospheric concentration of CO_2 has been recorded from 280 to 395.4 parts per million (ppm) in 2013 due to anthropogenic CO_2 emissions and devastations of forests (Metz, Davidson, Coninck, Loos, & Meyer, 2005). Based on current emission data, as early as 2047 the Earth's surface temperature could exceed historical records by Earth System Models, which will affect most ecosystems on the Earth (Mora, et al., 2013). Therefore, it is necessary to use artificial technology to control the atmospheric CO_2 concentration to prevent excessive temperature increasing on the Earth.

Carbon Capture and Storage (CCS) is a technology system to reduce the anthropogenic CO_2 in the atmosphere, including CO_2 capture from industry emission sources, CO_2 transportation by network of pipelines and CO_2 sequestration into storage sites. The CO_2 storage sites include depleted gas and oil reservoirs (Kovscek & Cakici, 2005), unmineable coal seams (Metz, Davidson, Coninck, Loos, & Meyer, 2005), saline aquifers (Kaarstad, 1992), deep sea sediments (House, Schrag, Harvey, & Lackner, 2006), as well as a combination between enhanced oil/methane recoveries with CO_2.storage (Bondor, 1992) (Legg, 1998). In order to mitigate climate change, Giga tons of CO_2 are required to be injected to the storage sites (Metz, Davidson, Coninck, Loos, &

Meyer, 2005). Based on current technology, implementation of CO_2 capture and storage at a large scale is technically feasible (Metz, Davidson, Coninck, Loos, & Meyer, 2005). There are four trapping mechanisms for CO_2 storage, including structural & stratigraphic trapping, residual CO_2 trapping, dissolution trapping and mineral trapping. Leakage potential is a serious problem for CO_2 storage we must consider. For example, once the cap rock is broke by activities like earthquakes, CO_2 can leak from structural & stratigraphic trapping site and come back to the atmosphere or pollute drinking water at shallower depth due to its mobility and positive buoyancy with respect to the brine, which is the scenario we must prevent. Figure 1.1 shows main trapping mechanisms for CO_2 storage, relevant trapping contributions for each mechanism and storage security.

Dissolution of CO_2 mechanism can prevent such leakages effectively. When the supercritical CO_2 is injected into the formation, it migrates upward duo to its lower density with respect to brine, until it reaches the cap rock and stays there if no disturbing activities would take place. Once CO_2 contacts the fresh brine, the dissolution process is triggered, and the density of the brines increases with the increasing saturation of CO_2, advocated by Lindeberg & Wessel –Berg (Lindeberg & Wessel-Berg, 1997). Due to the negative buoyancy, CO_2 saturated brine with a higher density migrates downward to the bottom of the reservoir as fingers form, and stays stably there for thousands of years regardless of formation destruction activities. At same time, fresh brine flows upward continually to dissolve more CO_2. The time scale for the dissolution trapping is estimated to be from hundred to thousand years. Therefore dissolution of the supercritical CO_2 into the brine in saline aquifers is a very important mechanism due to its high security and

long – term storage capacity. Figure 1.2 shows the CO_2 –rich fingers migrating downward in the porous media.

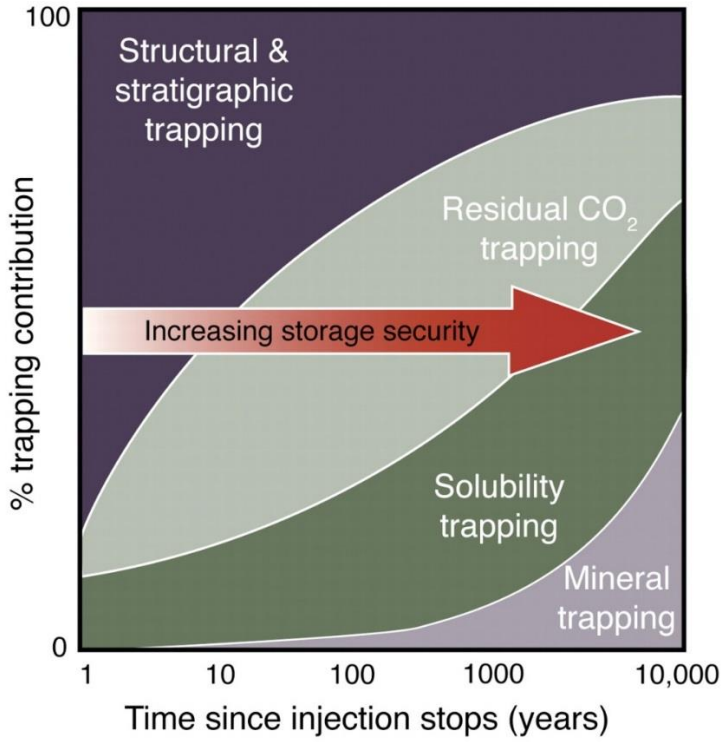

Figure 1.1 - Main trapping mechanisms for CO2 storage. Graph is modified from the documents by Metz. (Metz, Davidson, Coninck, Loos, & Meyer, 2005)

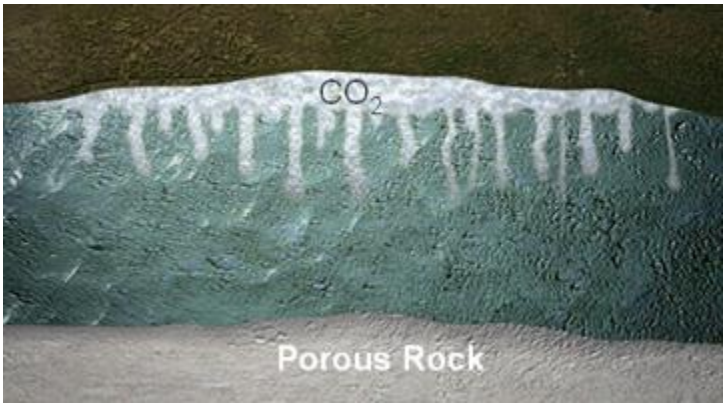

Figure 1.2 - Dissolution of CO2 into brine and heaver fingers descending migration (Metz, Davidson, Coninck, Loos, & Meyer, 2005)

1.2 RESEARCH OBJECTIVE

Since the time scale of CO_2 convective dissolution trapping mechanism is estimated to be very large, it is difficult to detect whether the convective dissolution process take place, as well as how fast it can take place. The motivation of my project is to understand the dynamics of the CO_2 convective dissolution trapping which has higher security and large long-term storage capacity. The objective of the project for my master degree is to study the CO_2 convective dissolution rate, the controlling factors which have negative or positive impact on CO_2 convective dissolution rate, and convective finger pattern.

In order to approach the objective, a novel experiment system is applied, including an analog fluid system, a porous media environment and a video capture system with an advanced image analysis technology. Currently most of relevant research is based on simulation study. Among experiment study, most of them are based on the Hele- Shaw experimental environment. Therefore, relevant experiment study in the topic is very useful and essential. My research mimic and analyze the CO_2 convective dissolution process in the porous media, and the experimental results obtained by the advanced experimental system lays a solid foundation to testify simulation works. The purpose of this thesis is to introduce the advanced experimental system and share the progress I have made. The results can be extended to field scale study of the CO_2 convective dissolution process.

1.3 CHAPTER ORGANIZATION

Chapter 2: Background and literature review

- Basic introduction to the CO_2 geological storage.
- Basic introduction to the CO_2 saline aquifer storage and relevant mechanisms. Detailed explanation of the CO_2 convective dissolution process in saline aquifer.
- An overview of previous studies on CO_2 convective dissolution process by experiments and simulation.

Chapter 3: Materials and procedure

- An overview of the novel experimental systems.
- Description of how the analog fluids system is prepared and measured.
- Description of how the experimental porous media environment is prepared and measured.
- Description of how the video captures system is prepared and performed.
- Description of how the video captures system is prepared and performed.
- Description of how the CO_2 convective dissolution experiment is performed and measured.

Chapter 4: Results

- Example of how one CO_2 convective dissolution experiment is performed, how the images are captured and analyzed and how the results are calculated.

- Results of the convective dissolution rate calculation of all experiments.
- Results of the finger pattern analysis of all experiments.

Chapter 5: Discussion

- Discussion of the depended between convective dissolution rate and controlling factors.
- Discussion of the depended between convective finger pattern and controlling factors.
- Introduction of Rayleigh numbers and Sherwood numbers.
- Analysis of the experimental observations.
- Introduction of new model to describe the CO_2 convective dissolution process based on obtained experimental results.

Chapter 6: Conclusions and future work

- Conclusions of experimental observations, experimental analysis, and advocated new dynamics model.
- Recommendation of works to set up a 3-D experimental chamber with X-Ray image analysis technology and optimize the mathematical models.

CHAPTER 2: BACKGROUND AND LITERATURE REVIEW

2.1 CO_2 GEOLOGICAL STORAGE

In 1977 Marchetti (Marchetti, 1977) first published a paper to discuss geological storage as one option to reduce the anthropogenic CO_2 to solve global climate change problem. In 1989 several small-scale CO_2 tests were initialed by Statoil as a respond to a carbon tax introduced by the Norwegian Parliament, which is approximately $ 50 / ton CO_2 (Kaarstad, 1992). Since then the industry and the academia started to study and discuss potential options for geological storage with their advantages and disadvantages. Especially during the First International Conference on Carbon Dioxide Removal in Amsterdam in 1992, Storage in saline aquifer (Kaarstad, 1992), storage in depleted gas and oil reservoirs (Legg, 1998), and CO_2 combined with enhanced oil recovery technology were proposed as feasible potential geological sites for CO_2 storage (Bondor, 1992). In 2001 Stevens proposed unminable coal seams combined with enhanced coal bed methane recovery technology as another option for geological CO_2 storage (Steven, Kuuskra, Gale, & Beecy, 2001). CO_2 storage in deep sea sediments, distinct from aquifer storage due toe he neutral buoyancy and potential of a self-sealing CO_2 hydrate cap, is regarded as another potential geological site (House, Schrag, Harvey, & Lackner, 2006).

In 2006 Metz published a report, estimating the world wide CO_2 storage capacity in depleted gas and oil reservoirs 675 to 900 Gt CO_2, unminable coal seams 3 to 200 Gt CO_2, and saline aquifers 1000 to 10000 Gt CO_2 (Metz, Davidson, Coninck, Loos, & Meyer, 2005). The economic zone of the US alone is estimated to have a storage capacity of greater than 1000 Gt CO_2 (House, Schrag, Harvey, & Lackner, 2006). This capacity

may be limited by the average formation permeability and geomechanical factors (Levine, Matter, Goldberg, Cook, & Lackner, 2007). Because of the potential profit by enhanced hydrocarbon recovery, a combination of CO_2 storage and enhanced oil/ coal bed methane recovery is economically preferred, with a limited storage capacity and long distance transportation cost though. In term of storage capacity and technical feasibility, saline aquifer is a good option for CO_2 storage. However, it should be noted no economic benefits in respect to saline aquifer storage is found until now, consequently incentives such as regulations and taxes are necessary for the application of aquifer storage.

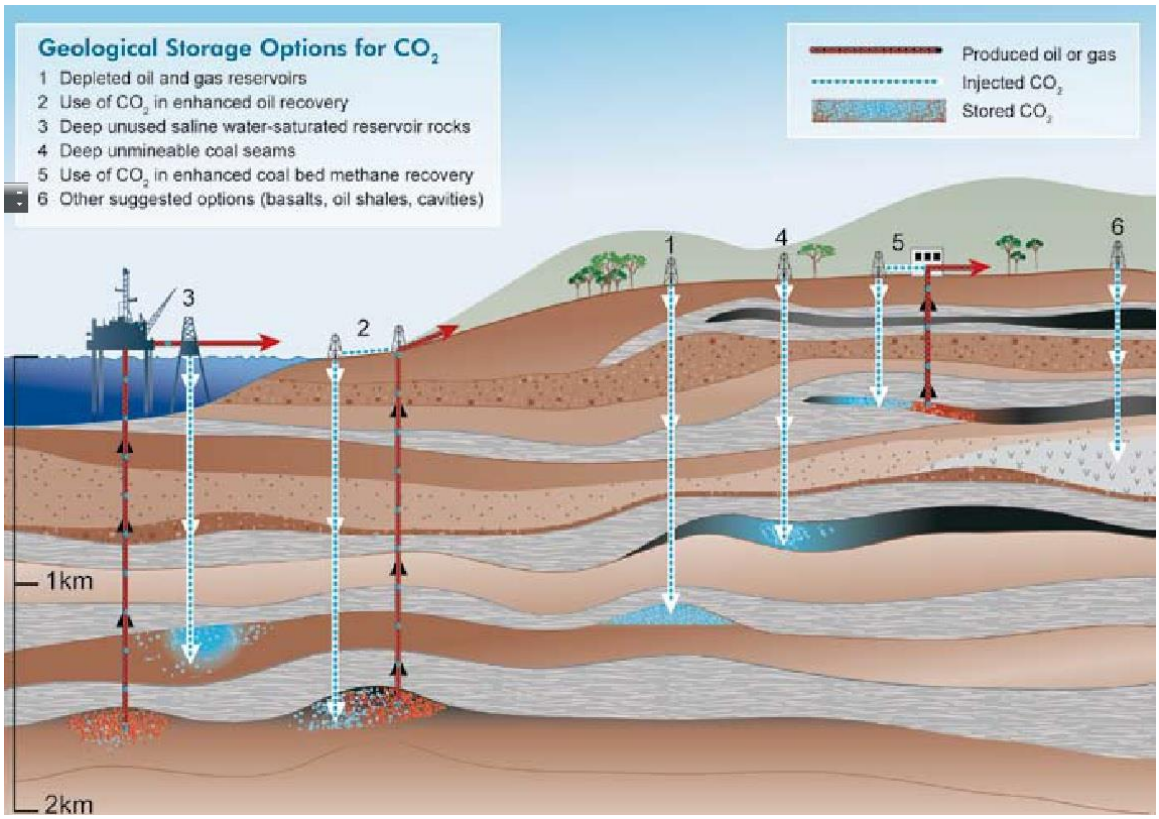

Figure 2.1 - Options for CO2 geological storage. Graph is adapted from Metz (Metz, Davidson, Coninck, Loos, & Meyer, 2005)

2.2 SALINE AQUIFER STORAGE

2.2.1 OVERVIEW

Saline aquifer refers to the deep sedimentary rocks saturated with formation water containing high salinity or brine, which cannot be used as the drinking or irritating water. Applications of high salinity formation water include low- temperature geothermal power generation (Lund, Freeston, & Boyd, 2005). Drilling slurries (Reed, Mathews, Bruno, & Olmstead, 2002), liquid radioactive water (Saripalli, Sharma, & Bryant, 2000) and hazardous chemical water (Rumynin, Konosavsky, & Hoehn, 2005) are injected into deep saline aquifer at a low fraction compared to the large volume of saline aquifers available.

For storage, carbon dioxide is injected at a depth greater than 800 m with a geothermal gradient of 25 °C / km (Holloway & Savage., 1993). This is the depth for CO_2 to stay in the supercritical state, which is less dense than brine under all meaningful storage conditions (Bachu & Stewart, Geological sequestration of anthropogenic carbon dioxide in the western canada sedimentary basin: Suitability analysis, 2002). When injected, supercritical CO_2 migrates upwards due to buoyancy until it reaches an impermeable seal, such as a clay or shale layer. Therefore it is necessary for the storage formation to have an overlying seal to prevent leakage. It should be noted that the amount of CO_2 that can dissolve into brine determines the long term storage capacity (Bachu & Adams, equestration of CO2 in geological media in response to climate change: capacity of deep saline aquifers to sequester CO2 in solution, 2003).

The timescale for CO_2 to stay mobile and buoyant in the storage formation underground is estimated to be from hundreds to thousands of years (Hesse, Tchelepi, & Orr Jr, 2006). The storage security is determined by the integrity of the overlying seals, as well as physical and chemical processes to immobilize CO_2 by negative buoyancy (Zhou, Bear, & Bensabat, 2003). Figure 2.2 shows injected CO_2 in different states and related chemical and physical process, which positively decreases CO_2 leakage possibility (Bachu & Adams, equestration of CO2 in geological media in response to climate change: capacity of deep saline aquifers to sequester CO2 in solution, 2003). The failure of seal integrity and immobilization process may result in the injected CO_2 leakage to the atmosphere (Metz, Davidson, Coninck, Loos, & Meyer, 2005).

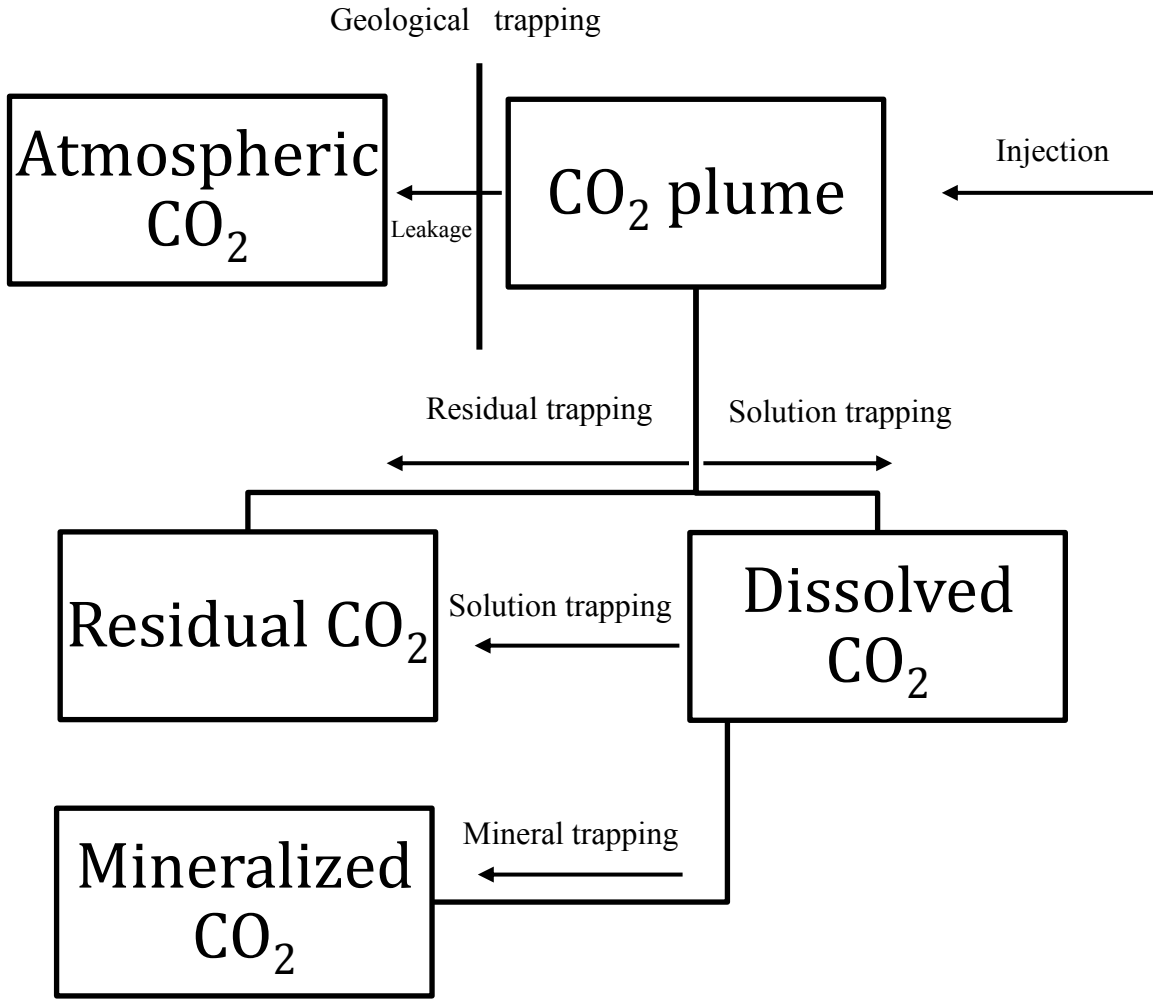

Figure 2.2 - Chemical and physical process to transfer injected CO_2 to different states. Graph is modified from Metz et al (Metz, Davidson, Coninck, Loos, & Meyer, 2005).

The general objective is to keep CO_2 in the storage formation, so leakage by the seal integrity failure and process failure should be avoided. There are three main leakage mechanisms identified by Metz *et al* (Metz, Davidson, Coninck, Loos, & Meyer, 2005), including:

- CO_2 enters the pore systems in the cap rocks with low permeability by exceeding capillary pressure
- CO_2 enters the openings in the cap rocks including fractures and faults.
- CO_2 leaks through abandoned or poorly completed wells

Especially the leakage through abandoned wells is regarded as the most possible mechanism due to the large amount in the sedimentary basin (Gasda, Bachu, & Celia, Spatial characterization of the location of potentially leaky wells penetrating a deep saline aquifer in a mature sedimentary basin, 2004).

2.2.2 TRAPPING MECHANISMS

Due to its positive buoyancy and mobility, injected CO_2 migrates upward until it reaches the impermeable overlying seal. If the integrity of seal system fails, including those three leakage mechanisms discussed above, then CO_2 may leak to atmosphere. Oppositely, any mechanism resulting in CO_2 immobilization and negative buoyancy can be identified as the CO_2 trapping mechanism. Currently there are three dynamics trapping mechanisms identified in saline aquifers (Hesse, Tchelepi, & Orr Jr, 2006).

- Residual trapping refers to the formation of residual saturation to immobilize migrating immiscible CO_2 by the capillary snap-off (Holtz, 2002). The

importance of the residual saturation in the formation is highlighted by Kumar (Kumar, et al., 2004) as the dominant trapping mechanism in saline aquifer.

- Dissolution trapping refers to the dissolution of CO_2 into brine. With CO_2 saturation increasing, brine become denser resulting in the negative buoyancy to prevent leakage of dissolved CO_2. Ennis – King (Ennis-King, Preston, & Paterson, 2005) shows that overall CO_2 dissolution rate could be increased significantly by induced convective motion.
- Mineral trapping is the precipitation process of dissolved CO_2 to form carbonate minerals. The time scale for mineral trapping process is relatively large, usually from hundreds to thousands of years (Xu, Apps, & Pruess, 2003).

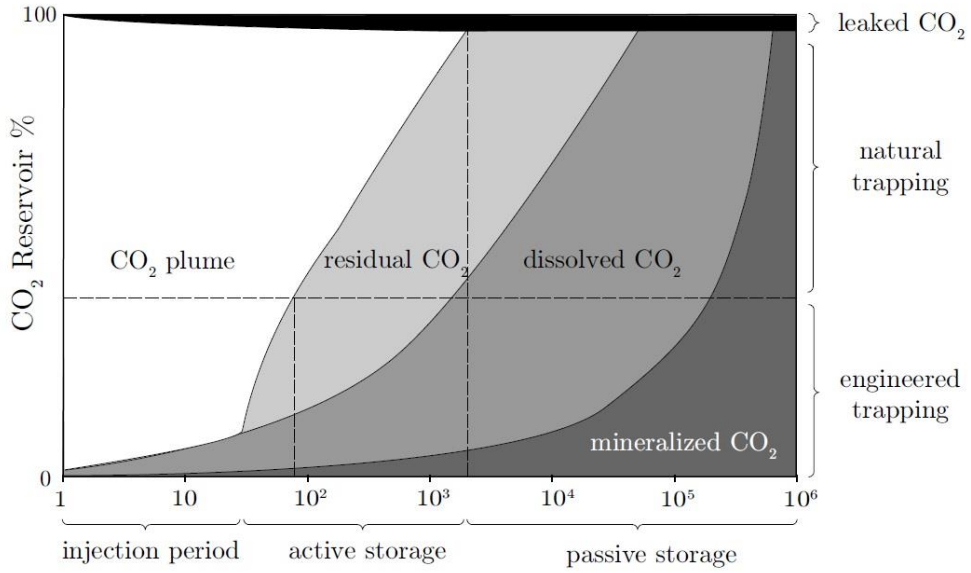

Figure 2.3 - A plot showing the evolution of the injected CO_2 in each state as a function of time. Graph is adapted from Metz (Metz, Davidson, Coninck, Loos, & Meyer, 2005).

Figure 2.3 shows the relationship between injected CO_2 in each state as a function of time. As we can observe, injected CO_2 will transfer from plume sate to mineralized state completed if timescale is long enough, which provide the permeant storage option while residual trapping and dissolution trapping are more technical feasible (Zhang, Oldenburg, & Benson, 2005).

According to the technical effectiveness, Hesse (Hesse, Tchelepi, & Orr Jr, 2006) identified direct dissolution of mobile CO_2 plume and residual trapping as the primary trapping process, and the mineralization of dissolved CO_2 and dissolution of the residual CO_2 as the second trapping process. Engineering trapping is to enhance trapping efficiency by technical methods during the injection period and some period after the injection, including water – alternating-gas injection (Kovscek & Cakici, 2005) (Juanes, Spiteri, Orr Jr., & Blunt,, 2006) (Ide, Jessen, & Orr Jr, 2007) and the circulation of brine to increase dissolution (Leonenko & Keith, 2008). Natural trapping process highly depends on the selection of storage size (Pruess, 2005). **This thesis focusses on the scenario in the natural trapping process when CO_2 plume has trapped by the geological structure, and CO_2 continues dissolving into underneath brine.**

Also, an active storage period is defined as the scenario when CO_2 is still mobile and buoyant so leakage is still possible, while a passive storage period is defined as the redistribution between two trapped phases. The time point between the active storage period and the passive storage period is used to determine the security of a geological storage site (Hesse, Tchelepi, & Orr Jr, 2006).

2.2.3 CO_2 Convective Dissolution Trapping

As the CO_2 saturates with brine, its density increases with saturation increases, resulting in the downward motions of denser CO_2- rich brine plume under reservoir conditions (Yang & Gu, 2006) (Ennis-King, Preston, & Paterson, 2005). Therefore, the duration of the active storage is determined by the dissolution of mobile and buoyant supercritical CO_2, and its dissolution rate is essential for the trapping efficiency of a CCS project. Table 2.1 shows the dissolution of CO_2 into water by Hele-Shaw experimental chamber and the CO_2- rich brine fingers can be observed flowing downward, which is in yellow and dyed by pH sensitive materials. Figure 2.4 shows the simulation results of CO_2 injection into a homogeneous formation.

Table 2.1 - Dissolution of CO_2 into water process by Hele-Shaw experimental chamber as a function of time. CO_2 is injected at the top of the chamber and continues to dissolve into underneath water

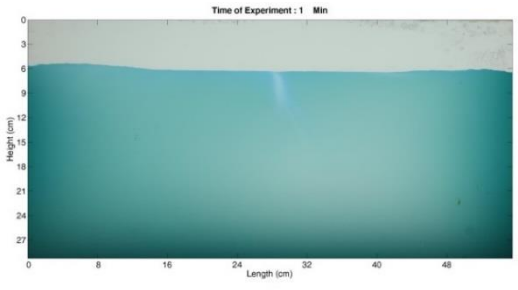	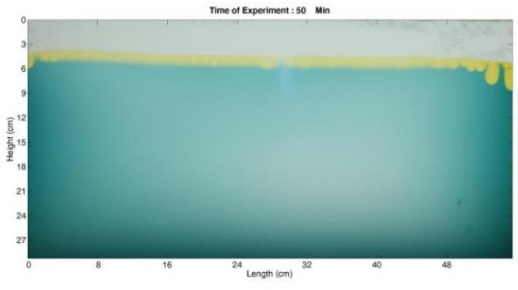
Experiment at 1 Min	Experiment at 50 Mins

Table 2.1 – Continued

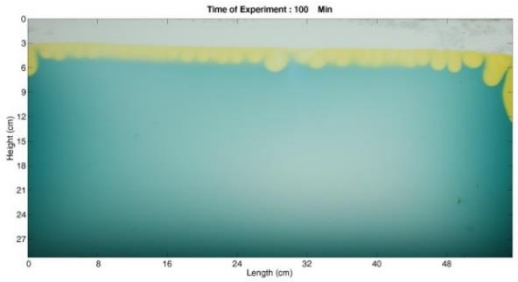	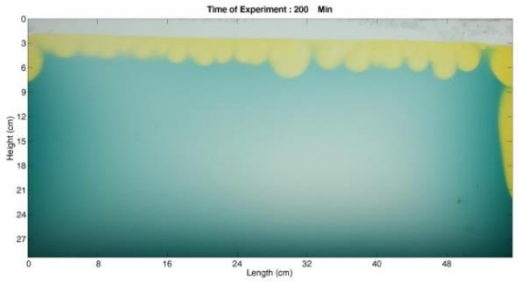
Experiment at 100 Mins	Experiment at 150 Mins
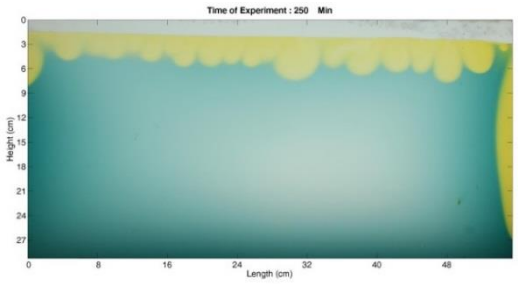	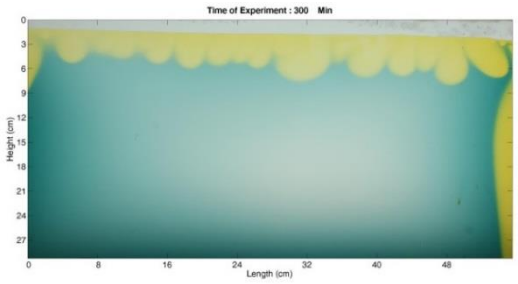
Experiment at 200 Mins	Experiment at 250 Mins
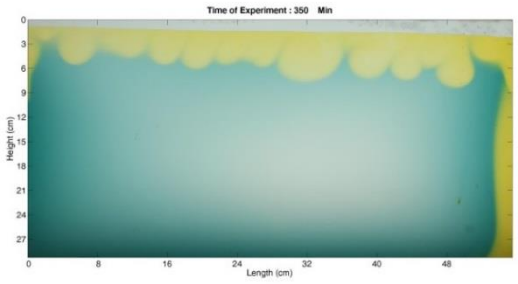	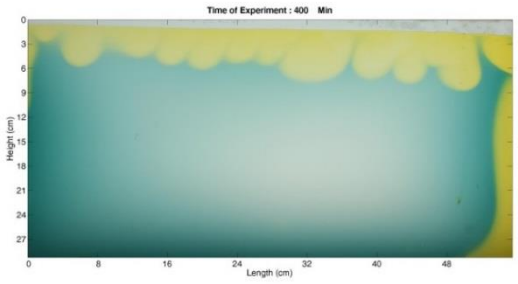
Experiment at 300 Mins	Experiment at 350 Mins

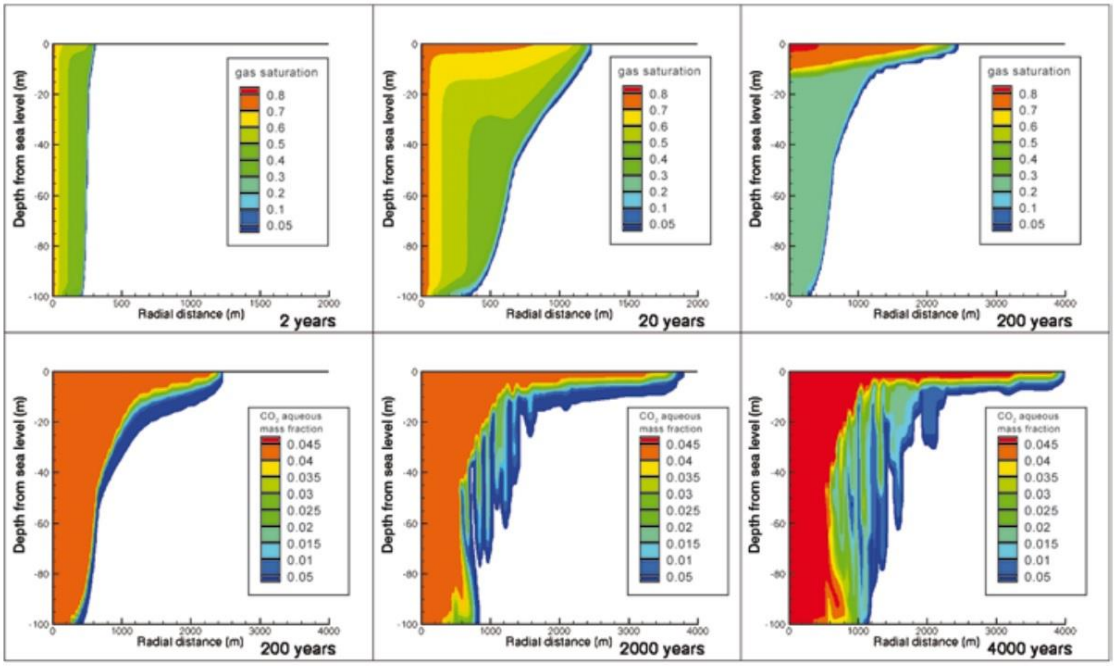

Figure 2.4 - Radial simulations of CO_2 injection into a 100 m thick homogeneous formation at a depth of 1 km with the 10 MPa pressure and 40°C temperature. The upper three parts of the figure shows gas saturation in the porous media at 2, 20 and 200 years, while the lower three parts shows the mass fraction of dissolved CO_2 on the aqueous phase at 200, 2000 and 4000 years (Ennis-King, Preston, & Paterson, 2005).

Since this thesis focuses on the scenario when supercritical CO_2 plume has ponded in the cap rock, a horizontal interface is assumed to separate supercritical CO_2 and brine, similar to the scenario in Table 2.1. Initially the dissolution rate of supercritical CO_2 at an interface is determined by molecular diffusion of dissolved CO_2 in the brine; therefore the dissolution rate is slow and decays as a function of time. The diffusive layer of CO_2 into brine grows as a function of time. Once the diffusive layer becomes thick enough, the interface will become very unstable and form denser fingers of CO_2 saturated brine

migrating downward. At the same time this downward fingers propagation brings fresh brine flowing upward convectively (Riaz, Hesse, Tchelepi, & Orr j r, 2006).Then supercritical CO_2 continues to contact convective fresh brine, the dissolution rate increases across the interface due to advection in both phases. At this stage the convective mass transport in the brine dominates the dissolution rate (Gasda, Nordbotten, & Celia, Vertically averaged approaches for CO2 migration with solubility trapping, 2011). This density – driven convection increases the dissolution rate from CO_2 to brine by several orders of magnitude (Ennis-King, Preston, & Paterson, 2005). **Therefore the objective of my thesis it study dependence between convection and dissolution rate, which in the future could be used to predict CO_2 dissolution rate by solubility trapping and to estimate the security of the long term geological CO_2 storage project.**

2.3 PREVIOUS WORK

Much effort has been made to study the convection in porous media due to the temperature or solute gradients. Numerical simulations by Linderberg & Wessel - Berg (Lindeberg & Wessel-Berg, 1997) demonstrate that the interface between CO_2 and brine stays sharp and is not disrupted by the dynamics of convective fingers in the brine, as shown in the Table 2.1. This result laid a solid foundation for the flowing models and experiments designs.

Riaz *et al*. (Riaz, Hesse, Tchelepi, & Orr j r, 2006)developed a linear stability analysis to accurately predict the critical time and the associated unstable wavenumber, based on the dominant mode of the self-similar diffusion operator. Farajzadeh *et al.* (Farajzadeh, Salimi, Zitha, & Bruining, 2007)founds that by computational simulation mass transfer increases and concentration front moves faster with Rayleigh number increasing, which is a dimensionless number depends on the characteristics of the porous media and the properties of the fluids. Neufeld *et al.* (Neufeld, et al., 2010)presented a high resolution numerical simulation, which demonstrated the convective flux scales with the Rayleigh number to the 4/5 power, rather than a linear relationship. Pau *et al.* (Pau, et al., 2010)developed a high- resolution two- dimensional simulation by block –structured adaptive mesh refinement method, and confirmed that onset time of convection follows tightly to the prediction of linear stability analysis. Gasda *et al*. (Gasda, Nordbotten, & Celia, Vertically averaged approaches for CO2 migration with solubility trapping, 2011)presented a model combining vertically integrated governing equations with an

upscaled dissolution-convection process. All these simulation studies are based on homogeneous porous media.

Some models with analytical solutions have been developed for the onset condition of density driven convection process in heterogeneous media by linear stability analysis. Especially, Farajzadeh (Farajzadeh, Salimi, Zitha, & Bruining, 2007)and Ranganathan (Ranganathan, Farajzadeh, Bruining, & Zitha, 2012) explored and discussed density- driven convection during CO_2 geological storage in the heterogeneous porous media by modeling and numerical simulation. The heterogeneity of permeability is generated by Sequential Gaussian Simulation method.

In order to testify the accuracy of modeling methods and simulation results, people also conducted a lot of experiments with image capture technique. Most of those experiments were conducted in the Hele- Shaw experimental chamber. In the Hele – Shaw cells, fluid flows through the narrow gap between two transparent plates, analogue to the flow though the porous media under Darcy's law. The CO_2 dissolution process shown in Table 2.1 is conducted in Hele- Shaw experimental chamber. Kneafsey & Pruess (Kneafsey & Pruess, 2010) presented their CO_2 solute- driven convection experiments conducted in Hele – Shaw cell. By visualizing small fingers forming process they obtained time-series data of finger lengths and wavelengths. The visualization results fit well with the modeling results conducted by Kneafsey & Pruess (Kneafsey & Pruess, 2010). Backhaus *et al.* (Backhaus, Turitsyn, & Ecke, 2011), Slim *et al*. (Slim, Bandi, Miller,, & Mahadevan, 2013), Tsai *et al.*(Tsai, Riesing, & Stone, 2013), Khosrokhavar *et al.* (Khosrokhavar, Elsinga, Farajzadeh, & Bruining, 2014)and Faisal *et*

al. (Faisal, Chevalier, Bernabe, Juanes, & Sassi, 2015) also investigated qualitative and quantitative study of the convective instability and mass transport of diffusion layers in a Hele – Shaw geometry, which can be used to determine time scales and convective dissolution rate in the CO_2 geological storage .

The advantage of Hele- Shaw experimental cell includes better visualization effect and controllable permeability. However, CO_2 convective dissolution process takes place in the porous media, so Hele- Shaw cell may hide some physics which could have negative or positive impact on the dynamics of convective dissolution. Currently, very few experiments are conducted in the porous media.

Farajzadeh *et al*. (Farajzadeh, Salimi, Zitha, & Bruining, 2007)injected CO_2 into the sand pack to measure its pressure change in order to calculate CO_2 dissolution rate. Neufeld *et al.* (Neufeld, et al., 2010) used analog fluids to conduct convective dissolution experiments in a thin chamber filled with glass beads, which created a 2-D porous media. To my knowledge, no new research is conducted in the porous media currently.

In my studies, I use an analog fluid systems of methanol and ethylene-glycol, and water to mimic the density behaviors of supercritical CO_2 and brine. Different size glass beads are used to create a homogenous porous media where convective dissolution can take place. A video capture system combined with the image analysis method is used to calculate convective dissolution rate and to analyze finger pattern.

CHAPTER 3: MATERIALS AND EXPERIMENTAL PROCEDURES

3.1 OVERVIEW OF EXPERIMENT

In order to study the hydrodynamic CO_2 convective dissolution mechanism by experimental methods, I use an analog fluid system to mimic supercritical CO_2 dissolution into brine, and analog fluid is placed into a porous media, which is packed by glass beads. Once the analog fluid contacts water, the convective dissolution is triggered. A video capture system is also set up to record every moment of the whole experiment process. After the experiment, a series of experimental images is processed for different analysis purposes. As we can expect, the dissolution dynamics can be impacted and controlled by the properties of analog fluids system and the properties of the porous media. Therefore, it is necessary to measure fluid density, fluid viscosity, porosity and permeability before the dissolution experiment to analyze these controlling factors. A full convective dissolution experiment does not only mean the dissolution dynamics measurement itself; it also include experimental plan determination, analog fluid system preparation, analog fluid properties measurement, porous media properties measurement, image processing and so on. Figure 3.1 shows the logic of convective dissolution experiment procedure.

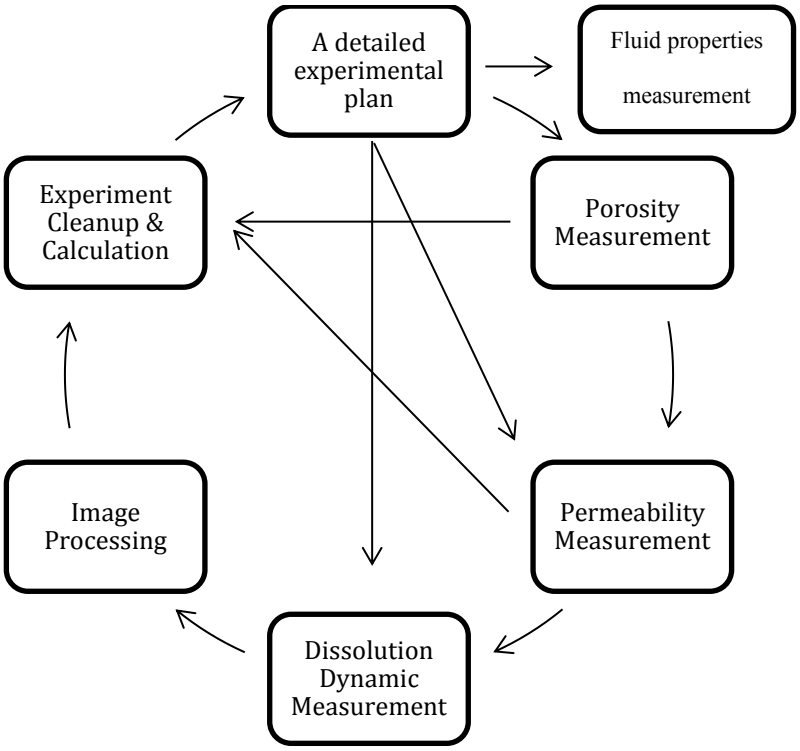

Figure 3.1 - Logic of convective dissolution experiments in the porous media. The measurement combination for one experiment is determined by the measurement purpose. Therefore a detailed experimental is essential for maximum efficiency.

3.2 ANALOG FLUIDS SYSTEM

As we know, supercritical CO_2 is buoyant with respect to water. Once water saturates with CO_2, it forms a denser interface of mixture of CO_2 and water. With more and more CO_2 dissolves into water, the density of mixture also increases, eventually will be higher than density of water. Then it will convect plumes flowing downward until it dissolves out of the bottom. Similarly, in a geological CO_2 storage field, as brine saturates with CO_2, the density of the mixture will increase and finally exceed the density of brine, which lead the vertical convective dissolution fingers flowing downward to the bottom of the reservoir, and stay there safely for millions of years. Here, I present an analog fluids system that has similar density behavior to CO_2 and water at ambient pressure and temperature.

3.2.1 METHANOL AND ETHYLENE-GLYCOL

Methanol, also known as methyl alcohol (CH3OH) is the simplest alcohol. It is a volatile and colorless liquid at ambient temperature with a density of $0.7918 g/cm^3$. Ethylene-glycol (HOCH2CH2OH) is a colorless, odorless, toxic and viscous liquid at ambient temperature with a density of $1.1132 g/cm^3$. Methanol and ethylene-glycol are mixed together by a certain weight ratio to obtain our analog fluid (MEG) to mimic the density behavior of CO_2. The density of pure MEG varies according to different methanol/ ethylene- glycol weight ratio. Four types of MEG, with the weight ratio 40: 60, 37: 63, 35: 65 and 33: 67 are made to produce different initial densities, shown as in Table 3.1.

Table 3.1 - Density of four types of MEG

MEG type	40:60	37:63	35:65	33:67
Density (g/cm^3)	0.9683	0.9786	0.9853	0.9917

When MEG dissolves into water, its density behavior are highly similar to the CO_2 – Brine density scenario. Figure 3.2 demonstrates the density behavior when water saturates MEG as a function of MEG saturation. As we can see in the plot, the Y axis represents the density of MEG - water mixture and the x axis represents the weight percentage of MEG in the MEG - water mixture; in other words, on the X axis, 1 represents pure MEG and 0 represents pure water. The water for experiment use is made with NaCl and deionized water with a 0.003% concentration, which is analog to brine. De-ionized (DI) water is filtered by a Barnstead Nanopure filtration system, and sodium chloride is manufactured from Fisher Scientific brand.

The density of pure MEG is lower than the density of water. As the MEG mixes with water, which mimics the process of CO2 dissolving into brine, the density of MEG-water mixture first increases gradually, eventually exceeding the density of water. At a certain weight fraction, its density reaches the maximum values; this max value is used for the mechanism analysis. After the peak, the density of MEG-water decreases and finally becomes the density of pure water as the weight fraction equals to zero.

Different types of MEG have the similar density behavior trends even though their initial densities are different. In addition, the maximum density value and related

weight fraction is also determined by MEG types. As shown in Figure 3.2, the maximum density of MEG type 1 represented as blue color curve is higher than the maximum density MEG type 2 represented as green color curve. It can be predicted that MEG convective dissolution rate increases with the maximum density of mixture increases.

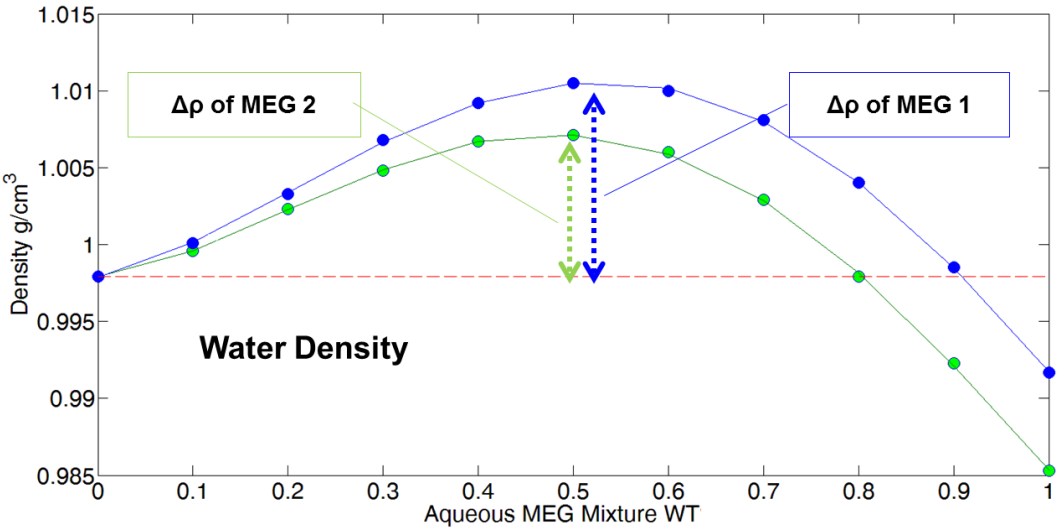

Figure 3.2 - Density behavior of MEG and water mixture

3.2.2 MEASUREMENT OF DENSITY

As discussed above, the density difference between CO_2 and water is the driving force for CO_2 convective dissolution process. Therefore I use MEG and water as the analog fluids system to CO_2 and brine due to their similar density behaviors. Four types of MEG with weigh fractions of 33:67, 35:65, 37:63 and 40: 60 are mixed with water to

measure the density of MEG-water mixture at each water fractions by the densitometer, Anton Paar DMA 35. After that the maximum density difference and corresponding water fraction can be obtained

3.2.2.1 Density Measurement Procedure

In order to obtain the MEG– water mixture density, first mix methanol with ethylene-glycol to get pure MEG. As discussed above, the methanol to ethylene-glycol ratio by weight for dissolution experiment application are 40:60, 37:63, 35:65, 33:67 with an increasing initial density trends. Put a magnetic stirring bar into the MEG container to obtain a highly homogeneous fluid, and then use the densiometer to measure corresponding densities for four types of pure MEG. Figure 3.3 shows the equipment required to obtain the pure MEG and MEG-water mixture.

After that, pure MEG and DI water are mixed together in a vial to obtain a series samples of mixture of MEG and water. A vial can hole approximately 25 g fluid. Then by calculation corresponding water amount is added to get target solution with the required water weight fraction while the total weight of the MEG – water mixture is equal to 25 g. Table 3.2 demonstrates required water weight and required MEG weight for different types of MEG to obtain the MEG-water mixture samples. It should be noted that a pipette is used to inject fluid accurately. It should also be noted that a stirring bar is put into the vial to make the fluid highly homogeneous which is essential for accuracy of analysis results.

Table 3.2 - Required water and MEG amounts to obtain mixture samples at different MEG fractions for four types of MEG

MEG Type	40 : 60		37 : 63		35 : 65		33 : 67	
MEG Wt%	Water g	MEG g	Water g	MEG g	Water g	MEG g	Water g	MEG g
100	0	25	0	25	0	25	0	25
90	2.5	22.5	2.5	22.5	2.5	22.5	2.5	22.5
80	5	20	5	20	5	20	5	20
70	7.5	17.5	7.5	17.5	7.5	17.5	7.5	17.5
60	10	15	10	15	10	15	10	15
50	12.5	12.5	12.5	12.5	12.5	12.5	12.5	12.5
40	15	10	15	10	15	10	15	10
30	17.5	7.5	17.5	7.5	17.5	7.5	17.5	7.5
20	20	5	20	5	20	5	20	5
10	22.5	2.5	22.5	2.5	22.5	2.5	22.5	2.5
0	25	0	25	0	25	0	25	0

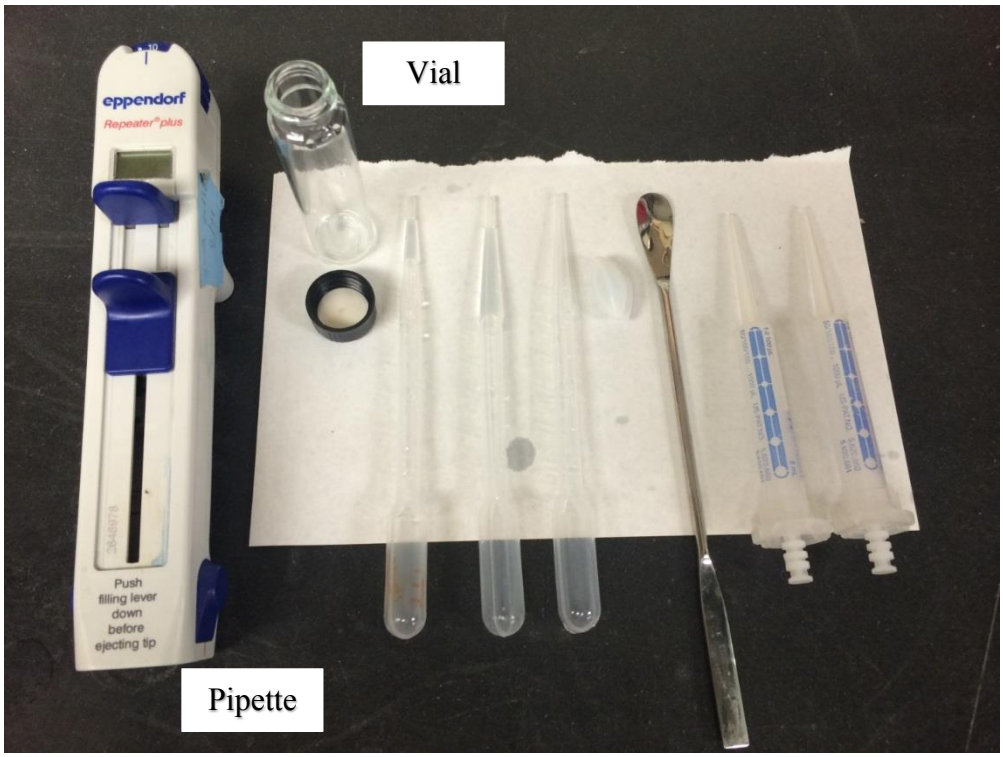

Figure 3.3 - Tools to obtain MEG-water mixture

For a specific type of MEG, there are eleven samples needs to be measured with a varying water fraction from 0% to 100%. A densitometer, Anton Paar DMA 35, as shown in Figure 3.4 is applied to measure the density of solution with different water contents. The procedure for measurement is listed below

1. Check densitometer power level.
2. Attach the plastic pipe into densitometer.
3. Press power button to turn on power.
4. Press the pump button and then put the plastic pipe into measuring fluid.
5. Release the pump button.

6. By pump pressure measuring fluid is sucked into densitometer.
7. Read density value on the digital screen.

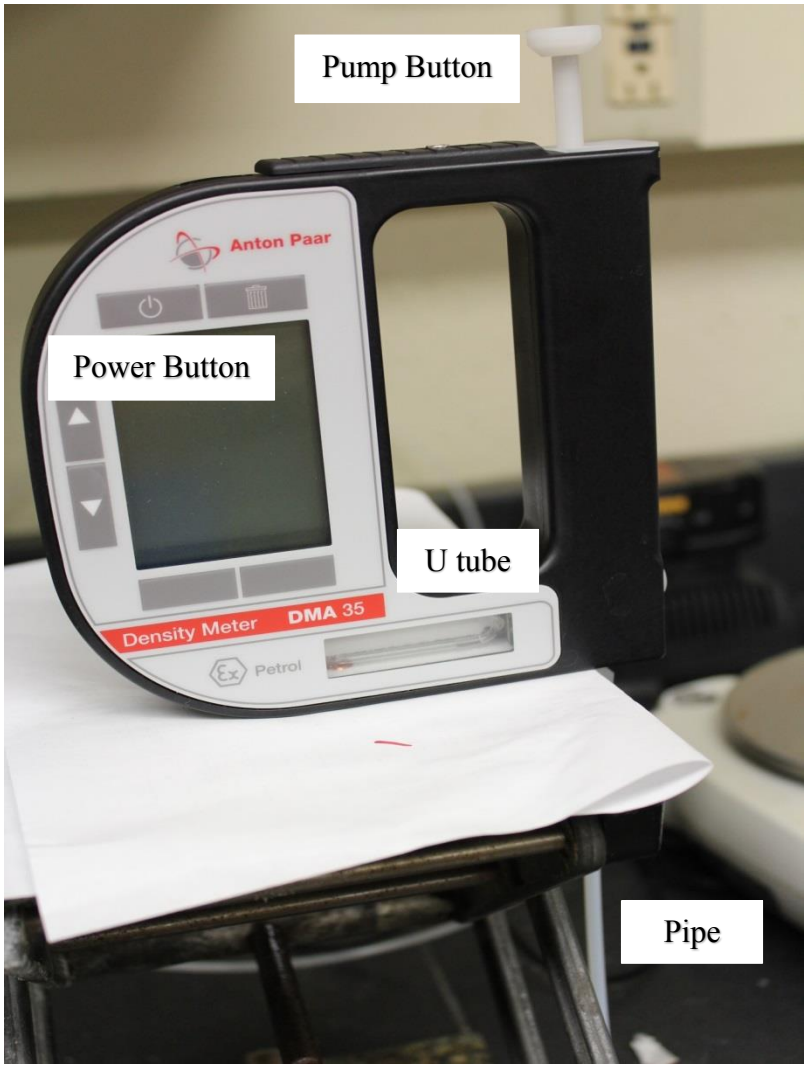

Figure 3.4 - Densitometer, Anton Paar DMA 35 is used to measure density of samples with different water fraction. A good calibration and a stable measurement environment is necessary for accuracy measurement.

Before measuring the MEG, DI water is injected to calibrate the densitometer accuracy. If output density value is in the acceptable error range which is listed on the manual, then the pure MEG can be measured and related results are recorded. It should be noted that the densitometer is placed on a stable and horizontal stage to start every measurement. Also, it is necessary to make sure no air bubble is inside plastic pipe and U tube. Otherwise the results would be highly deviated from its true density value. After measurement, acetone is injected into densitometer for clean and maintenance purpose following the same procedure. This densitometer used for the MEG density measurement, DM50, has the function to store all measured data in its own memories chip.

3.2.2.2 Density Measurement Results

By following the procedure discussed above, Table 3.3 - Density measurement results for MEG-water mixture can be obtained/

Table 3.3 - Density measurement results for MEG-water mixture

MEG WT%	MEG 33-67 $\frac{g}{cm^3}$	MEG 35-65 $\frac{g}{cm^3}$	MEG 37-63 $\frac{g}{cm^3}$	MEG 40-60 $\frac{g}{cm^3}$
100	0.9917	0.9853	0.9786	0.9683
90	0.9985	0.9923	0.9881	0.9774
80	1.004	0.9979	0.9947	0.9854
70	1.0081	1.0029	1.0002	0.9921
60	1.01	1.006	1.0035	0.9969
50	1.0105	1.0071	1.005	0.9996
40	1.0092	1.0067	1.005	1.0008
30	1.0068	1.0048	1.0039	1.0006
20	1.0033	1.0023	1.0016	0.9993
10	1.0001	0.9996	0.9995	0.9981
0	0.9979	0.9979	0.9979	0.9979

Figure 3.5 shows the measured density data for a certain type of MEG at each water fraction. As shown on the x axis, 0 represents the pure water and 1 represent the pure MEG. For the pure MEG, its density is lower than the density of water. With the water fraction increasing, the density of MEG-water mixture first increases, eventually reaches maximum value around the range between 40% to 60% water fraction, and then decreases to water density. For different MEG types, the density increases with increasing ethylene- glycol weight fraction.

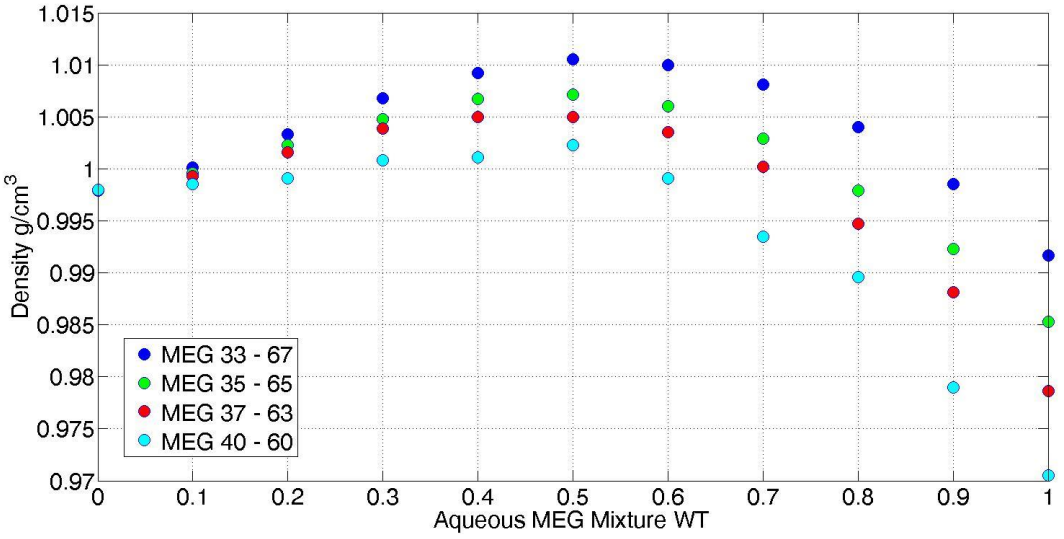

Figure 3.5 - Measured density points of MEG-water mixture samples for four types of MEG

Since the density difference between MEG and water is the driving force for convective dissolution process, it is necessary to find the related MEG-water mixture density curve and corresponding equation by existing experimental data for four types of MEG. Once the density behavior equation is obtained, then the maximum density and

corresponding water fraction can be calculated. In MATLAB, function "ployfit" and function "ployval" is used to find corresponding forth-order polynomials for four types of MEG, as shown in Figure 3.6. Red dash line represented water density, and 33-67 MEG has the largest maximum density difference, by which a highest convective dissolution rate is expected.

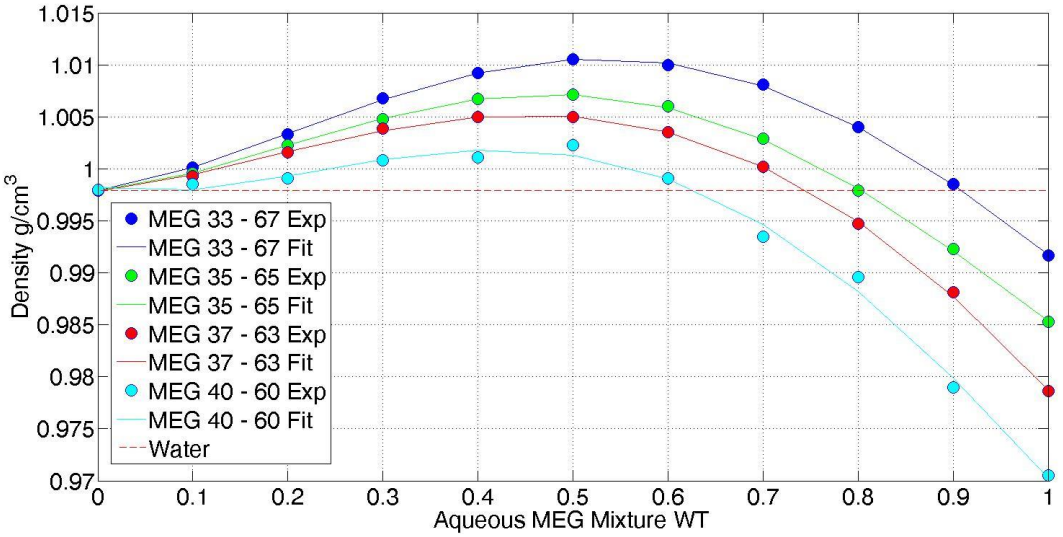

Figure 3.6 - Density fit line for MEG-water mixture measurement points by MATLAB

For each type of MEG, its density behavior can be fit back to a fourth-order polynomial by experimental density measurement data, as shown in Table 3.4. By derivative calculation, its maximum density, corresponding MEG fraction, and maximum density difference can be obtained, as shown in Table 3.5.

Table 3.4 - Fitting equations for MEG-water mixture measurement

40:60	px5 =0.092366 x^4 - 0.22512 x^3 + 0.10958 x^2 - 0.0064073 x + 0.99789
37:63	px5 =0.092366 x^4 - 0.22512 x^3 + 0.10958 x^2 - 0.0064073 x + 0.99789
35:65	px7 =0.094114 x^4 - 0.22395 x^3 + 0.10919 x^2 + 0.0080868 x + 0.99791
33:37	px8 = 0.078963 x^4 - 0.20317 x^3 + 0.10376 x^2 + 0.01429 x + 0.99787

Table 3.5 - Maximum density for MEG-water mixture, which is calculated by the obtained fitting equations

MEG type	MEG fraction regarding to maximum density	Maximum density g/cm^3	maximum density difference g/cm^3
40:60	0.3772	1.0008	0.0029
37:63	0.4554	1.0052	0.0073
35:65	0.4785	1.0072	0.0093
33:37	0.5305	1.0106	0.0127

3.2.3 MEASUREMENT OF VISCOSITY

The viscosity of a fluid is a measure of resistance to deformation to shear stress. The viscosity difference between CO_2 and water is a factor controlling the finger dynamics during convective dissolution process. As the analog fluid to CO_2 and water, the viscosity of MEG –water mixture is measured by rheometer. Four types of MEG with

weigh fractions of 33:67, 35:65, 37:63 and 40: 60 are mixed with water to obtain the viscosity of MEG-water mixture at each water fractions by the rheometer. The measurement results is used for dynamics analysis purpose.

3.2.3.1 Viscosity Measurement Procedure

The MEG-water mixture viscosity measurements are conducted by the ARES – LS1 rheometer and TA Orchestrator program in Dr. Pope's lab, shown as Figure 3.7.To measure the viscosity of the MEG-water mixture at a certain water fraction, first it is necessary to check the room temperature, which is an input for TA Orchestrator program to measure accurate viscosity. Then the rheometer should be powered on, including turning on machine, turning on fluid and opening the program '' TA Orchestrator'' with right environmental setting. Then the upper fixture should be attached gently, and offset torque and force to zero in '' Control '' tap in the program.

After the machine is warmed up, 15ml pure MEG is injected into the lower fixture by syringe. Then press ''Set Gap'' and wait for the temperature to reach the desired value. Click '' Control '' tab, set Title, Save As in '' Edit/ Start Test''. Then edit test according to the numbers in Table 3.6 - Equipment setting to measure sample viscosity.

After every value is set correctly, then select "Begin Test" to measure MEG viscosity. If everything is measured correctly, a viscosity log is plotted in the program "TA Orchestrator".

Table 3.6 - Equipment setting to measure sample viscosity

	1	2	3
Shear Rate	0	10	0
Zone time	10	50	10

Figure 3.7 - ARES – LS1 rheometer and TA Orchestrator program

After the viscosity data is obtained, it is important to clean and shut down the rheometer. First click on Gap icon to send the fixture to top, and click on control panel icon to shut down motor power. Then remove and clean upper and lower fixtures by acetone, water and air. Finally turn off the fluid bath and machine, and record the usage in the LOG file.

The procedure discussed above is the viscosity measurement for one MEG-water mixture sample. For each sample measurement, the viscosity is measured thirteen times to get the average viscosity value. Since four types of MEG with weigh fractions of 33:67, 35:65, 37:63 and 40: 60 are used as the analog fluids. For each type of MEG, there are eleven samples needs to be measured with a varying water fraction from 0% to 100%. Therefore totally there are forty-four samples to be measured by ARES – LS1 rheometer and TA Orchestrator program.

3.2.3.2 Viscosity Measurement Results

Following the viscosity measurement steps discussed above, the viscosity of four types of MEG-water mixture with different water fractions can be measured, as shown in Table 3.7, Table 3.8, Table 3.9 and Table 3.10. Table 3.11 shows the average viscosity of four types of MEG and

Figure 3.8 shows corresponding relationship between viscosity and MEG with different weight fractions.

Table 3.7 - Measured viscosity of 33-67 MEG

33-67 MEG, MEG wt%	100	90	80	70	60	50	40	30	20	10
Viscosity of #1 (cp)	3.25	3.43	3.81	2.72	3.05	2.18	2.03	2.51	1.98	1.06
Viscosity of #2 (cp)	3.21	3.58	3.65	2.86	3.02	2.27	2.18	1.92	2.46	0.77
Viscosity of #3 (cp)	3.43	3.46	3.70	3.05	3.20	2.42	2.24	2.02	2.18	1.27
Viscosity of #4 (cp)	3.38	3.53	3.54	3.05	3.29	2.41	2.16	1.95	2.07	1.17
Viscosity of #5 (cp)	3.40	3.53	3.42	3.16	3.28	2.48	2.17	1.91	1.82	1.14
Viscosity of #6 (cp)	3.39	3.53	3.40	3.16	3.30	2.50	2.14	1.83	1.67	1.16
Viscosity of #7 (cp)	3.42	3.53	3.38	3.17	3.30	2.49	2.10	1.82	1.59	1.16
Viscosity of #8 (cp)	3.51	3.63	3.49	3.28	3.45	2.59	2.22	1.88	1.58	1.22
Viscosity of #9 (cp)	3.52	3.65	3.48	3.30	3.44	2.60	2.23	1.87	1.54	1.21
Viscosity of #10 (cp)	3.52	3.65	3.47	3.29	3.45	2.61	2.22	1.87	1.53	1.22
Viscosity of #11 (cp)	3.53	3.65	3.48	3.30	3.46	2.62	2.23	1.88	1.53	1.24
Viscosity of #12 (cp)	3.55	3.66	3.50	3.33	3.48	2.64	2.26	1.90	1.55	1.26
Viscosity of #13 (cp)	3.60	3.70	3.54	3.37	3.52	2.68	2.30	1.93	1.57	1.29
Average of #1 to # 13 (cp)	3.44	3.58	3.50	3.18	3.33	2.51	2.19	1.90	1.77	1.17

Table 3.8 - Measured viscosity of 35-65 MEG

35-65 MEG, MEG wt%	100	90	80	70	60	50	40	30	20	10
Viscosity of #1 (cp)	3.12	3.37	3.14	2.84	4.08	1.80	2.41	1.61	1.42	0.93
Viscosity of #2 (cp)	3.47	3.33	3.27	2.89	3.38	2.40	2.08	1.81	1.25	1.69
Viscosity of #3 (cp)	3.55	3.50	3.32	2.93	3.29	2.30	2.16	1.63	1.49	1.12
Viscosity of #4 (cp)	3.51	3.42	3.35	3.09	3.17	2.45	2.17	1.67	1.34	1.24
Viscosity of #5 (cp)	3.50	3.50	3.38	3.08	3.06	2.39	2.17	1.76	1.44	1.15
Viscosity of #6 (cp)	3.52	3.53	3.39	3.09	3.00	2.48	2.15	1.80	1.41	1.19
Viscosity of #7 (cp)	3.52	3.56	3.41	3.16	2.95	2.50	2.17	1.80	1.45	1.17
Viscosity of #8 (cp)	3.61	3.63	3.49	3.22	2.98	2.55	2.20	1.83	1.47	1.19
Viscosity of #9 (cp)	3.61	3.64	3.51	3.24	2.98	2.57	2.21	1.84	1.48	1.19
Viscosity of #10 (cp)	3.62	3.64	3.51	3.26	2.97	2.58	2.22	1.86	1.50	1.20
Viscosity of #11 (cp)	3.64	3.65	3.51	3.27	2.98	2.59	2.23	1.87	1.51	1.22
Viscosity of #12 (cp)	3.65	3.67	3.53	3.29	3.00	2.61	2.26	1.90	1.54	1.24
Viscosity of #13 (cp)	3.69	3.71	3.56	3.33	3.04	2.66	2.29	1.93	1.57	1.27
Average of #1 to # 13 (cp)	3.56	3.55	3.43	3.14	3.07	2.49	2.18	1.80	1.44	1.24

Table 3.9 - Measured viscosity of 37-63 MEG

37-63 MEG, MEG wt%	100	90	80	70	60	50	40	30	20	10
Viscosity of #1 (cp)	4.14	3.85	3.71	3.22	3.34	2.91	2.53	2.18	1.42	0.93
Viscosity of #2 (cp)	4.09	4.07	3.93	3.65	3.18	2.80	2.44	2.05	1.25	1.69
Viscosity of #3 (cp)	3.95	3.97	3.77	3.77	3.08	2.63	2.19	1.95	1.49	1.12
Viscosity of #4 (cp)	3.92	3.98	3.83	3.60	3.00	2.65	2.19	1.93	1.34	1.24
Viscosity of #5 (cp)	3.90	3.93	3.83	3.49	2.99	2.57	2.19	1.89	1.44	1.15
Viscosity of #6 (cp)	3.87	3.90	3.86	3.45	2.98	2.57	2.20	1.86	1.41	1.19
Viscosity of #7 (cp)	3.87	3.87	3.82	3.37	2.96	2.56	2.19	1.85	1.45	1.17
Viscosity of #8 (cp)	3.94	3.98	3.89	3.45	3.03	2.61	2.22	1.87	1.47	1.19
Viscosity of #9 (cp)	3.94	3.98	3.91	3.44	3.03	2.61	2.23	1.87	1.48	1.19
Viscosity of #10 (cp)	3.95	3.98	3.91	3.43	3.04	2.61	2.25	1.88	1.50	1.20
Viscosity of #11 (cp)	3.95	3.98	3.92	3.44	3.05	2.62	2.26	1.90	1.51	1.22
Viscosity of #12 (cp)	3.98	4.00	3.94	3.46	3.07	2.65	2.28	1.92	1.54	1.24
Viscosity of #13 (cp)	4.02	4.03	3.98	3.51	3.11	2.69	2.32	1.96	1.57	1.27
Average of #1 to # 13 (cp)	3.94	3.97	3.87	3.51	3.04	2.63	2.24	1.91	1.44	1.24

Table 3.10 - Measured viscosity of 40-60 MEG

40-60 MEG, MEG wt%	100	90	80	70	60	50	40	30	20	10
Viscosity of #1 (cp)	3.67	3.26	3.08	3.48	3.18	2.34	1.75	2.28	2.04	1.32
Viscosity of #2 (cp)	3.46	3.55	3.08	3.09	3.20	2.27	1.87	1.74	1.02	1.07
Viscosity of #3 (cp)	3.31	3.58	3.06	3.08	2.95	2.33	1.88	1.88	1.27	1.20
Viscosity of #4 (cp)	3.28	3.56	3.09	3.00	2.93	2.31	1.99	1.80	1.17	1.22
Viscosity of #5 (cp)	3.17	3.51	3.10	3.01	2.84	2.31	2.06	1.82	1.27	1.18
Viscosity of #6 (cp)	3.13	3.52	3.10	3.02	2.86	2.30	2.08	1.81	1.24	1.19
Viscosity of #7 (cp)	3.11	3.50	3.10	2.99	2.82	2.30	2.10	1.79	1.29	1.17
Viscosity of #8 (cp)	3.17	3.61	3.20	3.09	2.90	2.33	2.14	1.81	1.27	1.18
Viscosity of #9 (cp)	3.15	3.59	3.21	3.07	2.89	2.33	2.17	1.82	1.28	1.18
Viscosity of #10 (cp)	3.14	3.59	3.21	3.09	2.89	2.34	2.18	1.82	1.29	1.19
Viscosity of #11 (cp)	3.15	3.60	3.22	3.09	2.90	2.35	2.21	1.83	1.30	1.21
Viscosity of #12 (cp)	3.16	3.61	3.24	3.11	2.92	2.37	2.23	1.86	1.32	1.23
Viscosity of #13 (cp)	3.20	3.65	3.28	3.14	2.95	2.41	2.27	1.89	1.34	1.26
Average of #1 to # 13 (cp)	3.20	3.57	3.14	3.06	2.92	2.32	2.08	1.81	1.25	1.18

Table 3.11 - Average viscosity of four types of MEG with different water fractions

MEG wt%	100	90	80	70	60	50	40	30	20	10
33-67 (cp)	3.44	3.58	3.50	3.18	3.33	2.51	2.19	1.90	1.77	1.17
35-65 (cp)	3.56	3.55	3.43	3.14	3.07	2.49	2.18	1.80	1.44	1.24
37-63 (cp)	3.94	3.97	3.87	3.51	3.04	2.63	2.24	1.91	1.44	1.24
40-60 (cp)	3.20	3.57	3.14	3.06	2.92	2.32	2.08	1.81	1.25	1.18

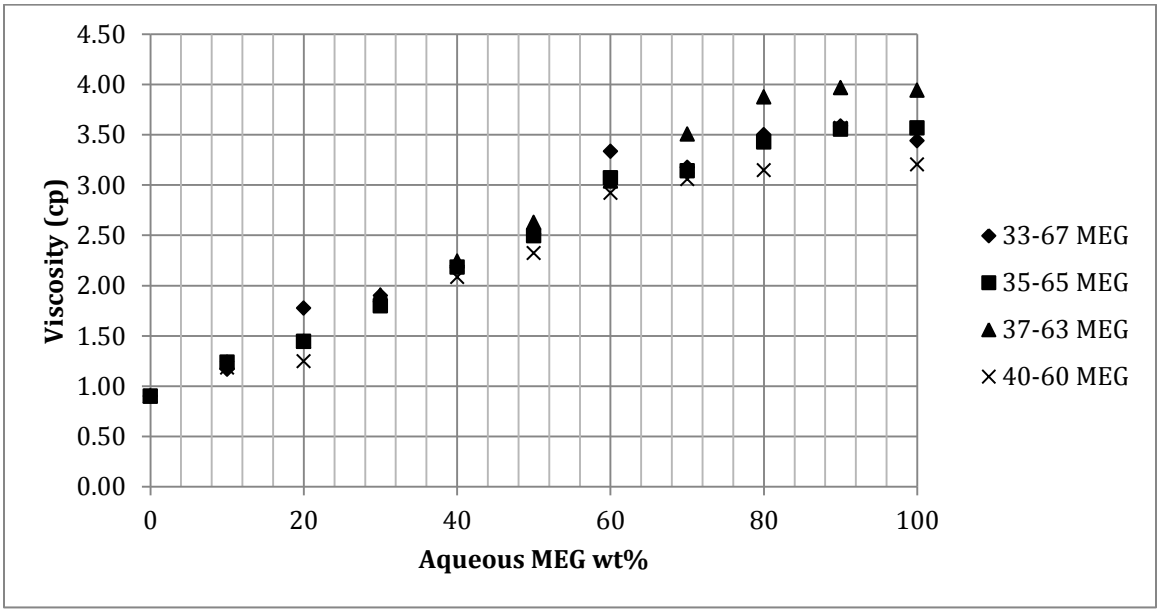

Figure 3.8 - Plot of MEG average viscosity vs. MEG with Water fractions

The measured viscosity data for a certain type of MEG at each water fraction are shown in Figure 3.8. On the x axis, 0 represents the pure water and 100% represent the pure MEG. For the pure MEG, its viscosity is higher than the viscosity of water. With the water fraction increasing, the viscosity of MEG-water mixture has a linear decreasing relationship. For different type of MEG, the viscosity increases with ethylene- glycol weight fraction increasing

When MEG dissolves into water, initially a diffusive layer is formed by the diffusion effect between MEG and water. When the diffusive layer become thick enough, instability across the layer triggers the descending MEG-rich water plume. It is the pure MEG that determine the onset of instability. Therefore, an average value of viscosity of four types of pure MEG, 3.2 cp is used for the dynamics analysis purpose.

3.3 EXPERIMENTAL ENVIRONMENT

In a natural CO_2 storage reservoir, the convective dissolution processes take place in the porous media environment, with small permeability and porosity. For previous dissolution experiments, most of them were conducted in a Hele-Shaw chamber (Kneafsey & Pruess, 2010), a system contains two thick plates and the fluid dynamics take place in the slit between the plates. Because the opening is so narrow that permeability is also very small, but no porosity concept exists in such a system. Only few studies were conducted in the real porous media environment (Neufeld, et al., 2010). Experiments in Hele-Shaw can present a good visualization effect; however in our case the CO_2 convective dissolution happens in the porous media environmental where grain,

pore and pore throat are also potential factors impacting the dissolution dynamics. Therefore the analysis could be affected negatively due to lack of porosity concept in Hele-Shaw chamber. In my experiment, a large size polycarbonate chamber is filled with different sizes glass beads to create a 2-D porous media environment. A camera and a laptop is used to capture every moment of the experimental process. A light box is used to provide appropriate light transmitting through the chamber during the experiment for video capture, and a fluid distributor is used to trigger the experiment with an even MEG and water interface.

3.3.1 EXPERIMENTAL CHAMBER

A large polycarbonate chamber is applied as the container for the glass beads to create a porous media environment. The length of the chamber is 74 cm, height 40 cm and thickness 2.5 cm. The assumption is that the chamber is thin enough to be considered as a 2-D experimental environment. Figure 3.9 is the schematic diagram of the chamber with its dimensions. The thickness of the experimental chamber is 2.5 cm.

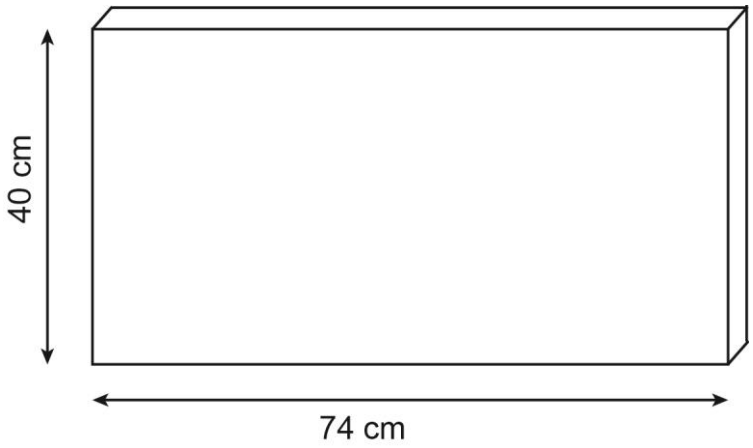

Figure 3.9 - A schematic diagram of polycarbonate chamber

Under the chamber there are five valves distributing symmetrically, which are applied as the drainage system to clean the chamber, as well as to control the water level. Another application of the valves is to measure the permeability of the chamber, similar to the Darcy experiment. Also, there is a screening mesh 2.5 cm above the bottom of chamber, which is used as a highly permeable holding plate to support large amount of beads standing on and to leave a void space for the fresh water, as well as MEG-water mixture, to transport vertically and horizontally. Above the chamber there is a fluid distributor to pour the MEG into porous media and trigger the dissolution experiment as a consequence, as shown in Figure 3.10.

There are several advantages for creating a large chamber to conduct convective dissolution experiments, including: First, more fingers can be observed during experiments, which is essential for the finger width analysis in the future. Second, there would be less wall effects, which leaves a negative effect on permeability measurement

and porosity measurement. Third, clearer pictures with more information can be obtained by video capture system.

3.3.2 POROUS MEDIA ENVIRONMENT

3.3.2.1 Glass Beads

To create a porous environment, soda lime glass beads are used and distributed into the experimental chamber for convective dissolution experiments due to its transparency properties. The experimental glass beads are purchased from Mo-Sci Corporation and Potters Beads. As we know, bead size determines the pore throat size, which is an essential controlling factor for permeability. Therefore we use three sizes beads including 1.2mm, 2 mm and 3mm (diameter). All of them are required to be clean and transparent, so the video capture system can record information accurately. Due to quality and color problem, 2mm and 3mm glass beads are purchased from Potters Beads, and 1.2mm beads are from Mo-Sci.

Figure 3.10 shows the experimental chamber filled with 2 mm glass beads, which is a homogeneous porous media environment. As it can be observed, there is a color difference between dry beads and wet beads to due to different refractive index. At the top there is a dark part which is the dry beads and light part at the bottom part is the beads saturated with water. Above the experimental chamber there is a cylinder fluid distributor for the experiment, which distributes MEG evenly across the glass beads.

One convective dissolution experiment used approximately 20 lbs. beads. After each experiment, this large amount of experimental beads are distributed into a cleaning

bucket and flushed by tap water to clean the residual MEG. The cleaning bucket is a plastic bucket with an artificial hole. Below the hole a replaceable square mess is attached to the bucket to hold the beads while water is flushing. An oven and two fans are used to dry beads after flushing. The oven is a forced air oven from Cascade Tek with a microprocessor control and the fan is from McMaster-Carr.

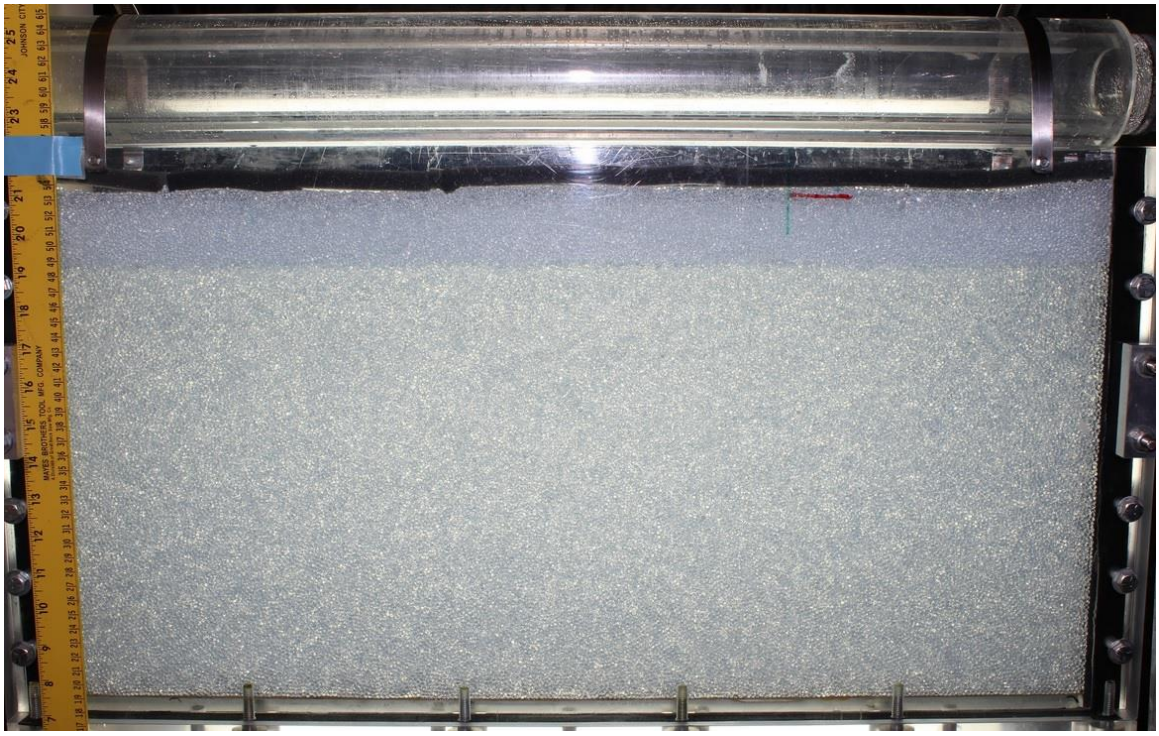

Figure 3.10 - Experimental chamber is filled with 2mm glass beads

3.3.2.2 Porosity Determination

Porosity ϕ is defined as a ratio of pore volume to bulk volume. For this dissolution experiments, uniform glass beads are used to create a homogeneous porous

media. Theoretically, the porosity for cubical packing is 47.6% and porosity for rhombohedra packing is 25.96%, as shown in Figure 3.11. For glass-beads-packing porous media environment, beads size is a controlling factor to determine permeability. As a result, it is necessary to measure the actual porosity of glass beads porous media. It should be noted that porosity made by the uniform spheres is independent of radius while permeability made by the uniform spheres, well sorted in other words, is dependent of radius. Equation 1 is the equation to calculate porosity.

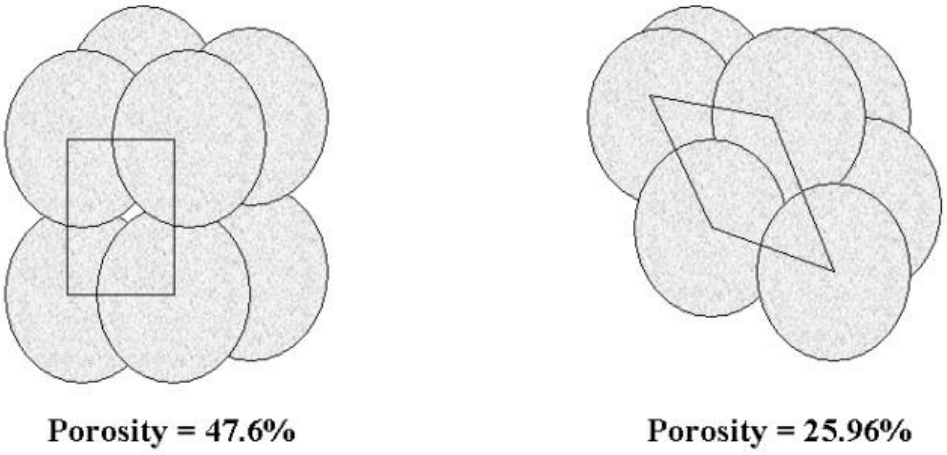

Figure 3.11 - A schematic diagram of porosity of glass-bead-packing porous media

$$\phi = \frac{V_P}{V_B} \qquad (1)$$

Where V_P is pore volume and V_S is solid volume.

3.3.2.2.1 Porosity Measurement Procedure

In order to measure the porosity, the procedures are listed below

1. Measure a certain amount of water, usually 1 L volume.
2. Close all five valves at the bottom of experimental chamber.
3. Turn on the light box.
4. Pour measured DI water into experimental chamber, record water level H_1.
5. Distribute a certain size of glass beads into experimental chamber by funnel evenly and stably until beads level reaches water interface level, record water level H_2.
6. Continue to distribute glass beads to measure permeability and dissolution dynamics.

Figure 3.12 shows this porosity measurement procedure. Then the porosity can be calculated by Equation 2

$$\phi = \frac{V_P}{V_B} = \frac{H_1 * L * W}{H_2 * L * W} = \frac{H_1}{H_2} \quad (2)$$

Where L is the length of the experimental chamber, 74 cm, and W is the width of chamber gap, 2.5 cm. H_1 and H_2 are measured water level.

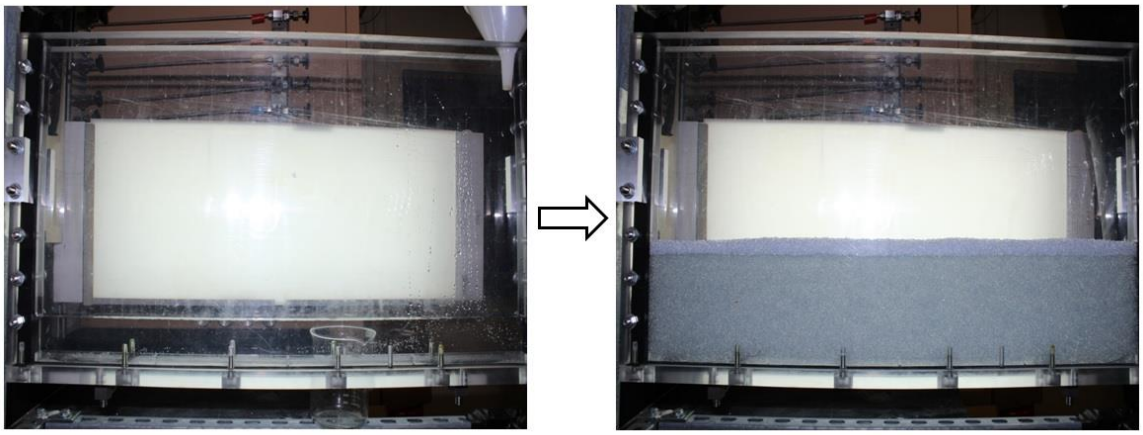

Figure 3.12 - Porosity measurement procedure, the general idea is to measure water displacement after filling the chamber with glass beads.

3.3.2.2.2 Porosity Measurement Results

As discussed above, porosity of the experimental system is measured by fluid displacement method and Equation 2. By measuring water raising level the porosity can be calculated. Take one experiment porosity measurement as an example, shown as in Figure 3.12. In the experimental chamber, 2mm size beads are distributed. On left the water level can be used to calculate pore volume. On right the water level can be used to calculate bulk volume. The porosity measurement results are listed in Table 3.12 - Porosity measurement results.

Table 3.12 - Porosity measurement results

	# 1 measurement		# 2 measurement		# 3 measurement	
Length cm	74.082	73.918	74.000	73.918	73.959	74.100
Width cm	2.500	2.500	2.500	2.500	2.500	2.500
Depth cm	5.378	12.977	5.531	13.032	5.722	13.070
Volume cm^3	996.061	2398.171	1023.184	2408.321	1058.025	2421.298
Calculated Porosity		0.415		0.425		0.437
Average Porosity		0.426				

The calculation results show the average porosity of glass beads packing porous media is 42.6%, which is in the expected ranges. The average porosity is used in the analysis of the dissolution dynamics. Also, it is used to estimate required glass beads to purchase. For example, the total value of experimental chamber is 7400 cm^3 with an average porosity of 42.6%. Therefore, the beads volume required for one experiment is 7400 * (1 – 0.426) = 4250cm^3. Soda lime, with a density of 2.5g/cm^3, is used as the materials to manufacture glass beads. Therefore, the beads weight for one experiment is 10.625 kg. This calculation result can be applied as a reference to purchase glass beads and MEG. It should be noted that porosity of the homogeneous porous media which is make be same size beads is independent of bead size.

3.3.2.3 Permeability Determination

Permeability is a measure of the ability of a porous media to allow fluid to pass through it, defined by Darcy's law. For dissolution experiment, it is a single phase flow process. Therefore, Darcy's law for single phase flow in differential form is

$$v = \frac{k}{\mu}\frac{dP}{dx} \tag{3}$$

Where v is the superficial fluid flow velocity through porous media (m/s), k is the permeability of porous media (m^2), μ is the dynamic viscosity of the fluid (Pa*s), dP is the pressure difference (Pa), dx is the length of applied pressure objective (m).

Figure 3.13 illustrates the classic Darcy permeability measurement method. When fluid flows through the sand pack, a hydraulic pressure difference between top and bottom of sand pack can be measured. The hydraulic pressure at top and bottom can be calculated by vertical heights from the datum level.

Then equation (3) can be modified to

$$k = v\mu\frac{L}{(\rho_w g h_1 - \rho_w g h_2)} \tag{4}$$

For our convective dissolution experiments, it is actually a single phase flow through porous media. Therefore I can use the classic Darcy's permeability measurement

method for our glass beads packing porous media. The permeability is determined by the bead size, and we use three sizes beads. Therefore it is necessary to measure the permeability by Darcy's method for each size bead. The permeability of glass beads packing porous media can be calculated by the equation (4) derived from the Darcy's law.

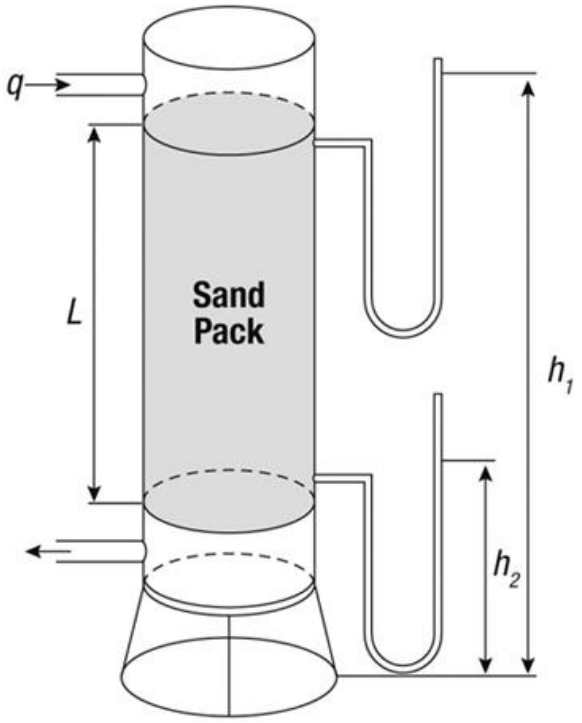

Figure 3.13 - A schematic of classic Darcy's permeability measurement method

3.3.2.3.1 Porosity measurement procedure

The general procedure for the classic Darcy's permeability measurement method for one size beads is listed below

1. Close all valves under the experimental chamber.
2. Turn on the light box.
3. Use waterproof tape to stick ruler vertically on the surface of chamber. Recommend position of ruler is 25 cm away from right side of chamber.
4. Pour 1 litter volume water into chamber.
5. Distribute a certain size of glass beads into experimental chamber by funnel evenly and stably until beads level almost reaches water interface level.
6. Repeat step 2 and step 3 until beads level is 48 cm away from table. Then add DI water until its interface reach 55 cm away from table. Vertical height can be read by the ruler in step 3.
7. Open the middle valve. The water table level in the experimental chamber should be equal to water table level in the central pipe which is connecting to the middle valve. Make sure no air bubble is inside the pipe.
8. Use waterproof tape to stick the central pipe connected to the middle valve on the surface of chamber parallel to the ruler. The distance between ruler and pipe should be as small as possible, Recommend position of vertically pipe is 22 cm away from right side of chamber.
9. Plug battery into camera, attach camera to tripod and connect camera to computer. Then turn on the camera and computer. The passcode for computer is ‘’CompData!’’.

10. Place the camera 10 cm away from the chamber. Make sure camera can work and stand stably. The relative positon of the chamber, the ruler, the central pipe and the camera is as shown in Figure 3.14.
11. Click EOS utility icon in Windows, then select remote control.
12. Estimate whether the computer has enough space for permeability measurement image capture and by checking how many pictures can be took based on current space.
13. Switch focus function into “AF” and build in flash.
14. Adjust camera setting.
15. Take the first picture manually for calibration purpose. A folder would be created automatically and named as the current date. Make sure all reading number on ruler, as well as the water interface in the experimental chamber and the water interface in the pipe can be clearly captured. Repeat step 12 – 14 until calibration picture meets a good calibration requirement, as shown in Figure 3.15.
16. Click timer function in EOS utility. Set delay time as 10 seconds, picture interval as 5 seconds.
17. Click start button to trigger camera taking pictures automatically.
18. After first picture, open the other four valves under the chamber. There should be a hydraulic height difference between water tale in the experimental chamber and the water table in the central pipe. Valves opening process should be finished quickly, stably and symmetrically.

19. Stop the camera by click ‘’stop’’ in EOS utility and close all valves when water interface in the experimental chamber recede to glass beads level.
20. Detach the ruler and the central pipe from the surface of chamber.
21. If plan to continue dissolution experiment, refer to step 7 in dissolution experiment procedure. Otherwise, drain the water, dump the beads, turn off light box, and clean the experiment environment.

After the measurement, the captured images are processed to calculate the permeability of the glass bead packing porous media. It is important to make sure beads interface is parallel to water interface when distributing the glass beads. It should be noted that all valves should be checked on a regular basis in case of drainage problem during experiments. It should be also noted that battery should be recharged immediately after experiments. In addition, the camera should be placed in a safe place after each experiment.

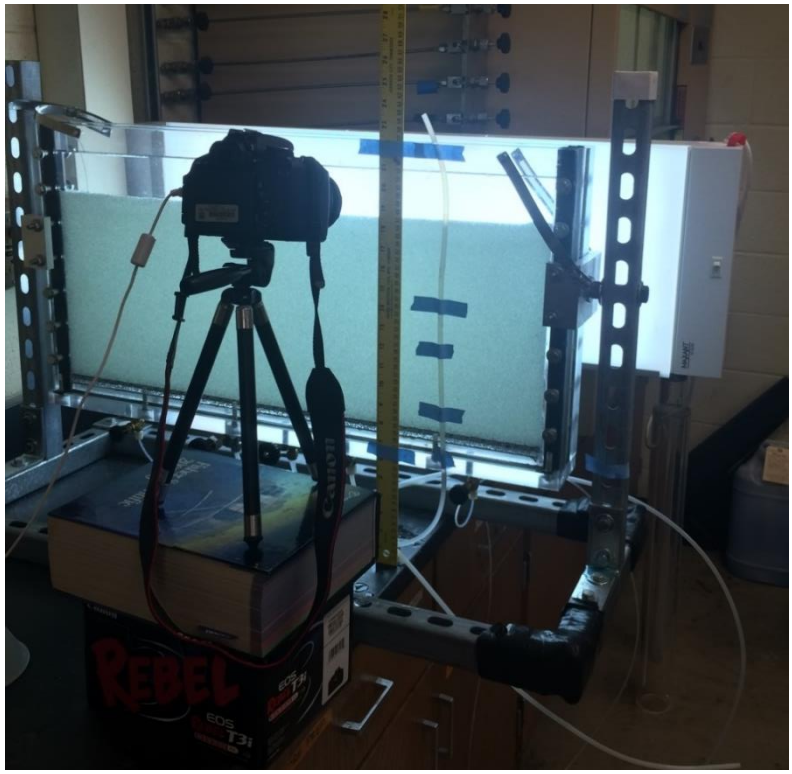

Figure 3.14 - Permeability measurement method for the convective dissolution experiment

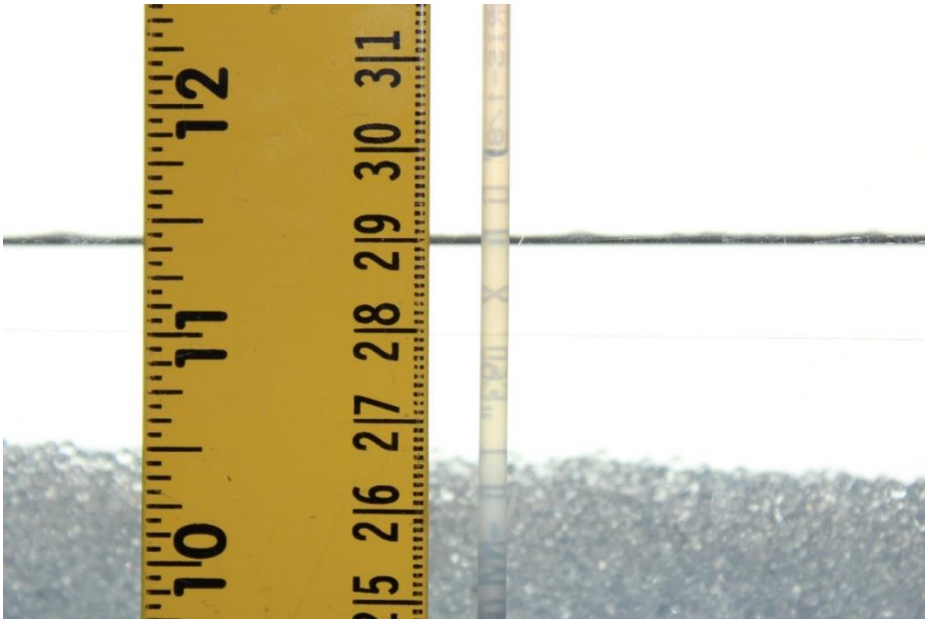

Figure 3.15 - An example of a good calibration image for permeability measurement

3.3.2.3.2 Permeability Measurement Results

As discussed above, by measuring relative water table difference the permeability can be obtained by Darcy's method. Take one measurement as an example, as shown in Figure 3.16, 2mm size beads are distributed in the experimental chamber. At that moment, it is a hydrostatic status because of closed valves. Therefore the water table in the experimental chamber equals to the water table in the central pipe. There is a slight water table difference between due to capillary pressure.

In order to perturb the hydrodynamic status, four symmetrical valves are opened and the fluid starts to flow through the porous media. Then the water table level in the central pipe starts dropping and going to be lower than water table level in the experimental chamber. The fluid flowing process and water table dropping process are as shown in Table 3.13. The time interval for each picture is 5 seconds. By measuring fluid flowing rate and water height difference, permeability of the 2mm beads porous media can be calculated as a consequence.

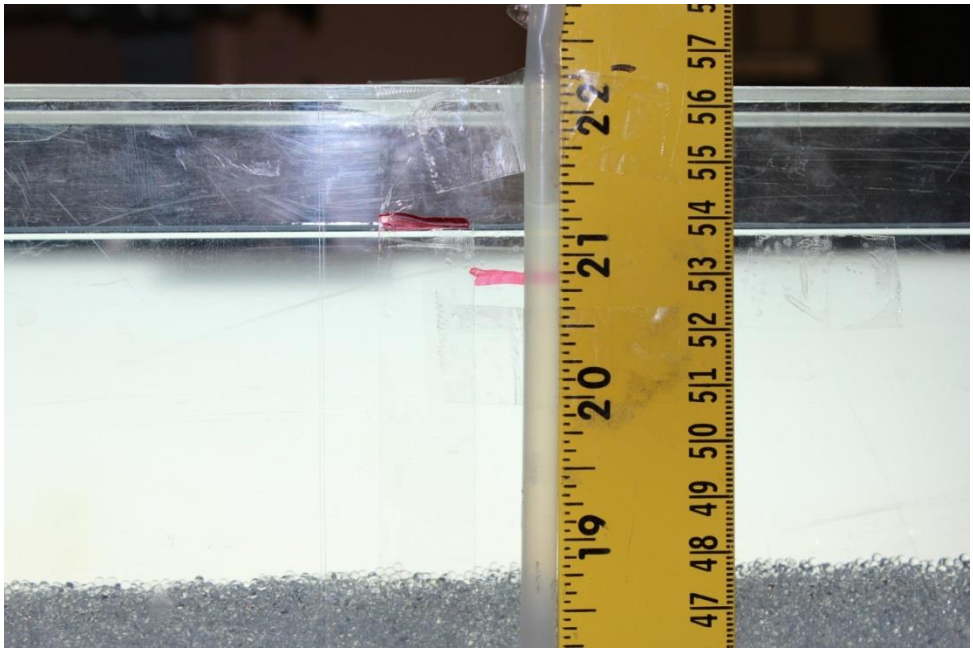

Figure 3.16 - Permeability measurements for 2mm glass beads

Table 3.13 - Permeability measurement procedure for 2mm beads

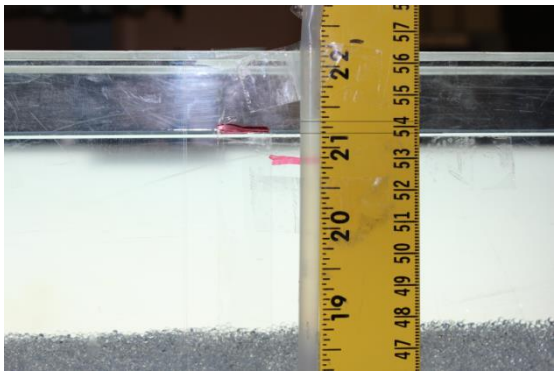		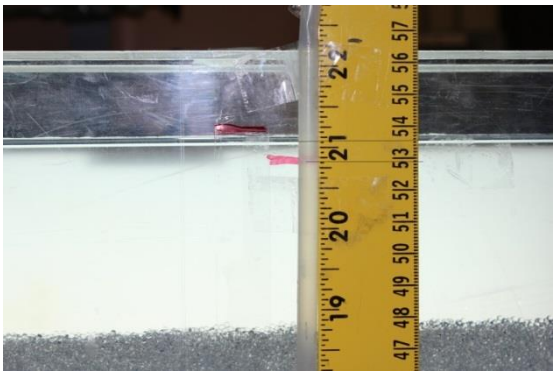	
Iamge 1 at 0 Sec $H' = H_{s1} - H_{s2} = 0.4\ cm$	H_{s1} = 53.80 cm H_{s2} = 54.20 cm	Iamge 1 at 5 Sec $\Delta H_1 = H_{c1} - H_{p1} + H' =$ $1.10\ cm$	H_{c1} = 53.60 cm H_{p1} = 52.90 cm

Table 3.13 – Continued

<table>
<tr><td colspan="2"> 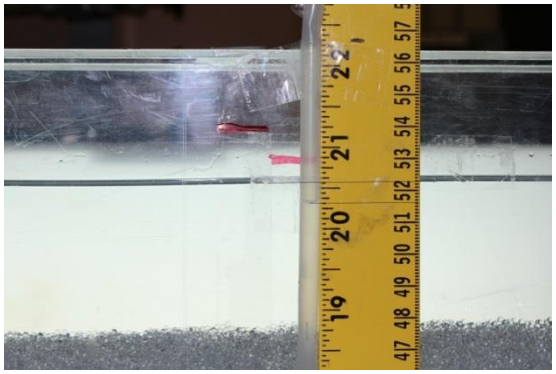 </td><td colspan="2"> 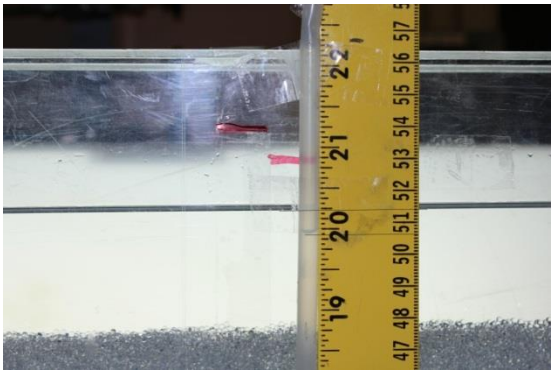 </td></tr>
<tr><td>Iamge 1 at 10 Sec
$\Delta H_2 = H_{c2} - H_{p2} + H' =$
$1.10\ cm$</td><td>H_{c2} = 52.30 cm
H_{p2} = 51.60 cm</td><td>Iamge 1 at 15 Sec
$\Delta H_3 = H_{c3} - H_{p3} + H' =$
$1.20\ cm$</td><td>H_{c3} = 51.40 cm
H_{p3} = 50.60 cm</td></tr>
<tr><td colspan="2"> 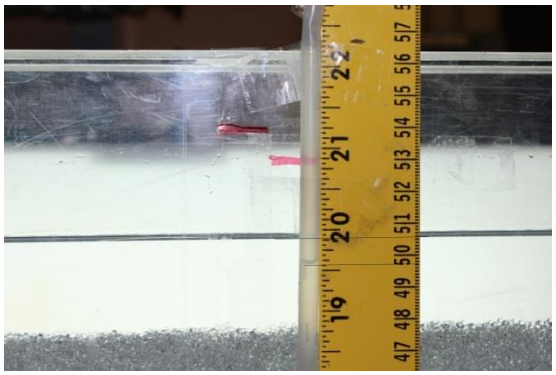 </td><td colspan="2"> 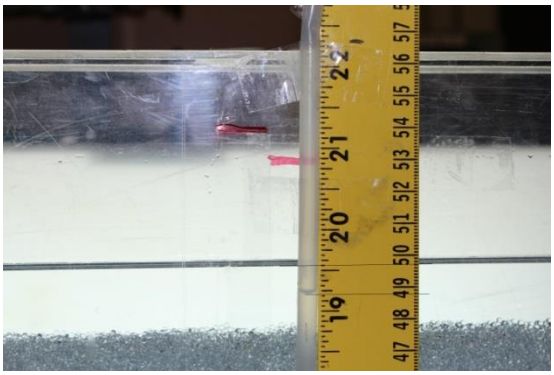 </td></tr>
<tr><td>Iamge 1 at 20 Sec
$\Delta H_4 = H_{c4} - H_{p4} + H' =$
$1.30\ cm$</td><td>H_{c4} = 50.60 cm
H_{p4} = 49.70 cm</td><td>Iamge 1 at 25 Sec
$\Delta H_5 = H_{c5} - H_{p5} + H' =$
$1.30\ cm$</td><td>H_{c5} = 49.70 cm
H_{p5} = 48.80 cm</td></tr>
<tr><td colspan="2">$V_1 = \frac{H_{c3} - H_{c2}}{5} = 0.18\ cm/s$
$V_2 = \frac{H_{c4} - H_{c3}}{5} = 0.16\ cm/s$
$V_3 = \frac{H_{c5} - H_{c4}}{5} = 0.18\ cm/S$</td><td colspan="2">$H_{ave} = \frac{1.1 + 1.2 + 1.3 + 1.3}{4} = 1.225\ cm$
$V_{ave} = \frac{0.18 + 0.16 + 0.18}{3} = 0.173\ cm/s$
$P = P_1 - P_2 = H_{ave} * \rho * g = 120.05\ pa$</td></tr>
</table>

For Darcy's equation, $k = V_{ave} * \mu * \frac{L}{P}$ where μ is the viscosity of water, and L is the length of measured core. For this 2mm porous media permeability measurement, $L = 28\ cm$ and $\mu = 0.9$ cp

Therefore, for permeability measured be Equation (5) as the Darcy's method,

$$K = V_{ave} * u * \frac{L}{P} = 0.173 * 0.9 * \frac{28}{0.0012005} = 3631um^2 = 3.6 * 10^{-9}m^2$$

For sphere packing porous media, permeability can also be calculated by Kozeny – Carman equation,

$$K = \frac{\phi^3 d^2}{(1 - \phi)^2 180} \quad (5)$$

Where ϕ is the porosity and d is the diameter of glass beads.

The results of Kozeny – Carman equation can be used as a reference to check the accuracy of measured permeability by the Darcy's method. For 2 mm beads porous media, by equation (5) the permeability $K = \frac{\phi^3 d^2}{(1-\phi)^2 180} = 5.19 * 10^{-9}\, m^2$. This result is close to measured results. The permeability measurements and calculation results is shown in Table 3.14.

Table 3.14 - Permeability for 1.2mm, 2mm and 3mm glass beads packing porous media

	K of 1.2mm (m^2)	K of 2 mm (m^2)	K of 3mm (m^2)
Darcy Measurement	$1.87* 10^{-9}$	$3.63* 10^{-9}$	$8.11* 10^{-9}$
Kozeny- Carman Equation	$1.86* 10^{-9}$	$5.15* 10^{-9}$	$1.16* 10^{-8}$

A water table difference exists between experimental chamber and central pipe in hydrostatic status. When two phase fluids are in contact with each, there is a pressure difference between two phase fluids, which is dependent on the curvature of the interface separating the two fluids. This pressure is known as capillary pressure. Therefore when measuring the permeability, the capillary pressure compensation is considered for accuracy of results.

The capillary pressure can by calculated by equation

$$P_c = \frac{2\sigma * cos\theta}{r} \quad (6)$$

Where σ the interfacial tension and r is the radius of the pipe.

As shown in the left picture in Table 3.15, there is a water table difference between the experimental chamber and the central pipe, and in the right picture it shows the contact angle approximately equals to 45°.

Table 3.15 - Capillary pressure effect and contact angle

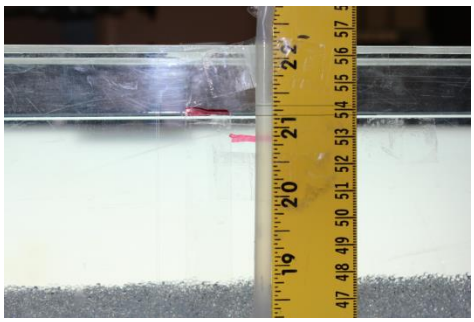	 

The surface tension between air and water is$7.2 * 10^{-3}\ N/M$, the radius of pipe is 0.25 cm, then

$$P_c = \frac{2\sigma * cos\theta}{r} = 2 * 7.2 * 10^{-2} * \frac{\cos 45}{0.0025} = 40.72Pa$$

The height difference is

$$h = \frac{P_c}{\rho g} = \frac{40.72}{1 * 10^3 * 9.8} = 0.0041\ m = 0.41\ cm$$

According to the left picture above, the measured height difference is 0.4 cm, which is close enough to the calculation result. Therefore, when calculating permeability, a height difference 0.41 cm is used as the capillary pressure compensation.

3.3.3 VIDEO CAPTURE SET-UP

In order to record the convective dissolution process as a function of time, the video capture system is set up, including a large light box, a camera in front of the experimental chamber, and a computer for remote controlling. The camera is connected to that data acquisition computer, which could take and store pictures of dissolution

experiments automatically. The distance between light box and experimental chamber is fixed while the distance between camera and experiment chamber depends on which measurement is taking place. If permeability is measured, the distance should be 10 cm. If porosity or dissolution is measured, then this distance should be 70 cm. The camera used is a Canon EOS REBEL T3i. Because the image processing method is very sensitive to captured light which is transmitting through the porous media during the experiments, the camera setting is fixed to obtain a series of consistent images for all experiments, as shown in Table 3.16. Figure 3.17 shows Canon EOS REBEL T3i and its related function bottoms.

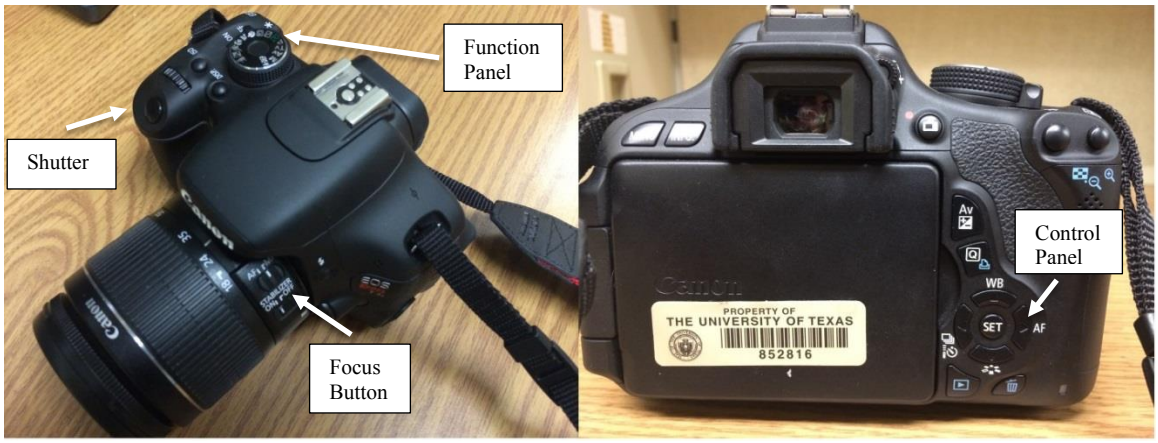

Figure 3.17 - Canon EOS REBEL T3i

Table 3.16 - Fixed camera image capturing settings for consistent image capture

Camera Maker	Camera Maker	F- Stop	Exposure Time	ISO Speed
Canon	EOS REBEL T3i	F/10	1/30 Sec	ISO - 100

If needed, a light diffuser is used between light box and experimental chamber to create a light- uniform environment. Figure 3.18 shows the relative position between the experiment chamber and video capture system.

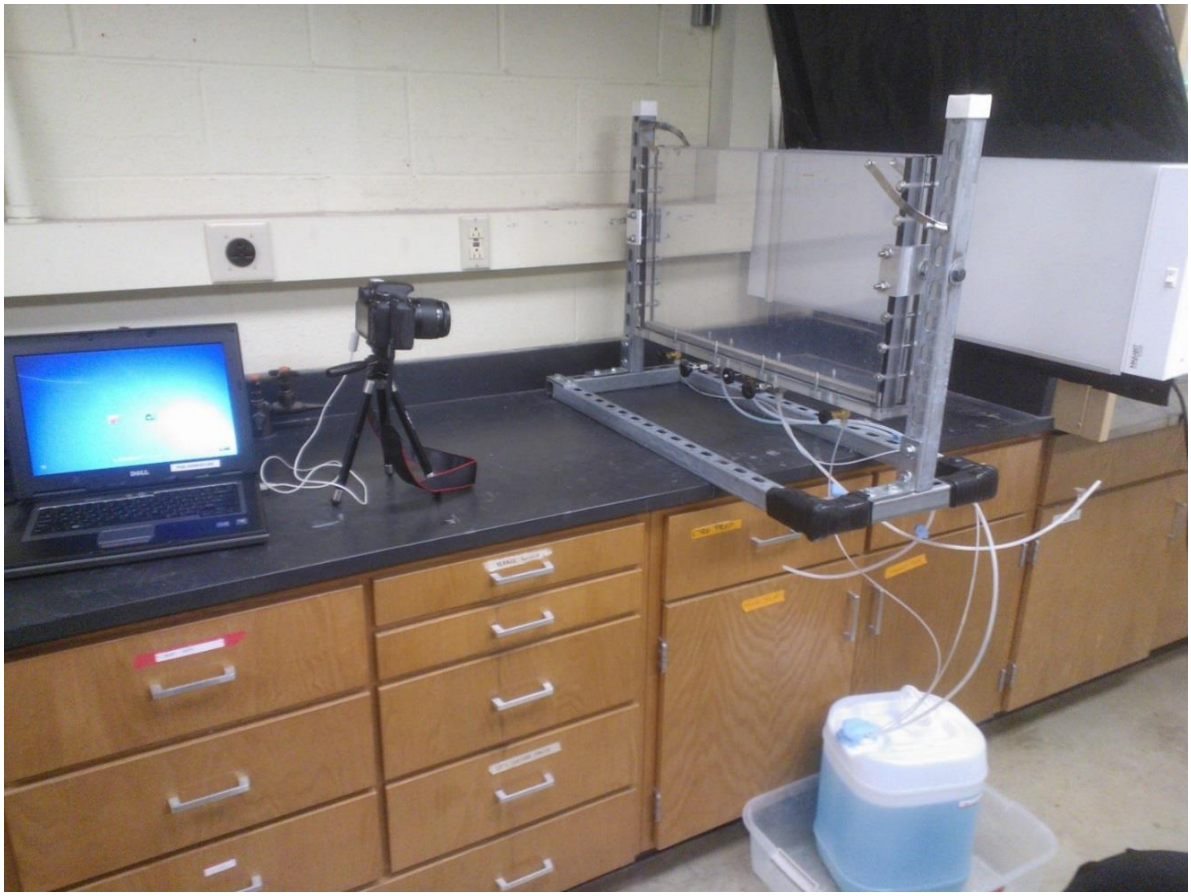

Figure 3.18 - Relative position of the experiment set-up for convective dissolution experiments

3.4 VIDEO CALIBRATION

In order to analyze the images captured from the dissolution experiments, it is necessary to observe and record the interface between MEG and water clearly and accurately. Since both of MEG and water are colorless and transparent, a dye with an appropriate concentration is required to color the MEG component. Then the receding interface, MEG concentration and finger dynamics can be determined by the color saturation difference between dyed MEG and water. Figure 3.19 - Effect plot of dyed MEG dissolving into watershows the effect of MEG with dye dissolves into water in porous media.

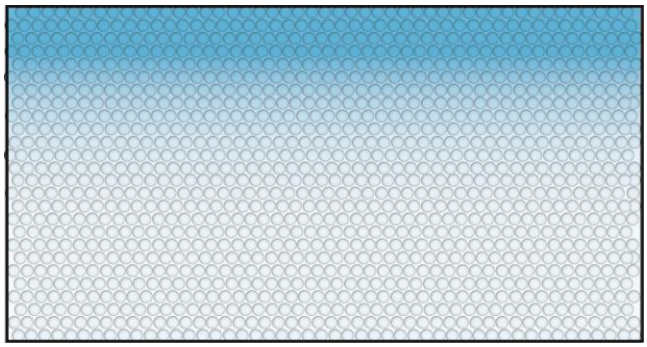

Figure 3.19 - Effect plot of dyed MEG dissolving into water

3.4.1 BRILLIANT BLUE FCF

From visualization perspective, both of MEG and water are transparent. As a result, MEG is dyed in order to be distinguished from Water. Brilliant Blue FCF, with molecular formula $C_{37}H_{34}N_2Na_2O_9S_3$, is used as the dye for the MEG, as shown in Figure 3.20 - Molecule of Brilliant Blue FCF.

The assumption is that, when dissolving into MEG, Brilliant Blue FCF only tracks the during the flow. Therefore, the color saturation difference between MEG and water, which is caused by the dye inside MEG, is a good indictor to distinguish MEG and water.

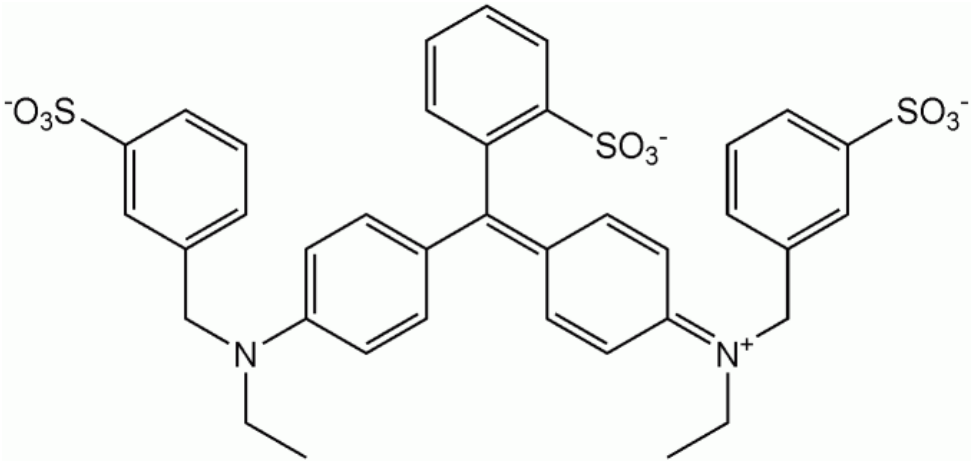

Figure 3.20 - Molecule of Brilliant Blue FCF

Therefore, when dyed MEG dissolves into water and forms MEG-water mixture, the dye concentration deceases as water fraction increases, resulting in color saturation decreasing. Figure 3.21 shows the relationship between color saturation and dye concentration in MEG-water mixture. It should be noted the calibration work is still in progress and doesn't finish yet, so that dependence is not scaled.

The MEG fraction in MEG-water mixture has a linear relationship with dye concentration, which can be represented as the black box on Figure 3.21. If the dye concentration into MEG-water mixture is appropriate, for a specific type MEG, the relationship between color saturation and MEG fraction into MEG-water mixture falls

into zone 1. If more dye is added, dye concentration will increase and the relationship between color saturation and MEG fraction into MEG-water mixture will move to zone 2. Compared to zone 2, with the MEG fraction from 0 to 100%, the color saturation variance range is larger. In other word, in zone2, with a small color saturation change, the MEG concentration has changed a lot, which is difficult for image process therefore undesired. Therefore, it is necessary to determine an appropriate dye concentration and use it consistently for all experiments. Through my experiment, 0.01g/700g dye is used for interface calculation and 0.03g/700g dye concentration is used for finger dynamic analysis.

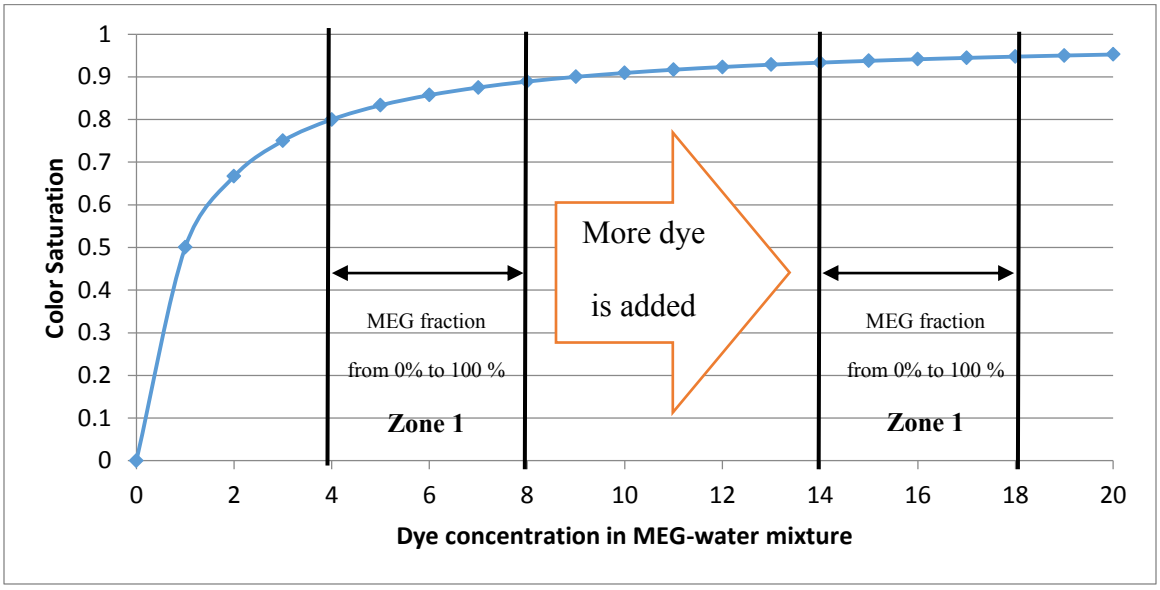

Figure 3.21 - Color saturation vs Dye concentration (Not scaled)

3.4.2 RGB CONVERTED TO HSV

In MATLAB, all images are saved as RGB (Red, Green and Blue) format. A broad array of colors is reproduced by added three colors together in various ways. A HSV format represents Hue, Saturation, and Value. Especially the saturation is actually the brightness of color captured, which is the color saturation concept we discussed above. Therefore captured experimental image should be switched to be presented only by color saturation to show the MEG concentration.

When dyed MEG dissolves into brine, we assume no diffusion would happen between dye molecular and brine. Therefore, by measuring the color saturations, receding velocity, finger dynamic and MEG concentration can be determined according to the relationship between color saturation and dye concentration. When the camera captures the experiment all process, all images are saved as RGB format (Red, Green and Blue). By switching the format of images from RGB to HSV (Hue, Saturation and Value) and only present the image by its color saturation, since we know the dependence between color saturation and dye concentration and the relationship between dye concentration and MEG fraction in MEG-water mixture, then MEG concentration can be determined by color saturation value. This is the basic idea to process the experimental images.

3.4.3 DYE CONCENTRATION CALIBRATION FOR COLOR SATURATION

In order to calibrate color saturation and dye concentration into MEG-water mixture, water solutions with different dye concentrations are distributed into porous media homogeneously and processed by MATLAB to show its color saturation.

The dye concentrations tested for calibration are 0.0005%, 0.0010% , 0.0015% , 0.0020% , 0.0025% , 0.0030% , 0.0035%, 0.0040% , 0.0045% , 0.0050% , 0.0055% by weight. With fixed relative positions between light source, experimental chamber and camera, a series of experimental pictures is taken as shown in left column in Table 3.17. Then the image is processed by MATLAB, the processed images are shown in Right column in Table 3.17.

Calibration results can be applied a reference to determine MEG concentration in convective dissolution experiments, especially to analyze the dynamics around MEG convective fingers areas as, where MEG concentration has a large variance.

Table 3.17 - Dye concentration calibration for color saturation

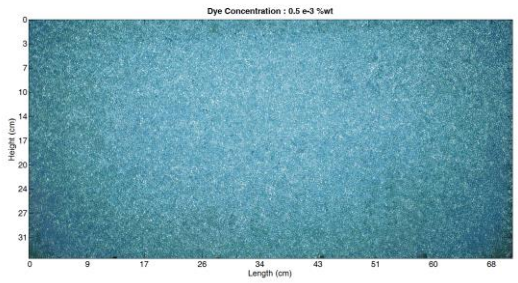	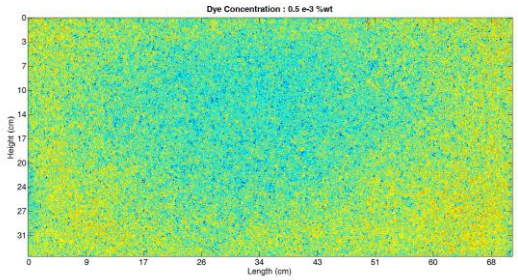
Image 1 : Original image with 0.0005% dye	Image 2 : processed image with 0.0005% dye
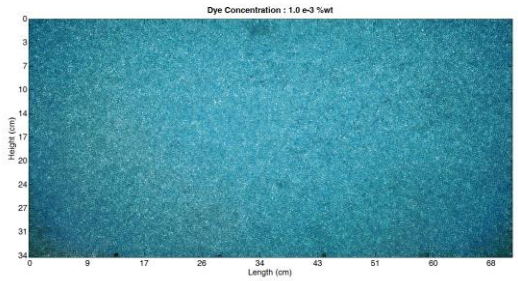	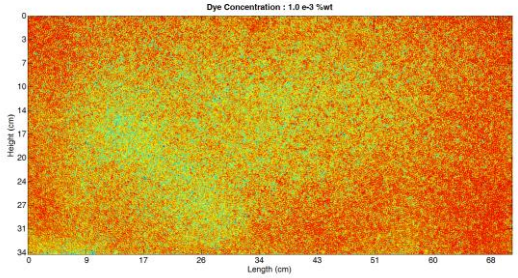
Image 3 : Original image with 0.0010% dye	Image 4 : processed image with 0.0010% dye

Table 3.17 –Continued

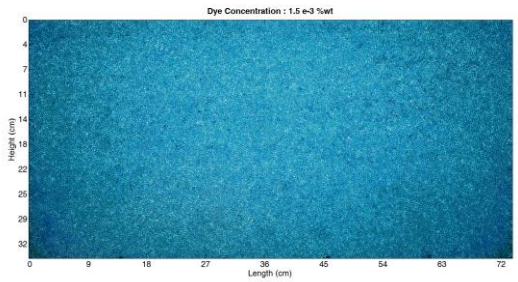	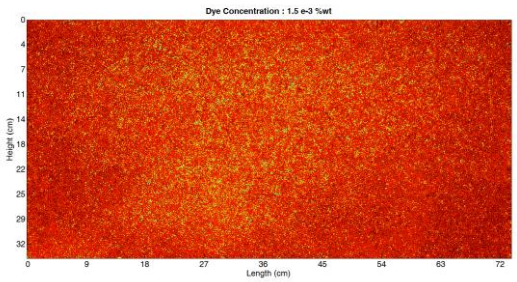
Image 5 : Original image with 0.0015% dye	Image 6 : processed image with 0.0015% dye
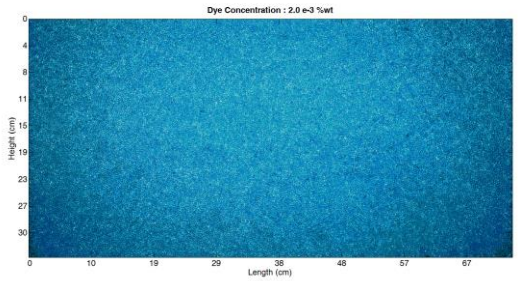	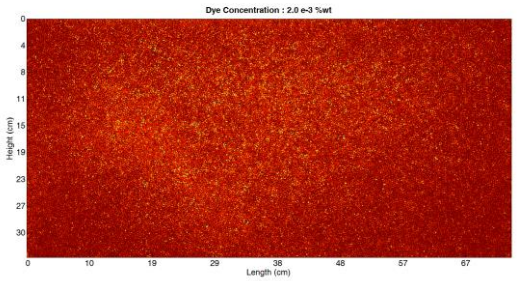
Image 7 : Original image with 0.0020% dye	Image 8 : processed image with 0.0020% dye
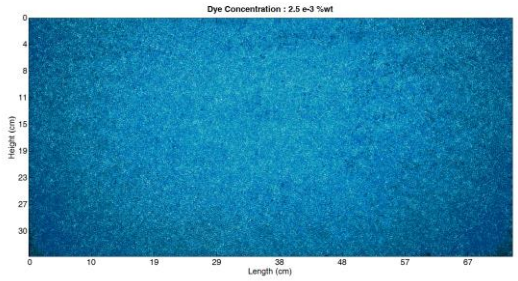	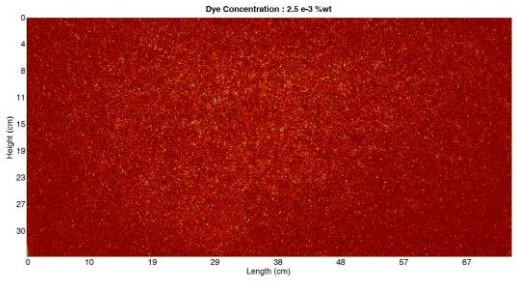
Image 9 : Original image with 0.0025% dye	Image 10 : processed image with 0.0025% dye

Table 3.17 –Continued

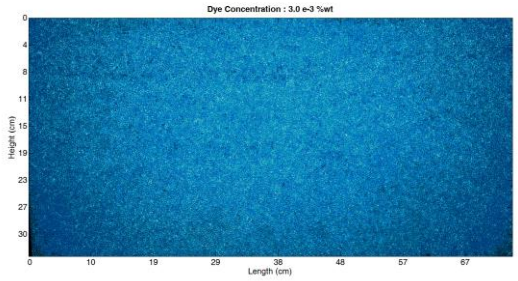	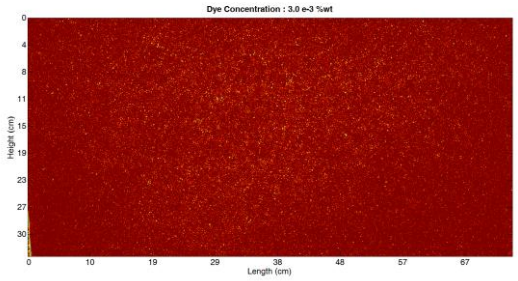
Image 11 : Original image with 0.0030% dye	Image 12 : processed image with 0.0030% dye
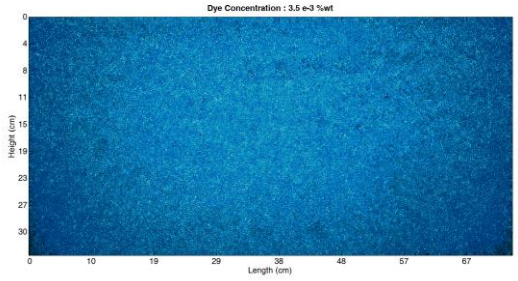	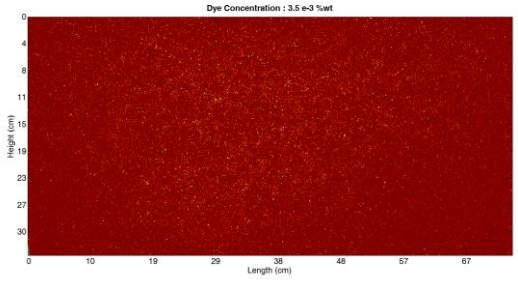
Image 13 : Original image with 0.0035% dye	Image 14 : processed image with 0.0035% dye
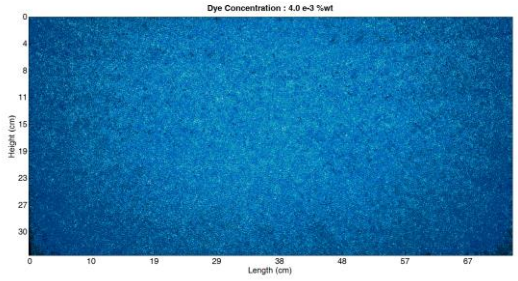	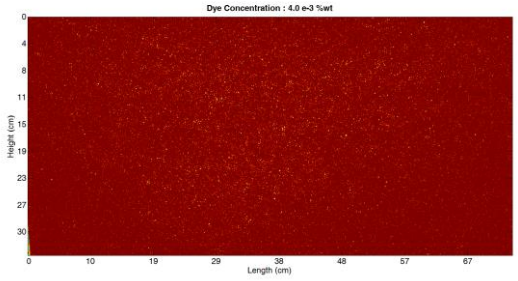
Image 15 : Original image with 0.0040% dye	Image 16 : processed image with 0.0040% dye

Table 3.17 –Continued

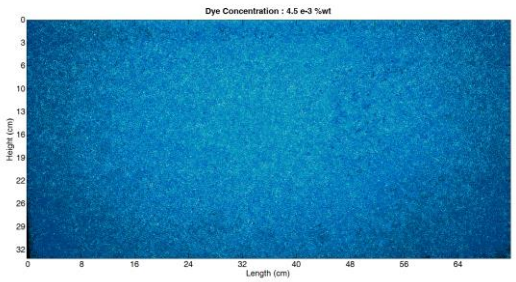	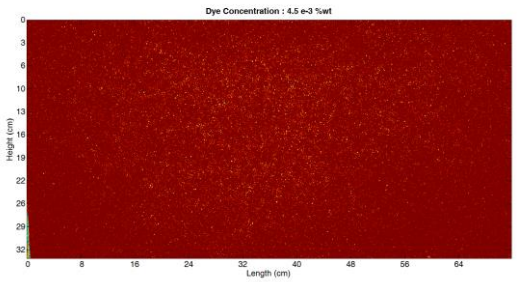
Image 17 : Original image with 0.0045% dye	Image 18 : processed image with 0.0045% dye
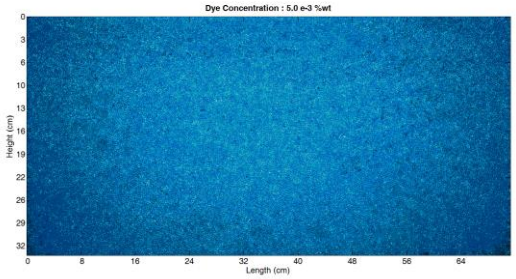	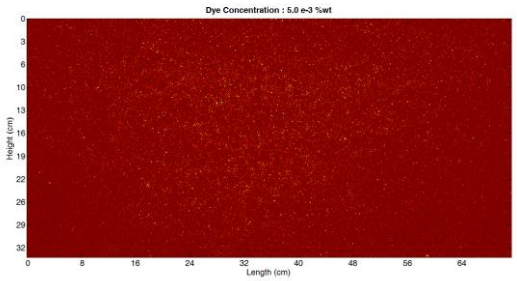
Image 19 : Original image with 0.0050% dye	Image 20 : processed image with 0.0050% dye
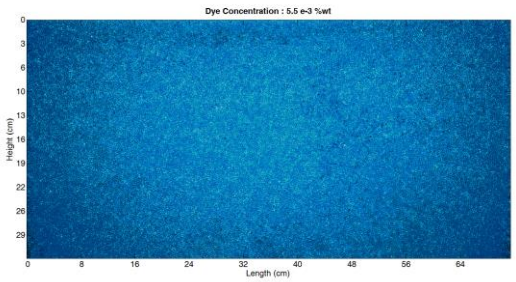	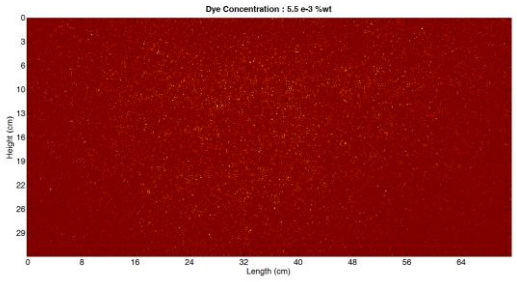
Image 21 : Original image with 0.0055% dye	Image 22 : processed image with 0.0055% dye

3.4.4 DYED MEG PREPARATION

In order to have consistent results, a large amount of four types of MEG with a certain dye concentration are prepared and stored in a closed container in advance. When a new experiment is planned, the prepared MEG can then be used consistently to avoid errors. Four type of MEG are used including 40:60, 37:63, 35: 65, and 33: 67 (Weight ratio of methanol to ethylene- glycol). A 4L container with lid is used to store each type of MEG. However, the upper limit for the scale is 1000 g, which is 1L approximately. Therefore, for a specific type of MEG, methanol and ethylene should be mixed four times to fill up the container. After MEG is made and stored, dye is also added according to the requirements. Lids should be closed tightly and label with MEG information on the container. Table 3.18 shows required materials' weight of methanol and ethylene- glycol required for a 4L MEG preparation. A stirring bar is placed into the container for 20 minutes mixing on stirring plate to obtain a highly homogeneous MEG. Figure 3.22 shows the prepared MEGs in the container.

Table 3.18 - Required methanol and ethylene - glycol weights to make pure MEG

MEG type	40:60		37:63	
Measurement #	Methanol g	Ethylene- Glycol g	Methanol g	Ethylene- Glycol g
1	360	540	333	567
2	360	540	333	567
3	360	540	333	567
4	360	540	333	567
MEG type	35:65		33:67	
Measurement #	Methanol g	Ethylene- Glycol g	Methanol g	Ethylene- Glycol g
1	315	585	297	603
2	315	585	297	603
3	315	585	297	603
4	315	585	297	603

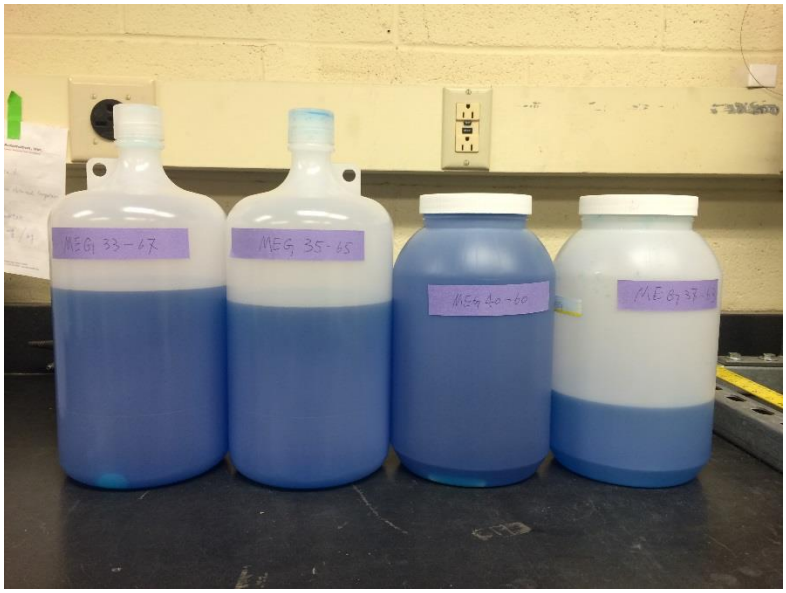

Figure 3.22 - Four types of MEG with a certain dye concentration ready for experiment

3.5 DISSOLUTION EXPERIMENT

To begin the dissolution experiment, an experimental plan should be made in advance. As we can expect, the CO2 convective dissolution dynamics depends on the permeability of the porous media and the maximum density difference. The permeability for glass beads packing porous media is determined by bead size and the maximum density difference is determined by MEG type. Therefore the experimental plan should contain beads size, MEG type information experimental date and dye concentration as a record. A successful dissolution experiments includes MEG preparation, porosity measurement and permeability measurement, dissolution measurement and image processing, but it should be noted that in some cases a combination of experiments can have better efficiency. For example, permeability measurement for a specific size of beads can be measured isolated, but the dissolution experiment can also be conducted after permeability measurement. That is the reason why a detailed plan is necessary for successful experiments. Figure 3.23 shows the schematic of CO2 dissolution experiment and the arrows in Figure 3.1 represents the potential combinations of experiments for efficiency maximization.

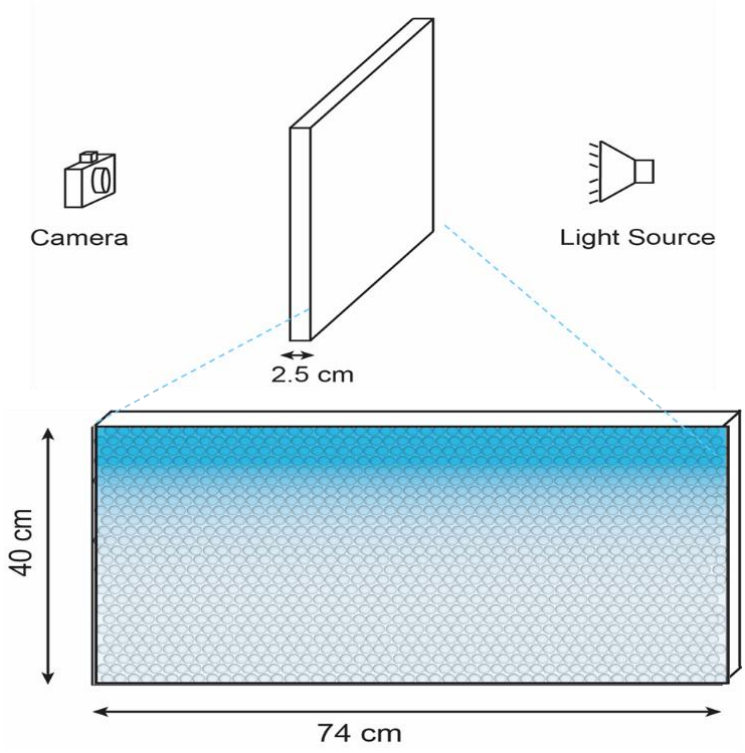

Figure 3.23 - Schematic of CO2 dissolution experiment

3.5.1 CONVECTIVE DISSOLUTION MEASUREMENT PROCEDURE

The procedure to measure dissolution dynamics is listed below

1. Determine MEG type and beads size for the experiment according to the experimental plan.
2. Close all valves under the experimental chamber.
3. Turn on the light box.
4. Put down black sheets to create a light- uniform experimental environment.
5. Pour 1 litter volume DI water into chamber.

6. Distribute a certain size of glass beads into experimental chamber by funnel evenly and stably until beads level almost reaches water interface level.
7. Repeat step 2 and step 3 until beads level reaches required level. Refer to porosity measurement procedure if porosity is required to be measured. Refer to permeability measurement procedure if permeability is required to be measured.
8. Fill both of DI water and glass beads into the level 48 cm away from table.
9. Fill glass beads to the level 53 cm away from table.
10. Close all valves tightly in case of drainage. Check them again before next step.
11. Use waterproof tape to stick ruler vertically on the surface of chamber. Recommend position of ruler is 3 cm away from left side of chamber.
12. Plug the battery into camera, attach camera to tripod and connect camera to computer. Then turn on the camera and computer. The passcode for computer is ‘’CompData!’’.
13. Place the camera 70 cm away from the chamber. Make sure the camera can work and stand stably on the table.
14. Click EOS utility icon in Windows, then select remote control.
15. Estimate whether computer has enough space for dissolution experiment image capture by checking how many pictures can be took based on current space. Usually available room for 1000 pictures is recommended.
16. Switch focus function into “AF” and build in flash.

17. Adjust camera setting.
18. Install fluid distributor above experimental chamber. Make sure the hole on the distributor is facing upward and slit on the on the distributor is facing down to glass beads in the experimental chamber.
19. Rotate the handle to make the slit on inner core inside the distributor face to the hole on the distributor.
20. Use funnel to inject MEG from the hole into inner core.
21. Take the first picture manually for calibration purpose. A folder would be created automatically and named as current date. Make sure whole experimental chamber can be captured clearly. Repeat step 20 until calibration picture meets the requirement. A good calibration should be like Figure 3.24.
22. Click timer function in EOS utility. Set delay time as 10 seconds, picture interval as 10, 15, 30 or 60 seconds, according to plan requirement.
23. Switch focus function into "MF" and shut down flash.
24. Click start button to let camera take pictures automatically.
25. After first picture, rotate the handle to make the slit on inner core face to the slit on the distributor stably and gradually. Make sure there is no relatively movement of experimental chamber during rotation process.
26. Check whether MEG and water interface is evenly distributed from following picture captured.
27. Dissolution process happens in the experiments chamber.

28. when all MEG dissolves into water and no finger exists in the chamber, stop the camera by click ‘’stop’’ in EOS utility.
29. Detach the ruler from the surface of chamber.
30. Detach the fluid disturber from the chamber.
31. Open valves to drain the water and MEG, dump the beads, and clean experiment environment. Turn off the light box.
32. After the measurement, captured images are processed to calculate dissolution dynamics. It is important to recharge the battery immediately for next experiment. It should also be noted that the camera should be placed in a safe place, the office desk in CPE 1.106 is recommended.

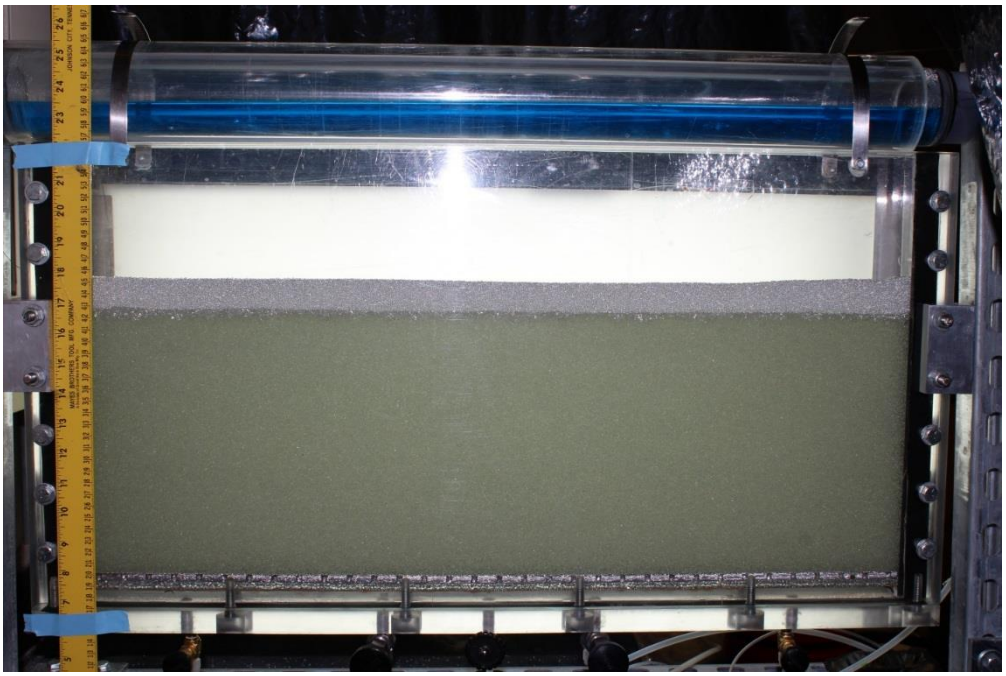

Figure 3.24 - An example of a good calibration picture for convective dissolution experiment

3.5.2 IMAGE PROCESSING METHOD

After all experimental images are captured by video capture system, images are processed by MATLAB. The general idea is to use the calibration picture to find appropriate size for the whole experimental images by truncate function. By allocating a real dimension by attached ruler to the pixels that images storage take, the actual distance between any two points on the plot can be calculated. By switching the image from RGB format to HSV format, MEG concentration can be determined, than the receding interface rate, fingers dynamics and fluid dynamics can be calculated as a result. Figure 3.25 shows the logic plot of the image processing method and Figure 3.26 shows the effect plot of one processed experimental image. As we can observe from Figure 3.26, experimental part is truncated to target part, and MEG concentration in flowing fingers can be represented as the color saturation. Also experimental time is added on the title so experimental process can be played as a function of time.

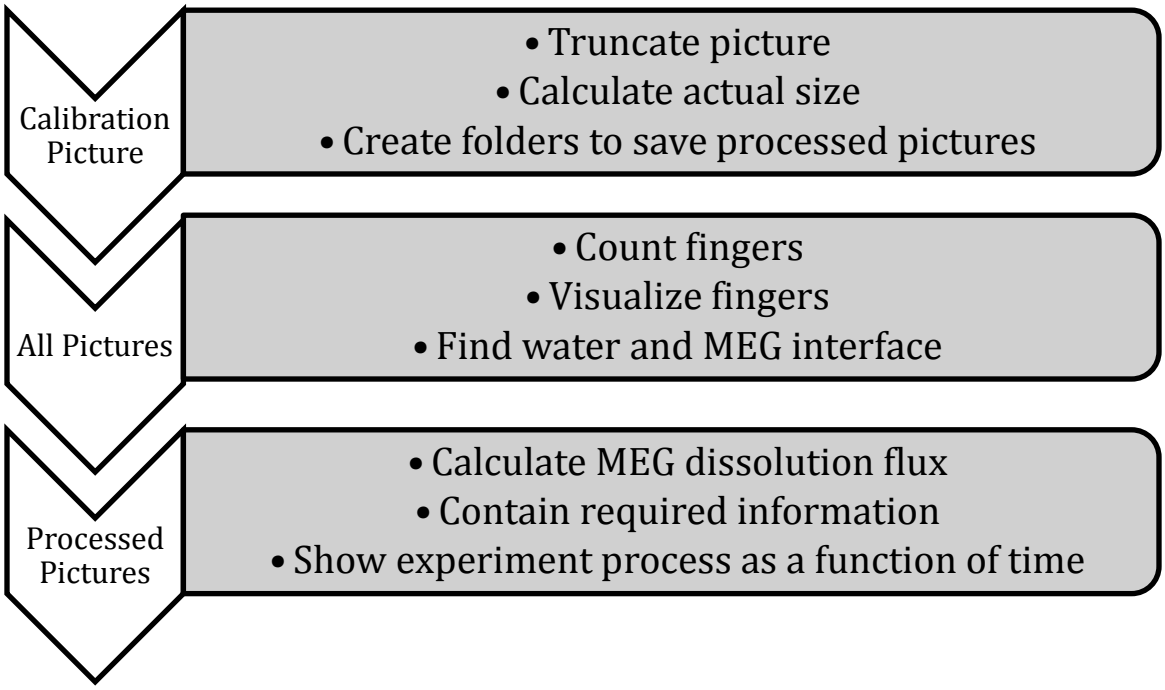

Figure 3.25 - Logic plot of the image processing method

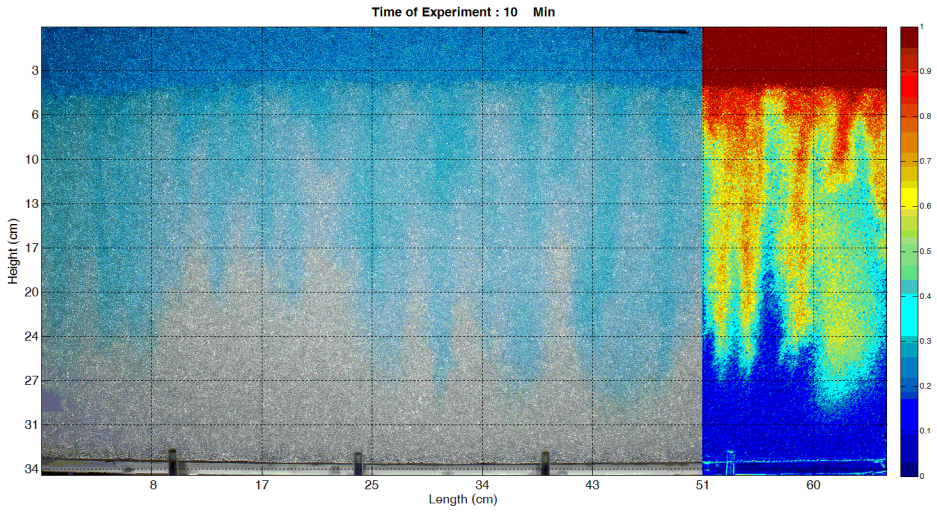

Figure 3.26 - Effect plot of one processed experimental image

In MATLAB, the corresponding script to create the direction and folders is listed below

```
[filename, pathname] = uigetfile('*.jpg',
'Pick the lights on file');
totalname = [pathname filename];
filedata = str2num(filename(12:15));
filedata = num2str(filedata);
mkdir(pathname,'processed');
mkdir(pathname,'original');
mkdir(pathname,'data');
pr = 'processed\';
or = 'original\';
dt = 'data\';
```

```
% Choose the first
experimental image

% Obtain the pathname
and folder direction of
selected image

% Make three folders to
save the following
processed iamges
```

The corresponding script to determine the actual size

```
clear x_r y_r
reply = 'No';
while strcmp(reply,'No')
    hold off; imagesc(im_in,[0,1])
    h = questdlg('Choose 30 cm (left click)
and 40 cm points (right click) from ruler 1
using mouse','Point
Selection','OK','OK','OK');
    [x_r(:,1),y_r(:,1),P] = impixel;
    hold on; plot(x_r(:,1),y_r(:,1),'xg-')
    reply = questdlg('Point Check','Points
Good?','Yes','No','No');
end
sc = abs(y_r(1,1) - y_r(2,1));
r = 30/sc;
```

```
% pick two points on
the ruler with a actual
distance of 30 cm in
the calibration image

% calculate the real
size, sc is the pixel
between 10 cm to 40 cm.
r is the factor with a
unit cm/pixel
```

The corresponding script to allocate the actual size to the x axis and y axis

```
a = abs (y_r_l(1,1) - y_r_l(2,1));
b = abs (x_r_l(1,1) - x_r_l(2,1));
%r=0.01;
r = r*1000;
r = ceil(r);
r = r/1000;
set(gca, 'Xlim', [-0.0000000000000001, b]);
```

```
% Obtain the size of
graphic current x axis
and y axis
```

```
set(gca, 'Ylim', [-0.0000000000000001, a]);
original = gca;
position = get(original, 'Position');
xtick = get(original,'XTick');
ytick = get(original,'YTick');
xsize = size(xtick);
ysize = size(ytick);
xtick_t = zeros(xsize);
ytick_t = zeros(ysize);
xtick_t_new = zeros(xsize(1,2),xsize(1,1));
ytick_t_new = zeros(ysize(1,2),ysize(1,1));
xtick_t = xtick * r;                          % Switch pixel to
xtick_t = round(xtick_t);                     actual size in cm by
xtick_t_new(:,1) = xtick_t(1,:);              multiply the factor r
ytick_t = ytick * r;
ytick_t = round(ytick_t);
ytick_t_new(:,1) = ytick_t(1,:);
xticklabel = num2str(xtick_t_new);            % Rewrite the labels in
yticklabel = num2str(ytick_t_new);            the x axis and  the y
set(original, 'XTick', xtick, 'XTickLabel',   axis
xticklabel,'FontSize',18);
set(original, 'YTick', ytick, 'YTickLabel',
yticklabel);
xlabel('Length (cm)');
ylabel('Height (cm)');
grid on;
tt = 0;
title(['Time of Experiment : ',num2str(tt),'
Min'],'FontWeight','bold');                   % Add the time to each
                                              image
```

The corresponding script for looping control

```
[filename, pathname] = uigetfile([pathname    % Select the last
'*.jpg'], 'Pick the LAST image');             picture
totalname_new = [pathname filename];
filenum_i = str2num(filename(12:15)); %loop   Obtain the filename
start                                         and direction of that
jj=0;                                         last image
exist_var = 2;

while exist_var>0                             % if exist is larger
    totalname = totalname_new;                than zero, the looping
    filename                                  starts
    im_i = imread(totalname);
    im_i_new =


Image process functions                       % if exist is larger
                                              than zero, the looping
                                              starts
```

```
    output = [pathout,filename];
    filedata_new = str2num(filename(12:15));
    filedata_new = num2str(filedata_new);
    output_data = [pathout_data,filedata_new];
    set(gcf,'PaperPositionMode','auto');
    saveas(gcf,output,'jpg');  %%%

    filenum = str2num(filename(12:15));
    if (filenum<11)
        filestring = ['000' num2str(filenum-
1)];
    elseif (filenum<101)
        filestring = ['00' num2str(filenum-1)];
    elseif (filenum<1001)
        filestring = ['0' num2str(filenum-1)];
    else
        filestring = num2str(filenum-1); %
    end
    filename = [filename(1:11) filestring
filename(16:end)];
    totalname_new = [pathname filename];

    jj = jj+1;
    exist_var = exist(totalname_new);
end
```

```
% save those images to
the directed folders

% fine one image
before the processed
image by ducting 1
from the series number
of processed image

%  Filename of new
image, which is one
smaller than processed
Image
If that exists,
exist_var is larger
than zero. If not
exists, exist_var
becomes zero, and
looping ends
```

CHAPTER 4: RESULTS

4.1 AN EXAMPLE OF CONVECTIVE DISSOLUTION MEASUREMENT AND ANALYSIS

4.1.1 EXPERIMENTAL IMAGES CAPTURING

Following the convective dissolution experiment procedure, analog fluid system of MEG and water is distributed into porous media and then convective dissolution experiment can be triggered with camera capturing the whole experimental process. Take one experiment as an example, 3 mm size beads are used to create a homogeneous porous media, and 37- 63 MEG with a dye concentration of 0.01g/700g is used as the analog fluid. Before the experiment, porosity and permeability of the porous media are measured and then calculated according to the experimental plan. Table 4.1 shows the original experiment images for the 37 -63 MEG in 3mm size beads convective dissolution experiment. The first image of the experiment is took with the camera flash on as the calibration image, which is used to determine the target area of all experimental images and to allocate the actual size to the all experimental images.

Table 4.1 - Original images for the 37 -63 MEG in 3mm size beads porous media

	
Calibration Image 1 at 0 Sec	Experimental Image 2 at 10 Sec
	
Experimental Image 3 at 400 Sec	Experimental Image 4 at 800 Sec
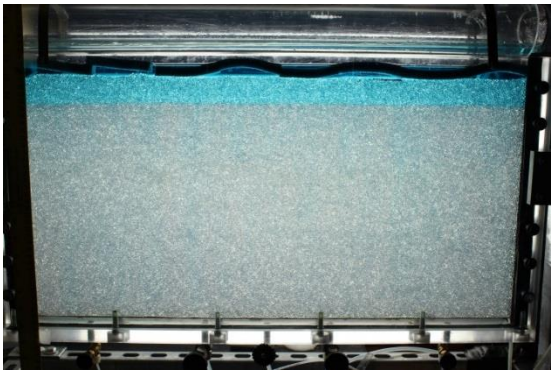	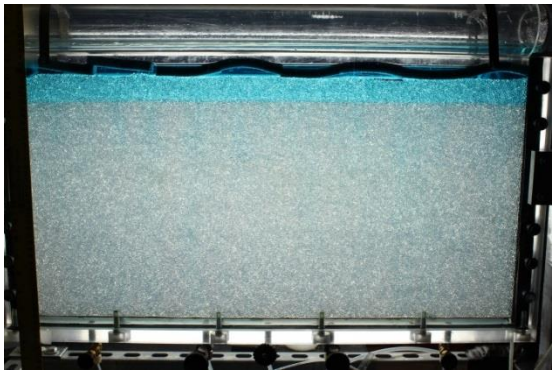
Experimental Image 5 at 1200 Sec	Experimental Image 6 at 1600 Sec

Table 4.1 – Continued

	
Experimental Image 7 at 2000 Sec	Experimental Image 8 at 2400 Sec
	
Experimental Image 9 at 2800 Sec	Experimental Image 10 at 3200 Sec
	
Experimental Image 11 at 3600 Sec	Experimental Image 12 at 4000 Sec

Table 4.1 – Continued

	
Experimental Image 13 at 4400 Sec	Experimental Image 14 at 4800 Sec
	
Experimental Image 15 at 5200 Sec	Experimental Image 16 at 5600 Sec

4.1.2 EXPERIMENTAL IMAGE PROCESSING

Currently we are interested in analyzing the images to determine two parts. 1) Dissolution rate and controlling factors and 2) dissolution finger pattern and its controlling factors. Therefore the captured original experimental images are processed by MATLAB to calculate dissolution rate, as well as to analyze the dissolution finger pattern.

First of all, experimental images are switched from HSV format to RGB format, and are only presented by the color saturation. This is known as the 1st processing stage. During this stage, the calibration image, which is captured when the camera flashing on, is processed to 1) allocate actual dimensions to all experimental images instead of pixels and 2) cut off undesired parts of all experimental images. All experimental images are saved as matrices, and each value in the matrix represent the color saturation at that specific position. Therefore, actual dimension is allocated by artificially defining an actual size to the distance between two elements in the matrix (calculated as pixels), and the region outside of the chamber is cropped off to reduce the size the matrix.

For example, if an image is saved as a 3*3 matrix, $A = \begin{matrix} a_{11} & a_{12} & a_{13} \\ a_{21} & a_{22} & a_{23} \\ a_{31} & a_{32} & a_{33} \end{matrix}$, the element a_{11} , with a numerical range from 0 to 1, is the color saturation at the upper right corner of the image. If we define a 1 cm to 1 pixel, the distance between a_{11} and a_{21}, then we can know that the actual size between a_{11} and a_{31} is 2 cm. Also, it we don't want left part of the image, just eliminate 1st column and reduce the matrix to a 3*2 matrix and get new matrix $B = \begin{matrix} a_{12} & a_{13} \\ a_{22} & a_{23} \\ a_{32} & a_{33} \end{matrix}$.

Back to the convective dissolution experiment, the size of an experiment image is usually 3000*5000. By the method discussed above the actual dimensions are added to the calibration image by reading the distance on the ruler and the outside region is cropped off. Because the relative position between camera and experimental chamber is

fixed, so calibration image and following experimental images have same size matrix but different element numbers in the matrix, color saturation in other words. Therefore, by the 'while' sentence in the MATLAB, all images are truncated and switched to HSV format according to the information obtained from calibration image. Besides, all experimental images can be added an axis with actual dimonsions. The time interval for each experimental image captured is fixed, so the time information is added in the title of each image. Table 4.2 shows the experimental images after the 1st processing stage.

In MATLAB, the corresponding script to conduct 1st stage processing is listed below

```
hsv_i = rgb2hsv(im_i_new);
hsv_filter_i = hsv_i(:,:,2);
```

```
% Switch original image
to HSV format
% Image is present only
by the color saturation
```

Table 4.2 - Image after 1st processing stage

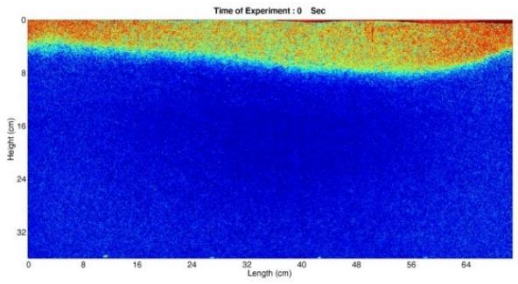	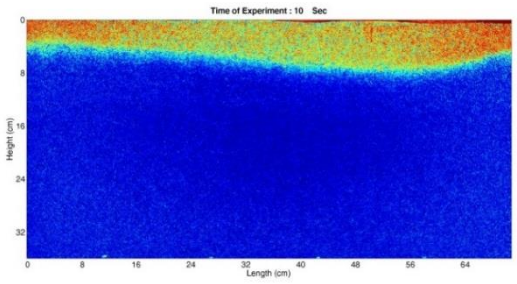
Calibration Image 1 at 0 Sec	1st Processed Image 2 at 10 Sec

Table 4.2 – Continued

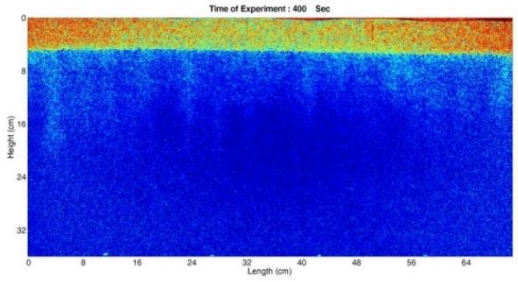	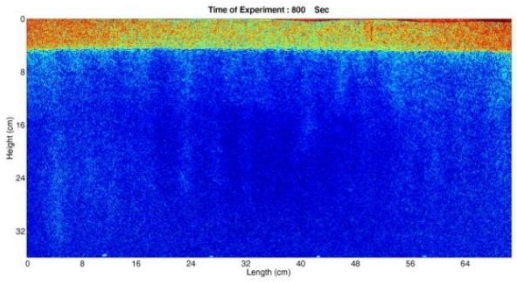
1st Processed Image 3 at 400 Sec	1st Processed Image 4 at 800 Sec
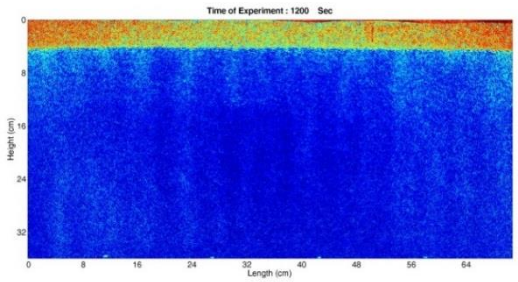	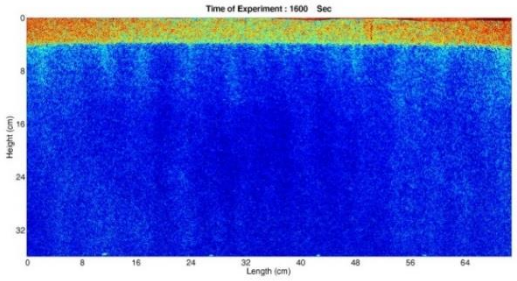
1st Processed Image 5 at 1200 Sec	1st Processed Image 6 at 1600 Sec
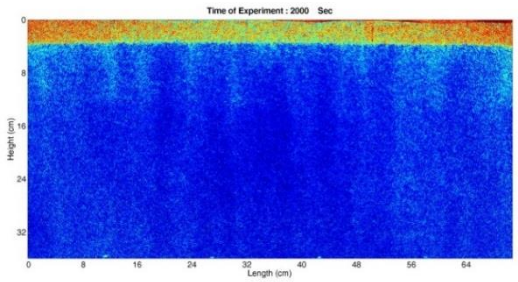	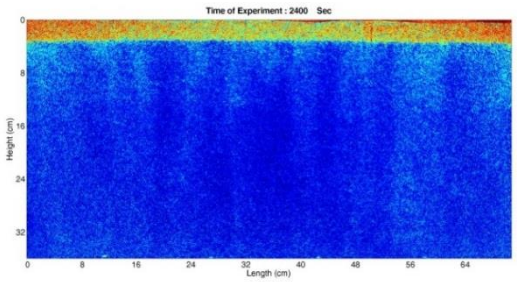
1st Processed Image 7 at 2000 Sec	1st Processed Image 8 at 2400 Sec

Table 4.2 – Continued

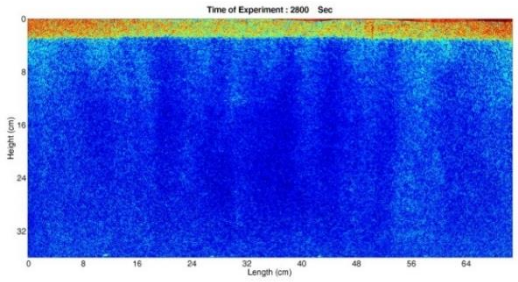	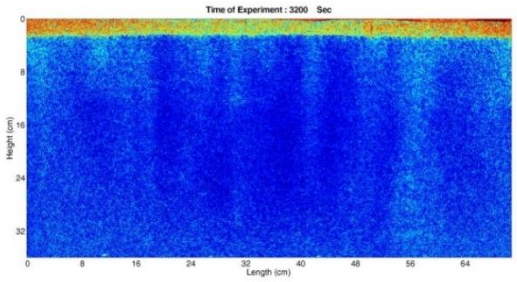
1st Processed Image 9 at 2800 Sec	1st Processed Image 10 at 3200 Sec
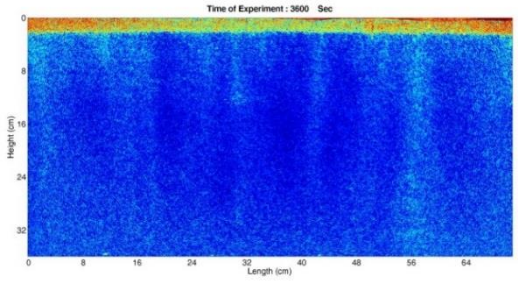	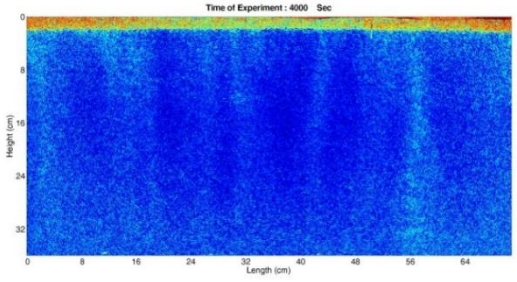
1st Processed Image 11 at 3600 Sec	1st Processed Image 12 at 4000 Sec
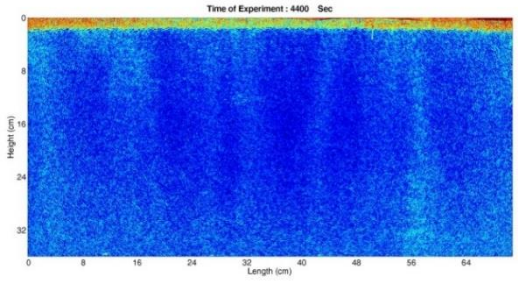	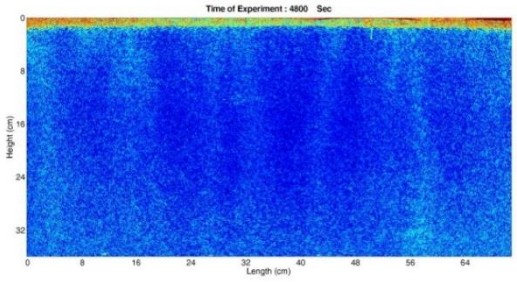
1st Processed Image 13 at 4400 Sec	1st Processed Image 14 at 4800 Sec

Table 4.2 – Continued

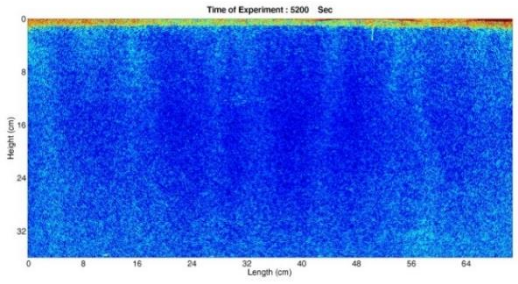	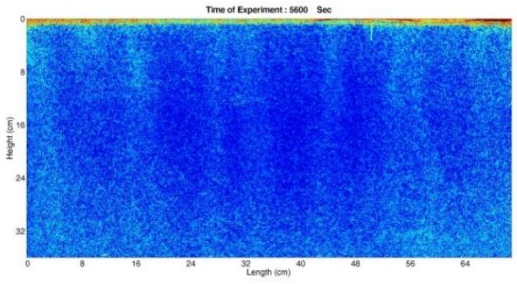
1st Processed Image 15 at 5200 Sec	1st Processed Image 16 at 5600 Sec

After 1st stage processing, more information can be obtained by 2nd stage processing, as shown in Table 4.3. First of all, time function and axis with actual size are added to original experimental images, as shown in the upper-left part of the image. Then, the 1st stage processed images are filtered to avoid noise, as shown in the upper-right part of the image. Along three analysis horizontal layers at different vertical pixel, finger signal, represented by specific value of its contour line, for each layers can be obtained and indicated as the same color line in the lower-left part of the image. In the lower-left part of the images, the interface between MEG and water is indicated as a contour line. It should be noted that the value for the interface contour line for this experimental setting is 0.39, determined by its dye concentration.

Table 4.3 - Image after 2nd processing stage

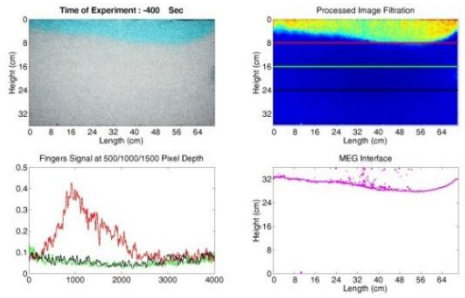	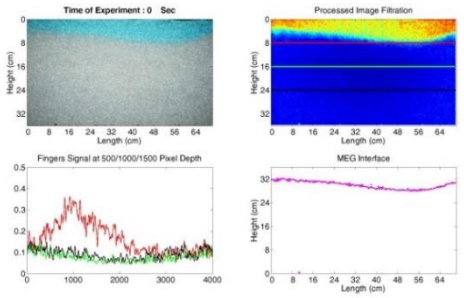
Calibration Image 1 at 0 Sec	1st Processed Image 2 at 10 Sec
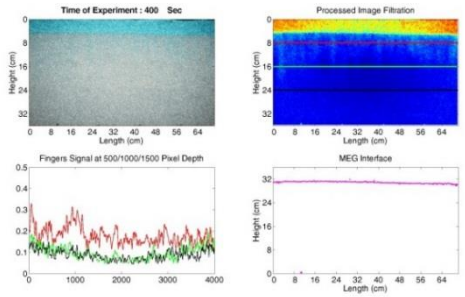	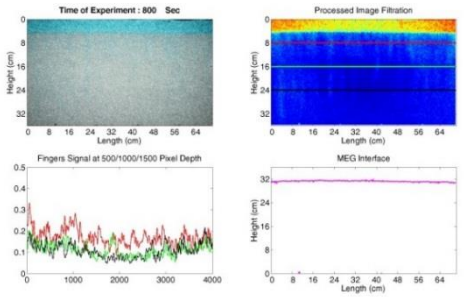
2st Processed Image 3 at 400 Sec	2st Processed Image 4 at 800 Sec
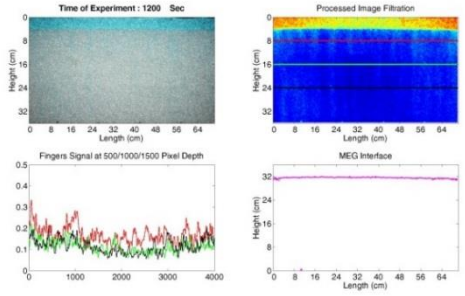	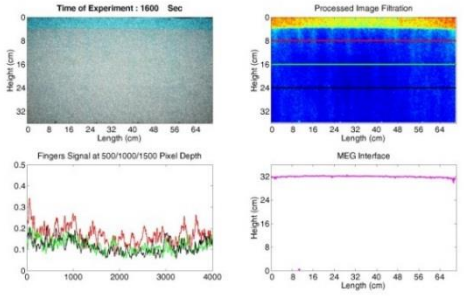
2st Processed Image 5 at 1200 Sec	2st Processed Image 6 at 1600 Sec

Table 4.3 – Continued

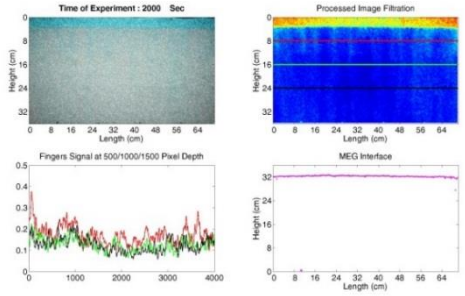	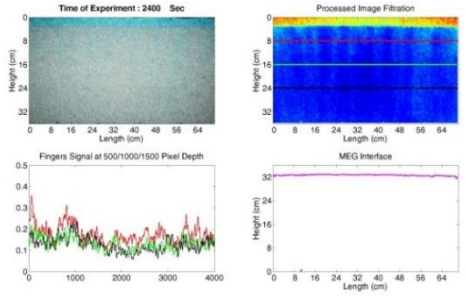
2st Processed Image 7 at 2000 Sec	2st Processed Image 8 at 2400 Sec
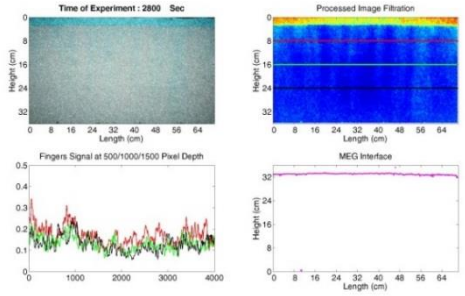	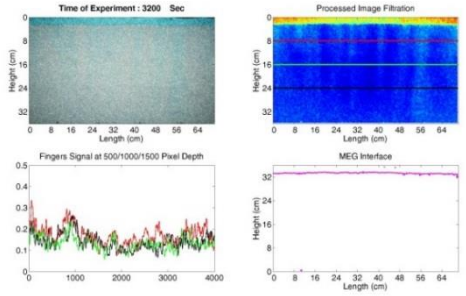
2st Processed Image 9 at 2800 Sec	2st Processed Image 10 at 3200 Sec
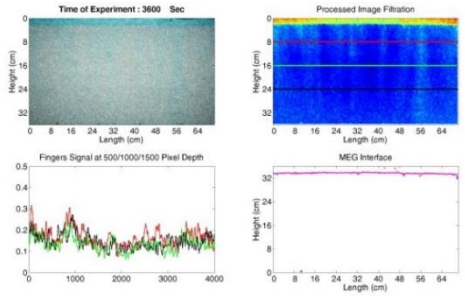	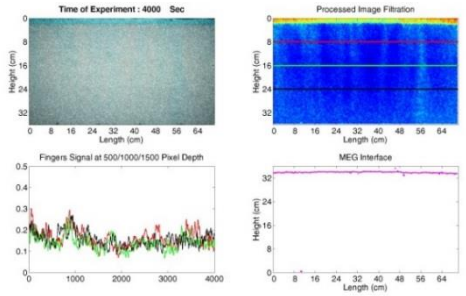
2st Processed Image 11 at 3600 Sec	2st Processed Image 12 at 4000 Sec

Table 4.3 – Continued

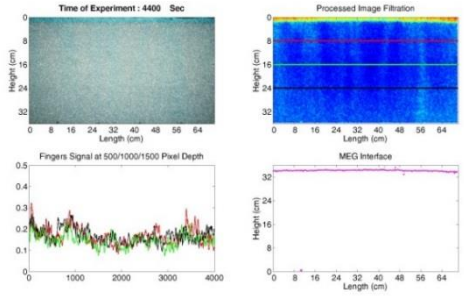	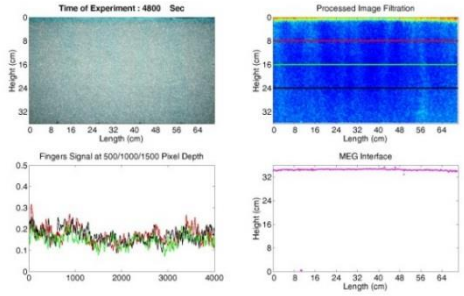
2st Processed Image 13 at 4400 Sec	2st Processed Image 14 at 4800 Sec
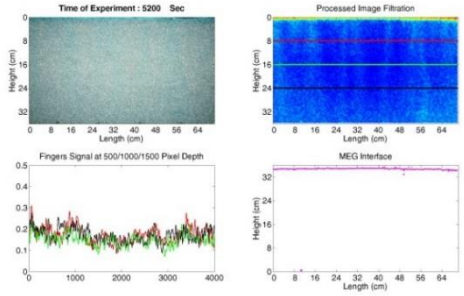	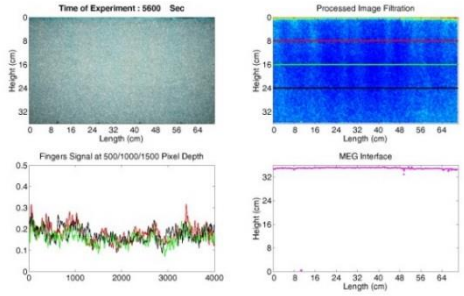
2st Processed Image 15 at 5200 Sec	2st Processed Image 16 at 5600 Sec

4.2 MEG RECEDING INTERFACE ANALYSIS

The MEG convective dissolution rate and controlling factors are the important objective for my research. With more and more MEG forming the MEG- water mixture, the remaining pure MEG volume decreases as a function of time. Therefore, by finding the interface between MEG and water, and then integrating the area above the interface, the remaining MEG area can be calculated since the width of experimental chamber is fixed. Also, a time line is allocated to each image of the experiment, so by processing all images we can obtain the remaining MEG area as a function of time, as shown in Figure 4.1 .The MEG dissolution rate can be also understood as the MEG interface receding velocity since the width and the length of the chamber are fixed. Therefore the MEG dissolution rate can be calculated by measuring the slope of the area vs. time line.

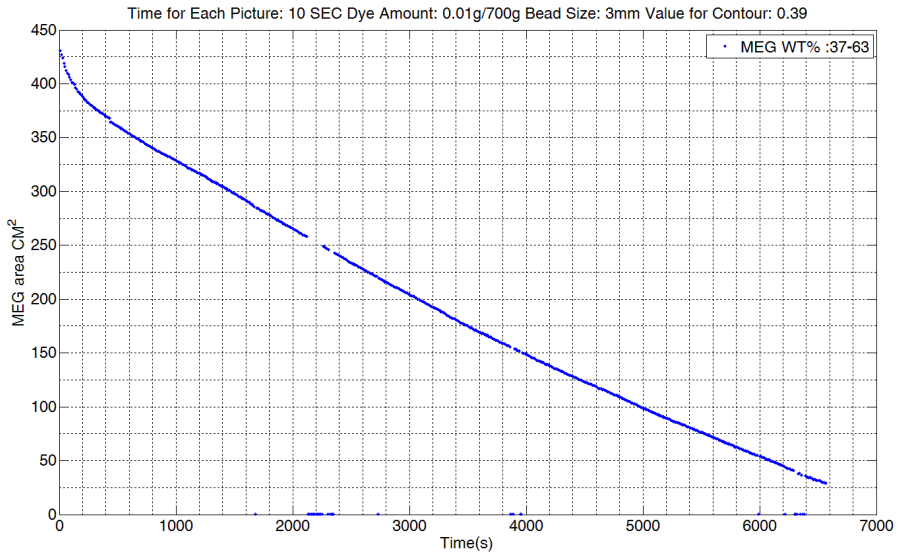

Figure 4.1 - MEG remaining area vs time for 37- 63 MEG in 3 mm beads porous media

Figure 4.1 shows the dependence between MEG remaining area and time for 37-63 MEG with a dye concentration of 0.01g/700g in 3 mm porous media. For 37- 63 MEG with a dye concentration of 0.01g/700g in 3 mm porous media, the density difference$\Delta\rho = 7.3\ kg/\ m^3$, and the permeability$K = 8.1 * 10^{-9} m^2$.

The plot can be divided into three ranges according to different stages. Range 1 for this experimental setting is from 0 s to 400s, with the highest slope on the plot. Range 2 is from 400 s to 2400s, with an intermediate slope. Range 3 is from 2400 s to 6000 s, with the lowest slop. The dissolution rate difference between range 1, range 2 and range 3 is due to its own physical behavior

For Range 1, the MEG is just distributed into porous media, and the MEG interface is not even, as shown in 10s and 400 s experimental images in Table 4.1. At this stages, the MEG tends to have a relatively even interface duo to density difference. Therefore more dynamics may happen during this stage, and cause the highest slope. For Range 2, the MEG interface is relatively even, and the MEG starts to dissolves into water and forms a MEG-water mixture with a higher density. Driven by density difference, this MEG-water mixture flows downward as several fingers. At the same time, water tends to flow upward to dissolve more MEG convectively. At 2400s, fingers first reach the bottom of the experimental chamber, and this range is what we are interested in. For Range 3, more and more MEG dissolves into water, and the corresponding dissolution rate decreases due to its driven force decreasing.

The MEG remaining vole rate can be calculated by the following equation

$$A' = \frac{200 - 325}{3100 - 1000} = -0.05952\ cm^2/s$$

The length of the interested target of the experimental chamber is 71.392 cm therefore, then the interface receding velocity is

$$v_i = \frac{A'}{L} = -\frac{0.05952\,\frac{cm^2}{s}}{71.392\ cm} = 0.000834\ cm/s$$

Therefore, the MEG interface receding velocity for 37 -63 MEG in 3 mm beads packing porosity media is $0.000834\ cm/s$.

By repeating the experimental procedure above, MEG interface receding velocity for the combinations of different MEGs and different porous media can be measured and listed in Table 4.4.

In MATLAB, the corresponding script to measure the MEG interface is listed below.

```
Figure (1)
 imagesc(hsv_ave,[0 1])
Figure (2)
 contour(flipud(hsv_ave),[0.39,0.39]);
 d = contourc(hsv_ave,[0.39,0.39]);
 f = zeros(2,d(2,1));
 f(1:2,1:d(2,1))=d(1:2,2:(d(2,1)+1));
 X = f(1,:);
 Y = f(2,:);
 area = trapz(X,Y);
 area_m(1,jj+1)= area*r*r;
 area_m(2,jj+1)= tt2;
```

```
% Show 1st processing
image in Figure(1)
% Show contour line
with the value of
0.39 in Figure (2)
% computer the contour
matrix, save the
information into a new
matrix, and calculate
related area
% Convert the result
to the actual area
```

Table 4.4 - MEG interface velocity for all experiments measurment

#	MEG Type	Dye Con/700g	Beads Size	MEG Rate cm^2/s	Receding V cm/s
1	33-67	0.05g	2 mm	-0.25	0.003644
2	33-67	0.05g	2 mm	-0.11538	0.001704
3	33-67	0.05g	3 mm	-0.13333	0.001883
4	33-67	0.01g	2 mm	-0.16667	0.002331
5	33-67	0.015g	2 mm	-0.14286	0.002019
6	35-65	0.019g	2 mm	-0.11364	0.00161
7	37-63	0.05g	2 mm	-0.04167	0.000605
8	37-63	0.015g	2 mm	-0.075	0.00106
9	40-60	0.015g	2 mm	-0.025	0.000348
10	40-60	0.05g	2 mm	-0.01563	0.00022
12	35-65	0.01g	3 mm	-0.1	0.001472
13	37-63	0.01g	3 mm	-0.05952	0.000834
14	40-60	0.01g	3 mm	-0.02778	0.000407
15	35-65	0.01g	2 mm	-0.10294	0.001413
16	35-65	0.01g	3 mm	-0.09091	0.001292
17	40-60	0.01g	3 mm	-0.03571	0.000531
18	33-67	0.01g	1.2 mm	-0.075	0.001083
19	35-65	0.01g	1.2mm	-0.05185	0.000714
20	37-63	0.01g	1.2 mm	-0.02778	0.000392
21	40-60	0.01g	1.2mm	-0.00581	0.0000866

4.2.1 MEG Receding Interface Dependence on Fluid

In our experiemnt, four types of MEG with different maximum density difference are used as the analoge fluid. Since the density differnce is the driven force for convective dissolutiuon, we analyze its impact on the receding interface velocity. Figure 4.2 shows the dependence between normalized remaining MEG volume and time of three experiments by different MEGs. The slope of the line gives the interface receding velocity. All three experiments are conducted in the porous media packed by 1.2 mm beads, which means the permeability of the porous media is constant. The red line represents the experiment with 35-65 MEG, green line represents 37-63 MEG, and blue line represents 40 – 60 MEG, which means the driving force for three experiments are different. Apparently, with driving force varing and permeability staying constant, the MEG interface velocities change.

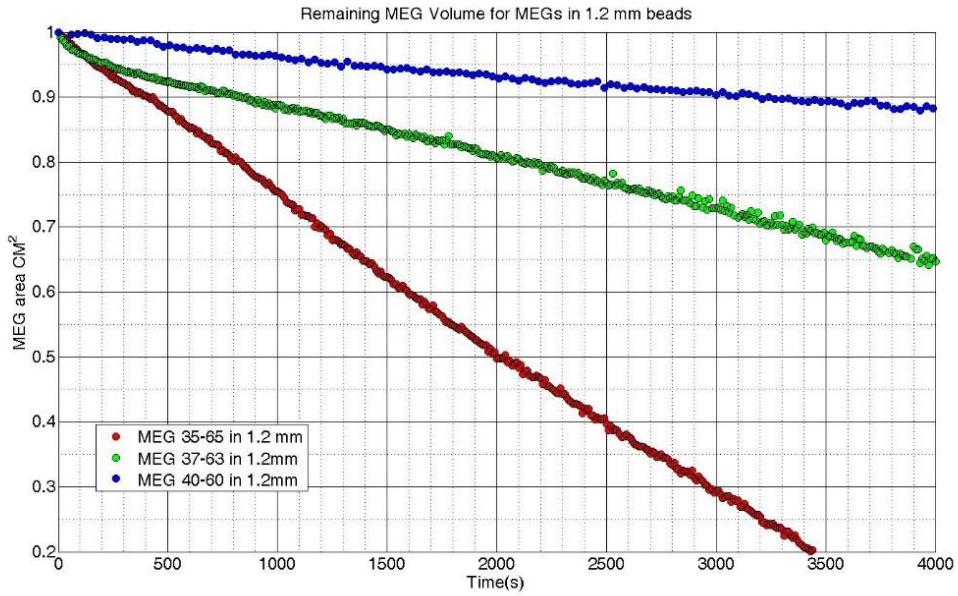

Figure 4.2 - Normalized remaining MEG vs time for three experiments with different MEGs

Figure 4.3 shows the interface receding velocity data for all experiments as a function of maximum density difference. The x axis is the maximum density difference, which is determined by the MEG type, and the y axis is the corresponding MEG interface receding velocity. Each dot represents one independent experiment with one combination of bead size and MEG type. Red dots represents experiments in 1.2 mm beads porous media, green dots represent experiments in 2 mm beads and blue dots represent experiments in 3 mm beads.

As we can observe from the figure, the interfacial flux linearly increases with the density difference increasing. The explanation for this phenomenon will be discussion in next chapter.

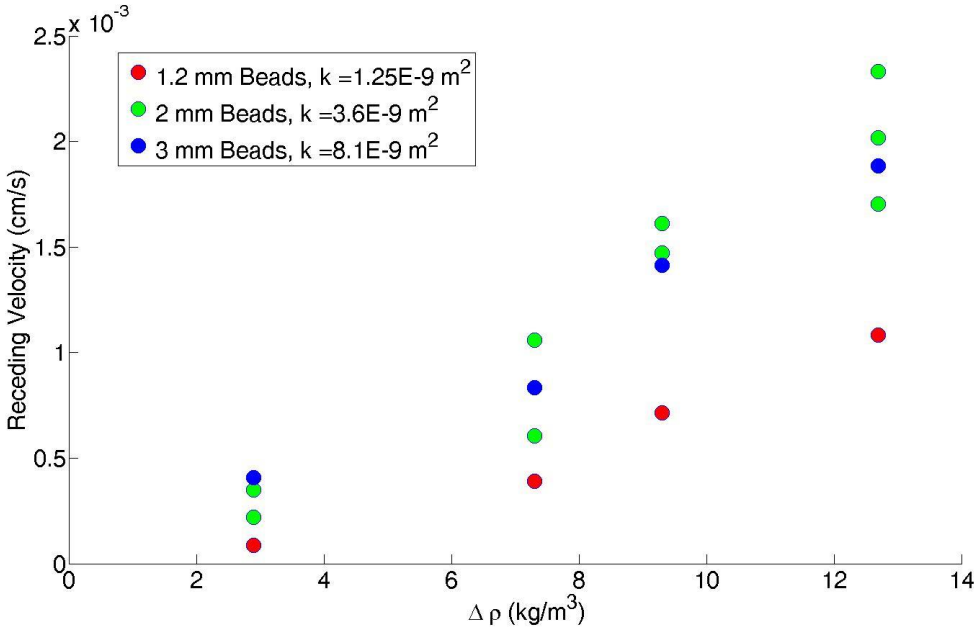

Figure 4.3 - Interface receding velocity vs maximum density difference

4.2.2 MEG RECEDING INTERFACE DEPENDENCE ON MEDIA

Similiarily, three types of beads with different permeaiblity, which is another potential controlling factor for convective dissoluiton, we used to create the porous media. Therefore the permeability impact on the receding interface velocity is also our interest. For example, Figure 4.4 shows the dependece between normalized remaining MEG volume and time of three experiments in different porous media. The slope of the line can be calculated the interface receding velocity. All three experiments are conducted by 35-65 type MEG, which means the driven force for convective dissolution is constant. The red line represents the experiment in 1.2 mm beads packing porous media, blue line represents the experiment in 2 mm beads packing porous media, and green line represents the experiment in 1.2 mm beads packing porous media, which

means the permeability for three experiments are difference. Aparently, with permeability varing and driven force staying constant, the MEG interface velocities also change, determined by the gravitional driven force.

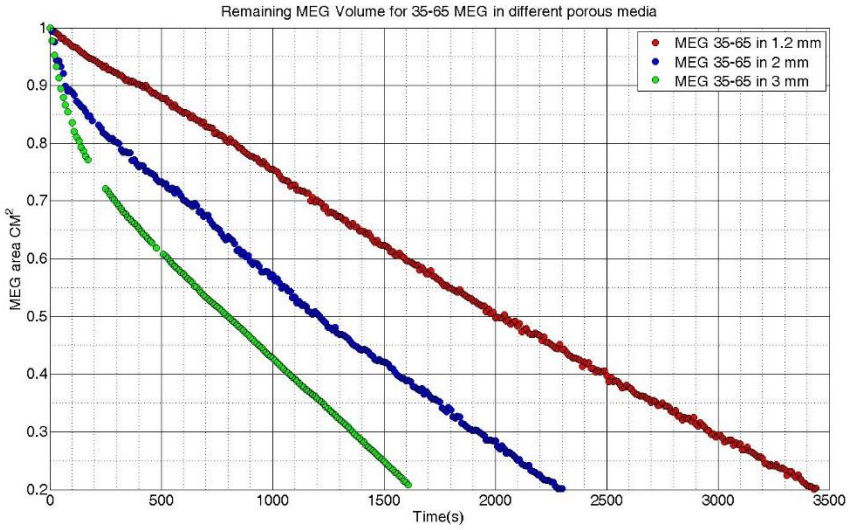

Figure 4.4 - Normalized remaining MEG vs time for three experiments in different media

Figure 4.5 shows the interface receding velocity data for all experiments as a function of permeability of porous media. The x axis is the permeability, which is determined by the bead size distributed in the experimental chamber, and the y axis is the corresponding MEG interface receding velocity. Each dot represents one independent experiment with one combination of bead size and MEG type. Red dots represents experiments by 33-67 MEG, green dots represent experiments by 35 -65 MEG, blue dots represent experiments by 37 -63 MEG and yellow dots represent experiment by 40 – 60 MEG.

As we can observe from the figure, the interfacial flux linearly increases with the permeability increasing before a threshold. After that, the interfacial flux is independent of permeability changes. The explanation for this phenomenon will be discussion in next chapter.

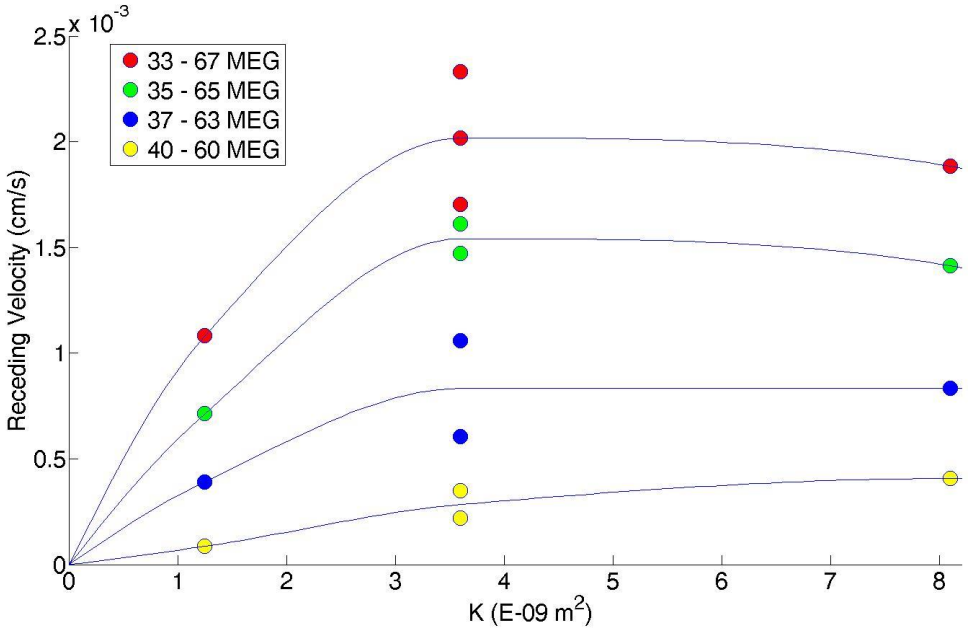

Figure 4.5 - Interface receding velocity vs permeability of porous media

4.3 FINGER PATTERN ANALYSIS

The MEG finger pattern in porous media and controlling factors are another topic of our study, including between MEG types, porous media and time and finger shape, finger number the dependences. When the experimental images are in HSV format, its color saturation can represent the MEG concentration with appropriate calibration.

However, based on current progress the color difference can only be used to distinguish MEG and water roughly. Also, the dye concentration is another key factor for finger pattern analysis. As we can expect, the color of fingers is brighter when more dye is added into MEG. Currently we use 0.01g/700g dye concentration to find clear MEG receding velocity and 0.03g/700g dye concentration to analyze the finger pattern.

Here I take one experiment for an analysis example, 33-67 MEG with 0.01/700 dye in 2 mm beads porous media, as shown in Table 4.5.

The 2nd processed image is listed in the upper-left part of the image. Three horizontal analysis layers at depths 500 pixels, 1000 pixels and 1500pixels of the experimental chamber are analyzed. Along these three horizontal layers, contour value for each point along the x axis is recorded as a function of time. If the value is beyond a certain number, we define at that area, there is a finger existing. The upper-right image is the contour value along the x axis at depth 500 pixels, the lower- left is the contour value along the x axis at depth 1000 pixels, and the lower-right is the contour value along the x axis at depth 1500 pixels. Still, the exact number to distinguish fingers and non-fingers depends on dye concentration, so it is still in progress.

Table 4.5 - Finger pattern analysis for 33-67 MEG with 0.01/700 dye in 2 mm beads porous media

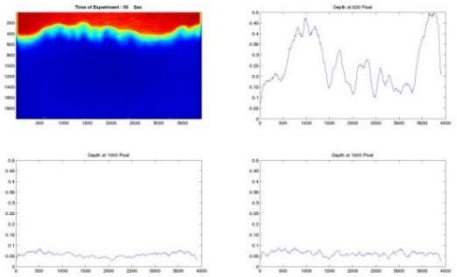	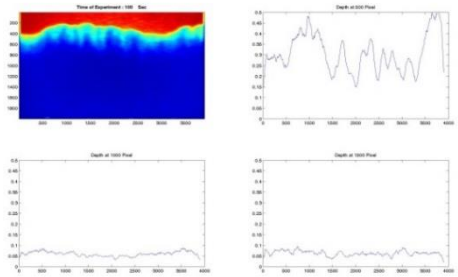
Calibration Image 1 at 0 second	Processed Image 2 at 100 second
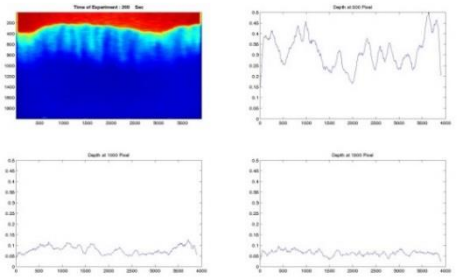	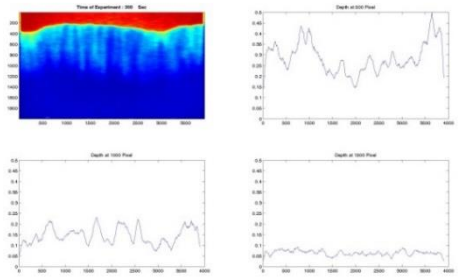
Processed Image 3 at 200 second	Processed Image 4 at 300 second
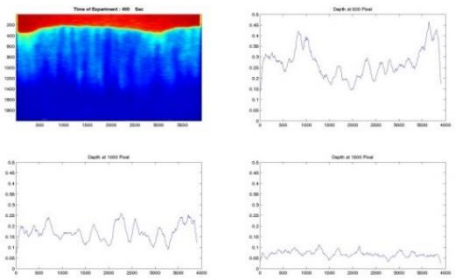	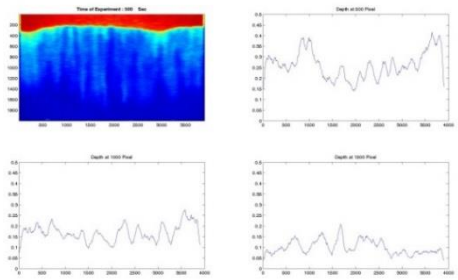
Processed Image 5 at 400 second	Processed Image 6 at 500 second

Table 4.5 – Continued

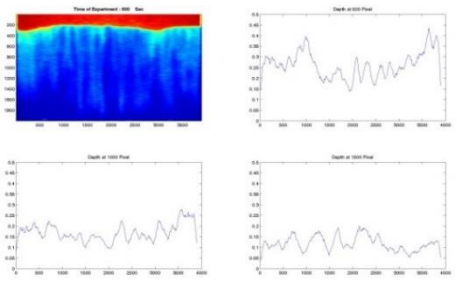	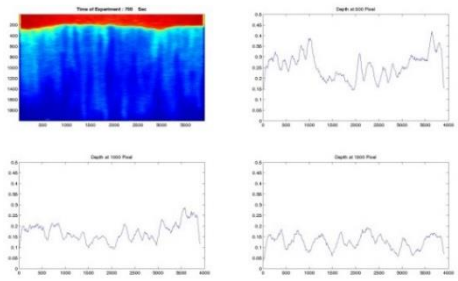
Processed Image 7 at 600 second	Processed Image 8 at 700 second
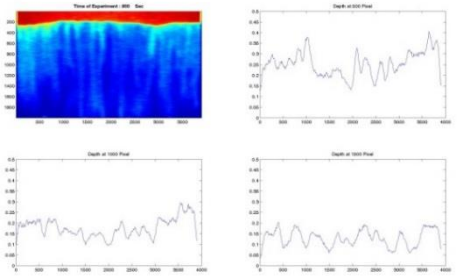	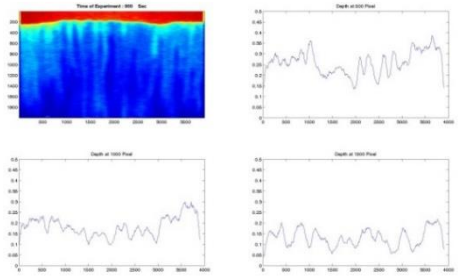
Processed Image 9 at 800 second	Processed Image 10 at 900 second
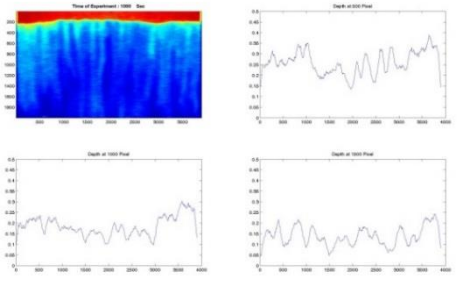	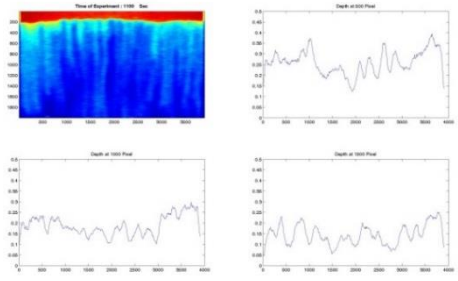
Processed Image 11 at 1000 second	Processed Image 12 at 1100 second

Table 4.5 – Continued

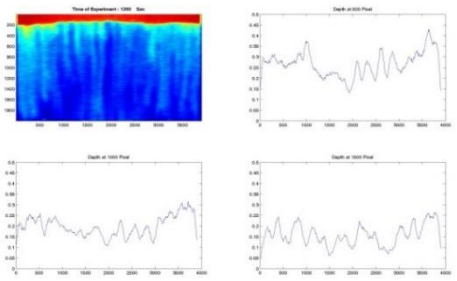	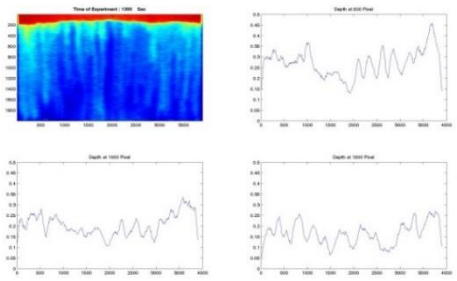
Processed Image 13 at 1200 second	Processed Image 14 at 1300 second
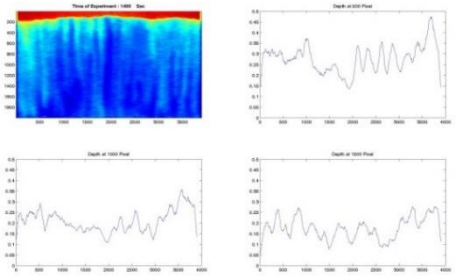	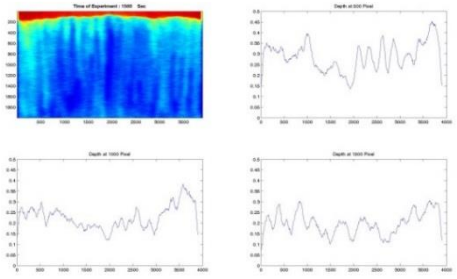
Processed Image 15 at 1400 second	Processed Image 16 at 1500 second

4.3.1 FINGER PATTERN DEPENDENCES

As we expect, the permeability of the porous media, the maximum density difference, and the time could potentially be the controlling factors to determine finger pattern, which includes finger number, finger shape and so on. However, due to the limit of our current understanding in this area, I am still working on optimizing the method to study the finger pattern consistently. Right now we can only analyze its dependences roughly. Take one study as an example, as shown in Figure 4.6. The upper image is 35-65 type MEG in 1.2 mm beads packing porous media and the lower image is 35-65 type

MEG in 3 mm beads. If we define one brighter column as one convective dissolution finger regardless of its width, then totally there are 22 fingers in 1.2 mm porous media and there are 9 fingers in 3 mm porous media.

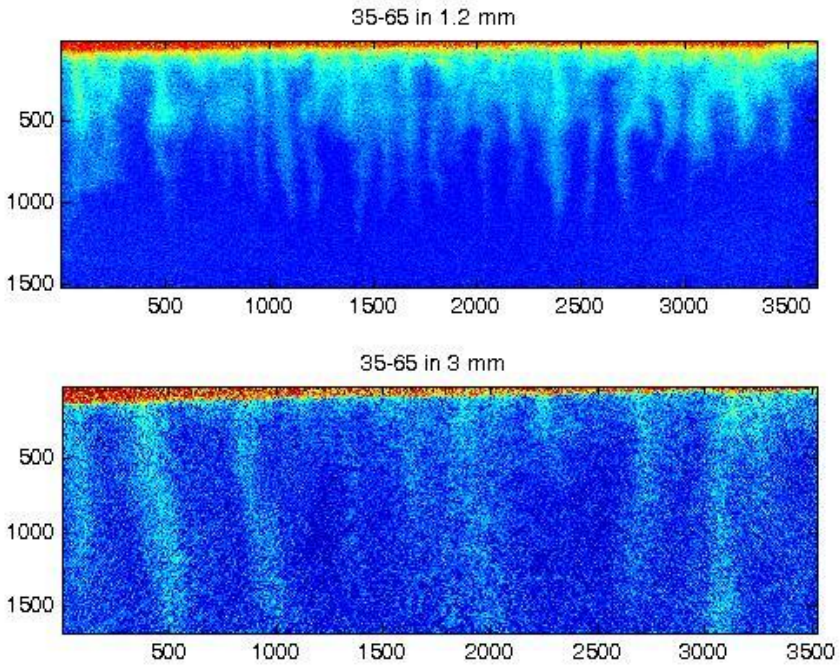

Figure 4.6 - Processed fingers of 35-65 MEG in 1.2 mm and of 35-65 MEG in 3 mm

Roughly, observed fingers numbers for all experiments are concluded in Table 4.6.

Table 4.6 - Fingers number for all experiments measurement

Glass Beads Size	MEG TYPE	Dye Amount g dye/700g MEG	Large Fingers
1.2 mm	33-67	0.01g	24
1.2 mm	35-65	0.01g	22
1.2 mm	37-63	0.01g	15
1.2 mm	40-60	0.01g	10
2 mm	33-67	0.05g	19
2 mm	33-67	0.01g	15
2 mm	33-67	0.015g	16
2 mm	35-65	0.01g	15
2 mm	35-65	0.019g	16
2 mm	37-63	0.05g	17
2 mm	37-63	0.015g	14
2 mm	40-60	0.015g	19
2 mm	40-60	0.05g	20
3 mm	33-67	0.01g	13
3 mm	35-65	0.01g	9
3 mm	37-63	0.01g	6
3 mm	40-60	0.01g	5

Figure 4.7 shows the finger number as a function of maximum density difference. Each dot represents one independent experiment with a certain combination of bead size and MEG type. Red dots represents experiments in 1.2 mm beads porous media, green dots represent experiments in 2 mm beads and blue dots represent experiments in 3 mm beads. Figure 4.8 shows the dependence between finger number and permeability of the porous media, which is determined by the bead size distributed in the experimental chamber. Red dots represents experiments by 33-67 MEG, green dots represent experiments by 35 -65 MEG, blue dots represent experiments by 37 -63 MEG and yellow dots represent experiment by 40 – 60 MEG.

Roughly we can observe that, the finger number increases linearly as the density difference increasing, and finger number decreases linearly as the permeability of the porous media increases. The potential physical explanation is discussed in next chapter.

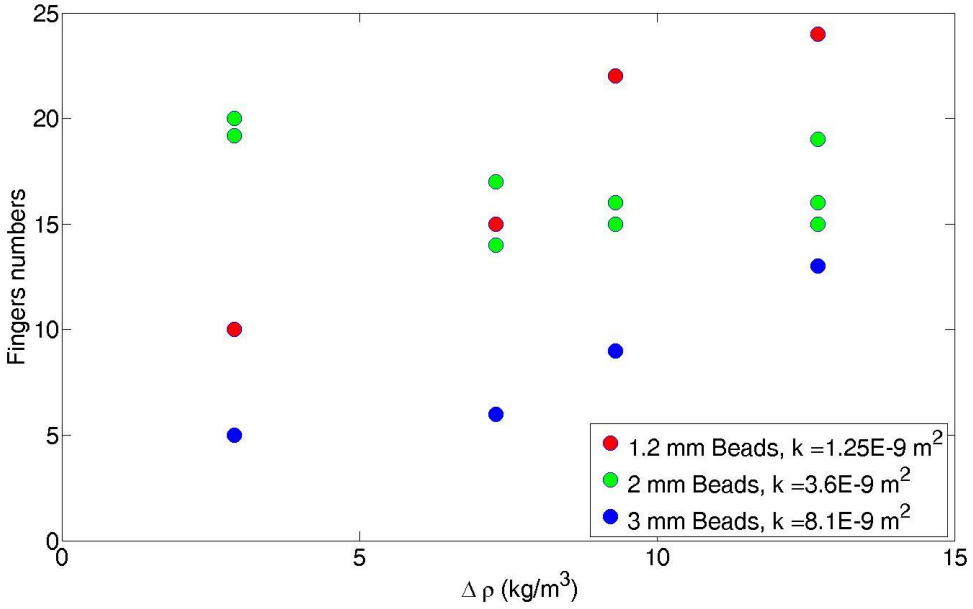

Figure 4.7 - Finger number vs. maximum density difference

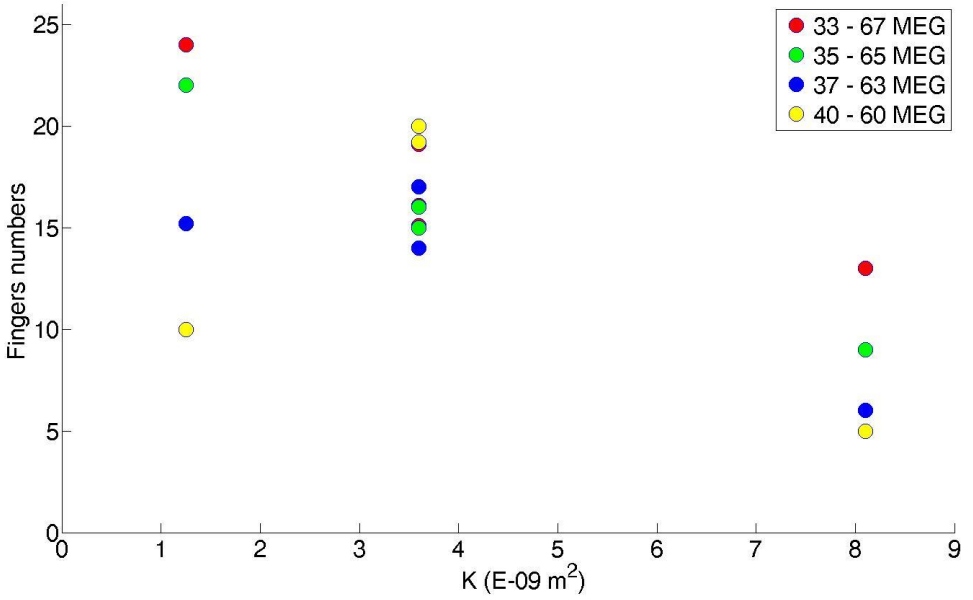

Figure 4.8 - Finger number vs. permeability of the glass packing porous media

CHAPTER 5: DISCUSSION

5.1 MEG RECEDING DEPENDENCE OBSERVATIONS

According to the results obtained, there are a very interesting dependencies between the convective dissolution rate and the maximum density difference, between the convective dissolution rate and the permeability of the porous media. As we can observe from Figure 4.3 - Interface receding velocity vs maximum density difference, for experiments conducted in the same porous media with certain permeability, the MEG receding interface velocity increases linearly as the maximum density difference increases. This sample dependence between dissolution rate and maximum density difference is expected. The CO_2 convective dissolution dynamics is driven by the maximum density difference, therefore their dissolution rates increase as a function of driven force increasing , from a lower maximum density difference (40 -60 MEG) to a higher maximum density difference (33-67 MEG).

Figure 4.5 - Interface receding velocity vs permeability of porous media shows a surprising dependence between the MEG interface receding velocity and the permeability of the experimental porous media. For the experiments with same types of MEG, the MEG interface velocity first increases linearly, which is expected, unexpected stays constant as the further permeability increases. As we know, if we increase the permeability of the porous media with a constant driving force, the dissolution rate should also increases linearly. However, between the 2mm beads packing porous media with permeability of $3.6 * 10^{-9}\, m^2$ and 3mm beads packing porous media with

permeability of $8.1 * 10^{-9}\, m^2$, all four types of MEG with an increasing driven force have constant interface receding velocities even though the permeability of the porous media increases 2.1 times. Therefore, there must be a physics existing in the CO2 convective dissolution process in the porous media which is not simple, and this physics phenomenon might be very important to characterize the CO2 convective dissolution trapping in the field scale.

5.2 RAYLEIGH NUMBER AND SHERWOOD NUMBER INTRODUCTION

Therefore, in order to have a better understanding of CO2 convective dissolution dynamic and controlling factors, as well as the dependence between the convective dissolution rate and the permeability of the porous media, two dimensionless numbers, Sherwood number and Rayleigh number, are introduced.

The Sherwood number is defined by

$$Sh = F_c/(\phi \Delta D_m/H) \quad (7)$$

$$F_c = \phi v_i \Delta \quad (8)$$

where F_c is the measured convective flux (m/s), ϕ is the porosity, Δ is the concentration difference between pure MEG and water, v_i is the interfacial velocity, D_m is the diffusivity (m^2/s) and H is the height of the reservoir(m).

$$Ra = kg\Delta\rho H/(\phi D_m \mu) \quad (9)$$

where k is the permeability of the system (m^2), ϕ is the porosity, g is the gravitational acceleration (m/s^2), H is the height of the reservoir (m), $\Delta\rho$ is the maximum density difference (kg/m^3), D_m is the diffusivity (m^2/s) and μ is the viscosity of MEG $(Pa * s)$

Permeability depends on bead sizes and maximum density difference depends on MEG types, therefore, a range of Rayleigh numbers can be obtained by using

combinations of different sizes beads and different types of MEG. For each Rayleigh number, a Sherwood number can be calculated by measuring the interfacial velocity in the specific experimental setting. Then a range of corresponding Sherwood numbers can be obtained.

By finding the dependence between the Sherwood numbers and the Rayleigh number, we can understand how fast CO2 convective dissolution process can happen. The advantage of dimensionless number is that all research results can be upscaled to field scale. In other words, the Sherwood numbers and the Rayleigh numbers work as the link between experiment study and field application.

For the example discussed in the chapter 4, 37- 63 MEG with a dye concentration of 0.01g/700g in 3 mm porous media, the Rayleigh number can be calculated as

$$Ra = \frac{kg\Delta\rho H}{\phi D_m \mu} = \frac{8.1 * 10^{-9} * 9.8 * 0.35 * 7.3}{0.425 * 10^{-9} * 0.0032} = 148876$$

For that experiment setting, the corresponding Sherwood number can be calculated

$$Sh = \frac{v_i H}{D_m} = \frac{0.000834 * 0.35 * 0.01}{10^{-9}} = 2918.16$$

Then the dependence between Sherwood number and Rayleigh number for the experiment by 37- 63 MEG with a dye concentration of 0.01g/700g in 3 mm porous media can be plotted in Figure 5.1.

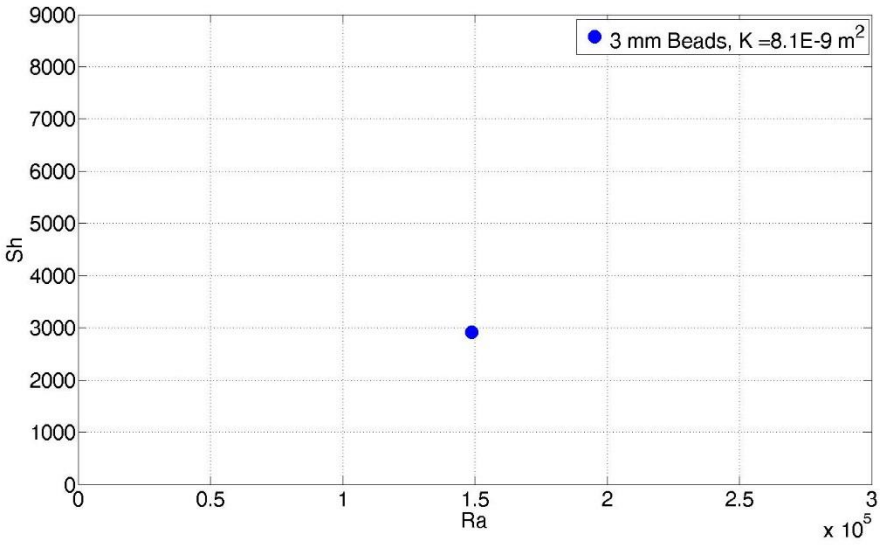

Figure 5.1 - Sh vs Ra for the 37- 63 MEG with a dye concentration of 0.01g/700g in 3 mm porous media

Since currently we have 3 sizes of glass beads and four types of MEG, totally there are 12 Rayleigh numbers as the variables. For combinations of different MEG types and different beads sizes, Rayleigh numbers are listed in Table 5.1.

Table 5.1 - Rayleigh numbers based on current beads and MEGs

Rayleigh Number	1.2 mm	2 mm	3mm
40-60	13580.96	26285.73	59142.89
37-63	34186.55	66167.52	148876.9
35-65	43552.73	84295.61	189665.1
33-67	59475.24	115113.4	259005.1

By conducting experiments based on each Rayleigh number, corresponding Sherwood number can be calculated by measuring the interfacial velocity. Table 5.2 shows all experimental measurement results.

Table 5.2 - Rayleigh numbers and Sherwood numbers for all experiments measurements

Exp #	MEG Type	Beads Size	Ra Number	SH Number
1	33-67	2 mm	115113.4	12752.87
2	33-67	2 mm	115113.4	5963.822
3	33-67	3 mm	259412.3	6591.337
4	33-67	2 mm	115113.4	8156.911
5	33-67	2 mm	115113.4	7066.738
6	35-65	2 mm	84295.61	5636.165

Table 5.2 – Continued

7	37-63	2 mm	66167.52	2117.362
8	37-63	2 mm	66167.52	3710.038
9	40-60	2 mm	26285.73	1219.393
10	40-60	2 mm	26285.73	770.4635
12	35-65	3 mm	189665.1	5150.846
13	37-63	3mm	148876.9	2918.161
14	40-60	3 mm	59142.89	1424.71
15	35-65	2 mm	84295.61	4947.192
16	35-65	3 mm	189665.1	4522.198
17	40-60	3 mm	59142.89	1860.119
18	33-67	1.2 mm	59475.24	3789.027
19	35-65	1.2mm	43552.73	2497.681
20	37-63	1.2 mm	34186.55	1371.104
21	40-60	1.2mm	13580.96	303.0987

Figure 5.2 shows Rayleigh numbers and Sherwood numbers for all experimental results on a linear scale axis. Figure 5.3 shows Rayleigh numbers and Sherwood numbers for all experimental results on a loglog scale axis.

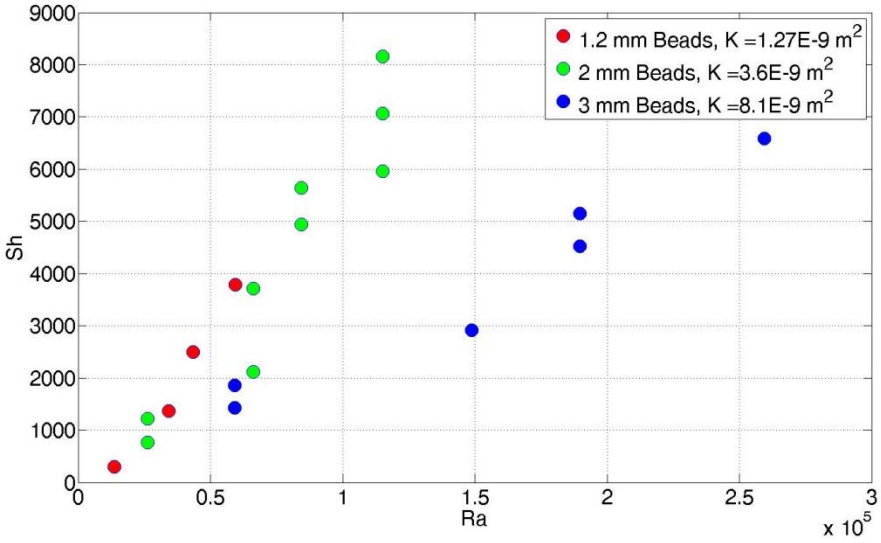

Figure 5.2 - Rayleigh numbers and Sherwood numbers for all experimental results on a linear scale axis

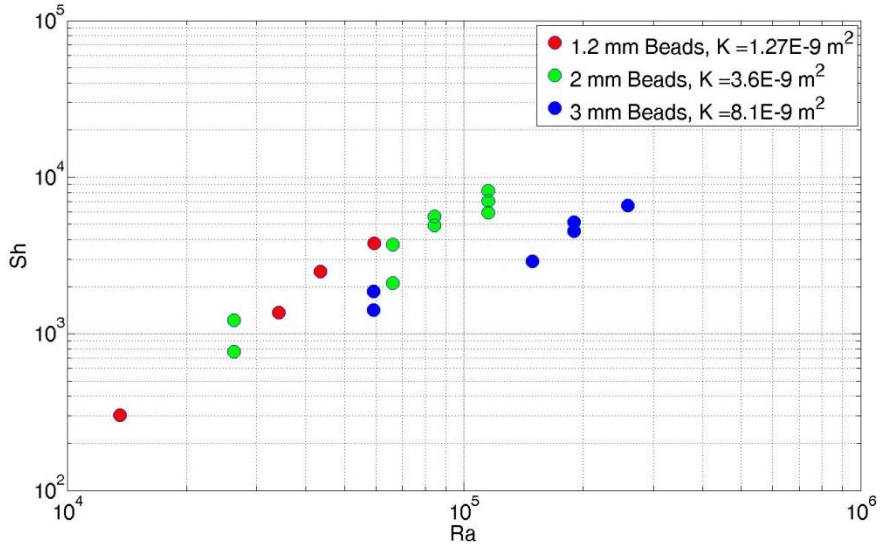

Figure 5.3 - Rayleigh numbers and Sherwood numbers for all experimental results on a loglog scale axis

Previous studies shows the dependence between Sherwood numbers and Rayleigh numbers can be fit back to a straight line in loglog axis, which is an exponential mathematical relationship between Sherwood numbers and Rayleigh numbers. However, according to the experiment results I obtained, loglog plot actually squeeze all data together to fit a straight line. From Figure 5.4 we can conclude that experiments conducted in the porous media with a permeability smaller than $3.6 * 10^{-9}\, m^2$, 1.2 mm beads packing porous media and 2 mm beads packing porous media in other words, there is a linear relationship between Sherwood numbers and Rayleigh numbers in the linear axis system. But for 3 mm beads packing porous media, it has its own dependence between Sherwood numbers and Rayleigh numbers, as shown in Figure 5.4. For a glass beads packing porous media, the permeability is determined by the beads size. Therefore the bead size could be a key point to explain the phenomenon. This results is also consistent to the observation of the dependence between convective flux and permeability of the porous media that the convective flux is independent of permeability after a bead size threshold.

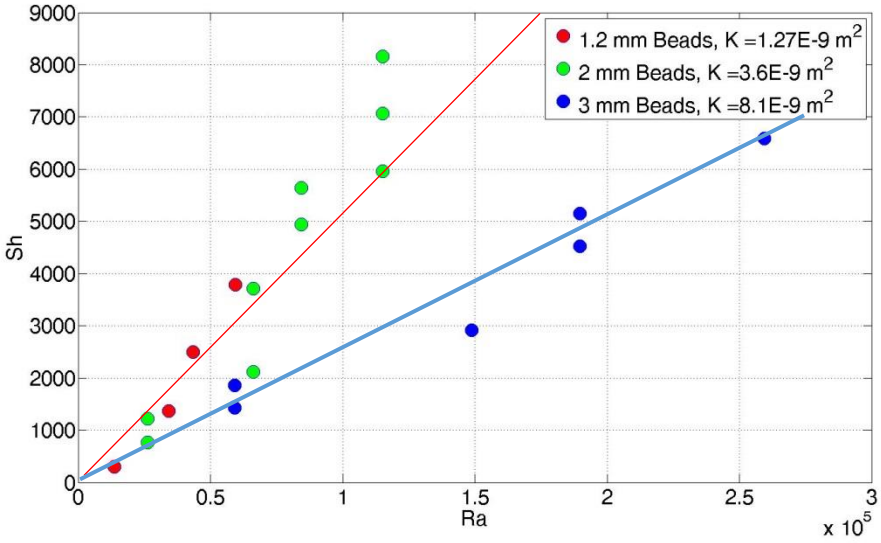

Figure 5.4 - Different dependences between Rayleigh numbers and Sherwood numbers

5.3 HYPOTHESIS OF TRANSVERSE DISPERSION

5.3.1 HYDRAULIC DISPERSION EFFECT

According to the experiment results, currently we have four main observations,

- The connective dissolution flux is linearly dependent of the maximum density difference change.
- The convective dissolution flux is linearly dependent of the permeability change before a bead size threshold.
- The convective dissolution flux is independent of the permeability change after that bead size threshold.
- The exponential dependence between Sherwood numbers and Sherwood number by previous studies is invalid after that bead size threshold.

We think it is the transverse hydraulic dispersion effect that hinders convective dissolution flux after that bead size threshold. When the maximum density difference is increased, the only parameter changed is the driving force. MEG and water still have same flowing pattern and same dispersion effect, and that is the reason why connective dissolution flux is linearly dependent of the maximum density difference change. However, when we increase the bead size, on one hand we increase the permeability which could increase convective dissolution flux under same driven force. However, on the other hand we also increase the transverse hydraulic dispersion effect between MEG and water. Before the bead size threshold, the positive impact caused by permeability increasing is larger than the negative impact caused by transverse hydraulic dispersion

effect. That is the reason why the convective dissolution flux is linearly dependent of the permeability change. After that bead size threshold, apparently the positive impact caused by permeability increasing is smaller than the negative impact caused by transverse hydraulic dispersion effect, then the convective dissolution flux is independent of the permeability change.

Current Rayleigh number, which works as a variable, only includes convection effect and diffusion effect while the dispersion effect is ignored. That would be the reason why exponential dependence between Sherwood numbers and Sherwood number invalid after the dispersion effect is large enough.

5.3.2 HYDRAULIC DISPERSION MODEL

Previous Rayleigh number is defined as$Ra = kg\Delta\rho H/\phi D_m\mu = VH/D_m$, where $V = kg\Delta\rho/\phi\mu$ is the convection flux (m/s) and$D_m$is the molecular diffusivity (m^2/s).

Instead, the transverse dispersion is added into the equation as

$$Ra^* = kg\Delta\rho H/\phi D\mu = VH/D \quad (10)$$

$$D = D_m + \alpha_T V \quad (11)$$

Where α_T is the transverse dispersivity of the experimental chamber (m)

Combined Eqn (4) and Eqn (5), then the Ra^* is modified to

$$Ra^* = 1/(\frac{1}{Ra} + \frac{\alpha_T}{H}) \quad (12)$$

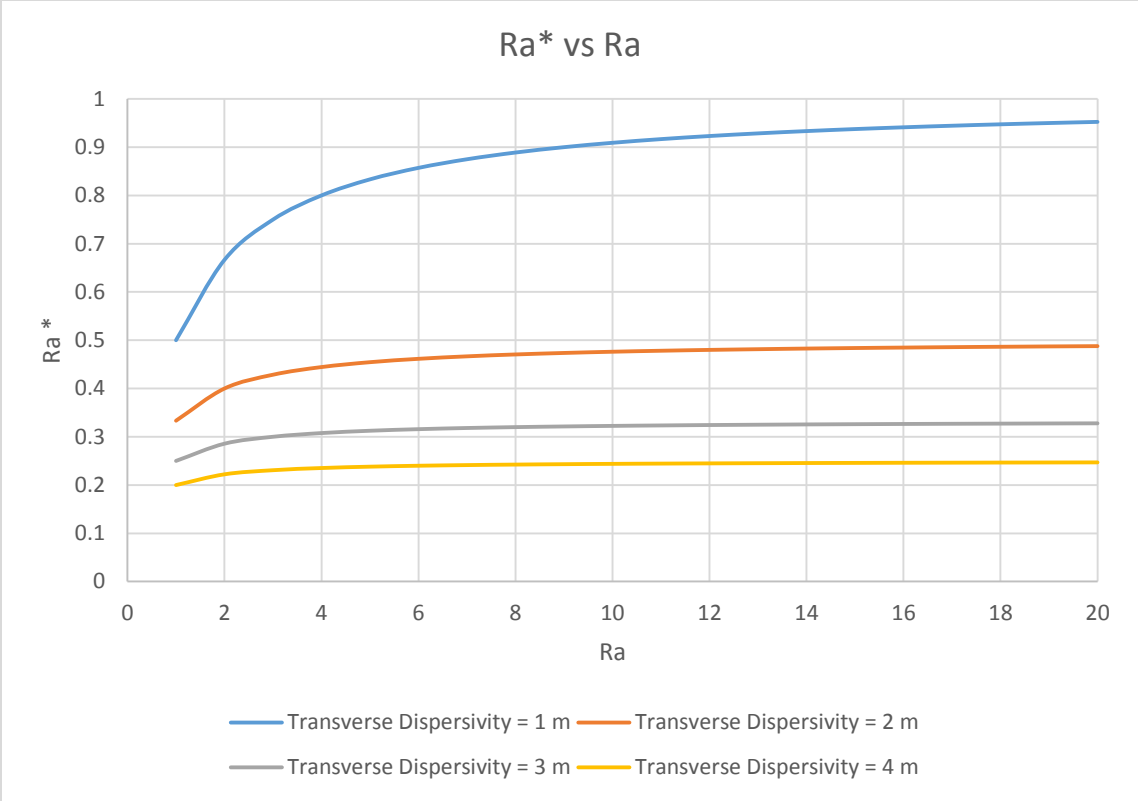

Figure 5.5 - Dependence between Ra * and Ra

As we can observe from Figure 5.5, if the dispersivity is indluded in Rayleigh number, then Ra^* has a maximum value depends on the transverse dispersivity. Then the observation of different dependences between Sherwood number and Rayleigh number for different bead sizes could be explained. If the bead size is larger than the threshold, then Ra^* reaches its maximum value and stays constant, as the trend shown in Figure 5.5, then probably the Sherwood number could be fit back with new Rayleigh number. Therefore, the hydraulic transverse dispersion can not only explain the experimental

observation from physics perspective, it should also characterize the dependence from mathematics perspective.

Also, the maximum value for Ra^* is determined by the transverses dispersivity. Therefore accurate measurement and calculation of the transverse dispersivity of the convective dissolution experiments is necessary. Current experiments to determine transverse dispersivity are in progress. Once the hypothesis of hydraulic dispersion can be proven, a great advance will be made for the understanding of the CO2 convective dissolution trapping mechanism.

5.4 FINGER PATTERN OBSERVATIONS

Based on current progress, there are some interesting observations on finger pattern

- For experiments conducted in the same porous media with certain permeability, the convective dissolution fingers numbers increases as the maximum density difference increases.
- For experiments conducted by the same type of MEG with a certain driven force, the convective dissolution fingers numbers decreases as the permeability increases, while their fingers widths become larger.

It should be noted that these are temporary conclusions with abnormal data due to limit analysis method. The second observation is very interesting. Previous studies show that with permeability increasing, more fingers were observed, which is opposite to what I have observed. If we try to use the hypothesis of dispersion to explain the observation, then we can conclude that transverse dispersion would force MEG to form larger fingers at the interface, which makes sense from physics perspective.

Again, more finger pattern analysis is in progress and all these conclusions on finger pattern is temporary.

CHAPTER 6: CONCULSIONS AND RECOMMENDATIONS

6.1 CONCLUSIONS

The main objective of this research is to study the CO2 convective dissolution dynamics process and controlling factors on the convective dissolution rate and the finger dynamic pattern. In order to approach the problem, analog fluid systems of MEGs and water are used to mimic the density behaviors of CO2 and brine. Glass beads are used to create a homogenous porous media where convective dissolution can take place. The video capture system combined with the image analysis method is used to calculate convective dissolution rate and to analyze finger pattern. Based on current studies, the following conclusions can be made

- The convective dissolution rate is linearly dependent of the gravitational driven force.
- The permeability is determined by the bead size. For sizes below the bead size threshold, with the beads size increasing, permeability increasing is the dominant effect therefore the convective dissolution rate increases correspondingly. Once the bead size reaches the threshold, with the bead size increasing, the permeability increasing effect and the transverse dispersion effect are equally dominant, which cause convective dissolution staying constant.
- Because of the conclusion above, the previous dependence between Sherwood numbers and Rayleigh numbers is not found due to permeability move the threshold.

- We introduce a modified Rayleigh number includes a dispersivity term in its equation. Accurate measurement of the dispersivity is very essential to determine the correct dependence between Sherwood numbers and modified Rayleigh numbers.
- The finger numbers during the convective dissolution process increases as the gravitational driven force increases.
- The fingers numbers during the convective dissolution process decreases as the permeability of the porous media increase, while the fingers widths become larger.
- Transverse dispersion effect could be the reason to for the phenomenon that the fingers width is larger but fingers numbers become less with an increasing beads size.

6.2 FUTURE WORK

The present experimental study on CO_2 convective dissolution shows that this dynamics process is determined not only by the driven force and the permeability of the porous media, but also by the transverse hydraulic dispersion effect. According to the conclusions, in the future following works is recommended to be finished.

- A dispersion experiments will be set up to measure the dispersivity of the analog fluid system. Then the dependence between modified Rayleigh numbers and Sherwood numbers will be conclude to testify the hydraulic dispersion hypothesis.
- Smaller beads will be used to create a porous media with smaller permeability. Then the dependence of modified Rayleigh number and Sherwood number at a lower range will be explored.
- Dependence of modified Rayleigh number and Sherwood number will be used to characterize the dissolved CO_2 distribution in the porous media, as well as to estimate CO_2 convective dissolution rate in geological CO_2 field.
- Image analysis method will be optimized to qualitatively and quantitatively study the gravitational fingers dynamics and relevant controlling factors on finger pattern including shapes, numbers and so on.
- A novel 3-D experimental porous media environment with X-ray technique will be set up. Then a 3-D visualization and modeling of CO_2 convective dissolution process will be studied

- Then dynamics of CO_2 convective dissolution process and the dynamics of gravitational finger pattern in 3-D porous environment will be analyzed.

REFERENCES

Bachu, S., & Adams, J. J. (2003). equestration of CO2 in geological media in response to climate change: capacity of deep saline aquifers to sequester CO2 in solution. *Energy Conversion and Management*, 3151–3175.

Bachu, S., & Stewart, S. (2002). Geological sequestration of anthropogenic carbon dioxide in the western canada sedimentary basin: Suitability analysis. *Journal of Canadian Petroleum*, 32 - 40.

Backhaus, S., Turitsyn, K., & Ecke, R. E. (2011). Convective Instability and Mass Transport of Diffusion Layers in a Hele-Shaw Geometry. *PHYSICAL REVIEW LETTERS*.

Bondor, P. L. (1992). Applications of carbon dioxide in enhanced oil recovery. *Energy Convers. Manage.*, 579–586.

Ennis-King, J., Preston, I., & Paterson, L. (2005). Onset of convection in anisotropic porous media subject to a rapid change in boundary conditions. *Physics of Fluids*, 8.

Faisal, T. F., Chevalier, S., Bernabe, Y., Juanes, R., & Sassi, M. (2015). Quantitative and qualitative study of density driven CO2 mass transfer in a vertical Hele-Shaw cell. *International Journal of Heat and Mass Transfer*, 901 - 914.

Farajzadeh, R., Salimi, H., Zitha, P. L., & Bruining, H. (2007). Numerical simulation of density-driven natural convection in porous media with application for CO2 injection projects. *International Journal of Heat and Mass Transfer*, 5054–5064.

Gasda, S. E., Bachu, S., & Celia, M. A. (2004). Spatial characterization of the location of potentially leaky wells penetrating a deep saline aquifer in a mature sedimentary basin. *Environmental Geology*, 707-720.

Gasda, S. E., Nordbotten, J. M., & Celia, M. A. (2011). Vertically averaged approaches for CO2 migration with solubility trapping. *WATER RESOURCES RESEARCH*.

Hesse, M. A., Tchelepi, H. A., & Orr Jr, F. M. (2006). Scaling analysis of the migration of CO2 in saline aquifers. *SPE Annual Technical Conference and Exhibition.* San Antonio: Society of Petroleum Engineers.

Hewitt, D. R., Neufeld, J. A., & Lister, J. J. (2012). Ultimate Regime of High Rayleigh Number Convection in a Porous Medium. *PHYSICAL REVIEW LETTERS*.

Hidalgo, J. J., Fe, J., Cueto-Felgueroso, L., & Juanes, R. (2012). Scaling of Convective Mixing in Porous Media. *PHYSICAL REVIEW LETTERS*.

Holloway, S., & Savage., D. (1993). The potential for aquifer disposal of carbondioxide in the UK. *Energy Conversion and Management*, 925–932.

Holtz, M. H. (2002). Residual gas saturation to aquifer influx: A calculation method for 3-D computer reservoir model construction. *SPE Gas Technologies Symposium.* Calgary: Society of Petroleum Engineers .

House, K. Z., Schrag, D. P., Harvey, C. F., & Lackner, K. S. (2006). Permanent carbon dioxide storage in deep-sea sediments. *P. Natl. Acad. Sci.*, 12291–12295.

Ide, S. T., Jessen, K., & Orr Jr, F. M. (2007). Storage of CO2 in saline aquifers: ffects of gravity, viscous, and capillary forces on amount and timing of trapping. *Int. J. Greenh. Gas Control*, 481- 491.

Juanes, R., Spiteri, E. J., Orr Jr., F. M., & Blunt,, M. J. (2006). Impact of of relative permeability hysteresis on geological CO2 storage. *Water Resources Research*, 1–13.

Kaarstad, O. (1992). Emission-free fossil energy from Norway. *Energy Conversion and Management*, 781–786.

Khosrokhavar, R., Elsinga, G., Farajzadeh, R., & Bruining, H. (2014). Visualization and ivestigation of natural convection flow of CO2 in aqueou sand oleic systems. *Journal of Petroleum Science and Engineering*, 230–239.

Kneafsey, T. J., & Pruess, K. (2010). Laboratory Flow Experiments for Visualizing Carbon Dioxide-Induced, Density-Driven Brine Convection. *Transport in Porous Media*, 123-139.

Kovscek, A. R., & Cakici, M. D. (2005). Geologic storage of carbon dioxide and enhanced oil recovery. II. Cooptimization of storage and recovery. *Energy Conversion and Management*, 1941–1956.

Kumar, A., Noh, M., Pope, G., Sepehrnoori, K., Bryant, S., & Lake, L. W. (2004). Reservoir Simulation of CO2 Storage in Deep Saline Aquifers. *SPE/DOE Symposium on Improved Oil Recovery.* Tulsa: Society of Petroleum Engineers.

Legg, J. F. (1998). Overview of carbon dioxide removal and disposal in Canada. *Energy Convers. Manage.*, 787–794.

Leonenko, Y., & Keith, D. W. (2008). Reservoir engineering to accelerate the dissolution of CO2 stored in aquifers. *Environ. Sci. Technol.*, 2742–2747.

Levine, J. S., Matter, J. M., Goldberg, D., Cook, A., & Lackner, K. S. (2007). Gravitational trapping of carbon dioxide in deep sea sediments: permeability,buoyancy, and geomechanical analysis. *Geophysical Research Letters* .

Lindeberg, E., & Wessel-Berg, D. (1997). Vertical convection in an aquifer column under a gas cap of CO2. *Energy Conservation and Management*, 229 -234.

Lund, J. W., Freeston, D. H., & Boyd, T. L. (2005). 2005 Direct application of geothermal energy: 2005 worldwide review. *Geothermics*, 691–727.

Marchetti, C. (1977). On geoengineering and the CO2 problem. *Climatic Change*, 59-68.

Metz, B., Davidson, O., Coninck, H., Loos, M., & Meyer, L. (2005). *Carbon Dioxide Capture and Storage: Special Report of the Intergovernmental Panel on Climate Change.* Cambridge: Cambridge University Press.

Mora, C., Frazier, A. G., Longman, R. J., Dacks, R. S., Walton, M. M., Tong,, E. J., . . . Giambelluca, T. W. (2013). The projected timing of climate departure from recent variability. *Nature*, 183–187.

Neufeld, J. A., Hesse, M. A., Riaz, A., Hallworth, M. A., Tchelepi, H. A., & Huppert, H. E. (2010). Convective dissolution of carbon dioxide in saline aquifers. *Geophysical Research Letters*.

Pau, G., Bell, J. B., Pruess, K., Almgren, A. S., Lijewski, M. J., & Zhang, K. (2010). High-resolution simulation and characterization of density-driven flow in CO2 storage in saline aquifers. *Advances in Water Resources*, 443–455.

Pruess, K. (2005). Numerical studies of fluid leakage from a geologic disposal reservoir for CO2 show self-limiting feedback between fluid flow and heat transfer. *Geophysical Research Letters*, 1–4.

Ranganathan, P., Farajzadeh, R., Bruining, H., & Zitha, P. L. (2012). Numerical Simulation of Natural Convection in Heterogeneous Porous media for CO2 Geological Storage. *Transp Porous Med*, 25–54.

Reed, A. C., Mathews, J. L., Bruno, M. S., & Olmstead, S. E. (2002). Safe disposal of one million barrels of NORM in Louisiana through slurry fracture injection. *SPE Drill. Completion*, 72–81.

Riaz, A., Hesse, M., Tchelepi, H. A., & Orr j r, F. M. (2006). Onset of convection in a gravitationally unstable diffusive boundary layer in porous media. *J. Fluid Mech.*, 87–111.

Rumynin, V. G., Konosavsky, P. K., & Hoehn, E. (2005). Experimental and modeling study of adsorption-desorption processes with application to a deep-well injection radioactive waste disposal site. *J. Contam. Hydrol.*, 19–46.

Saripalli, K. P., Sharma, M. M., & Bryant, S. L. (2000). Modeling injection well performance during deep-well injection of liquid wastes. *J. Hydrol.*, 41–55.

Slim, A. C., Bandi, M. M., Miller,, J. C., & Mahadevan, L. (2013). Dissolution-driven convection in a Hele–Shaw cell. *Phys. Fluids*.

Steven, S. H., Kuuskra, V. A., Gale, J., & Beecy, D. (2001). CO2 injection and sequestration in depleted oil and gas fields and deep coal seams: worldwide potential and costs. *Environmental Geosciences*, 200 - 209.

Tsai, P. A., Riesing, K., & Stone, H. A. (2013). Density-driven convection enhanced by an inclined boundary: Implications for geological CO2 storage. *PHYSICAL REVIEW E*.

Xu, T., Apps, J. A., & Pruess, K. (2003). Reactive geochemical transport simulation to study mineral trapping for CO2 disposal in deep arenaceous formations. *Journal of Geophysical Research*.

Yang, C., & Gu, Y. (2006). Accelerated mass transfer of CO2 in reservoir brine due to density-driven natural convection at high pressures and elevated temperatures. *Ind. Eng. Chem. Res*, 2430–2436.

Zhang, Y. Q., Oldenburg, C. M., & Benson, S. M. (2005). Vadose zone remediation of carbon dioxide leakage from geologic carbon dioxide sequestration sites. *Vadose Zone*, 858–866.

Zhou, Q. L., Bear, J., & Bensabat, J. (2003). Saltwater upconing and decay beneath a well pumping above an interface zone. *Transport Porous Med.*, 337–363.